Ferromagnetic quantum criticality in the uranium-based ternary compounds URhSi, URhAl, and UCoAl

Tristan Combier

UNIVERSITÉ DE GRENOBLE

THÈSE

Pour obtenir le grade de

DOCTEUR DE L'UNIVERSITÉ DE GRENOBLE

Spécialité : **Physique de la matière condensée et du rayonnement**

Arrêté ministériel : 7 août 2007

Présentée par

Tristan COMBIER

Thèse dirigée par **Jean Pascal BRISON**
et codirigée par **Dai AOKI et Georg KNEBEL**

préparée au sein **du Service de Physique Statistique, Magnétisme et Supraconductivité, INAC, CEA-Grenoble**
et de **l'École doctorale de Physique**

Criticalité quantique ferromagnétique dans les composés ternaires à base d'uranium: URhSi, URhAl, et UCoAl

Thèse soutenue publiquement le **27 février 2014**,
devant le jury composé de :

M. Klaus HASSELBACH
Directeur de Recherche, Institut Néel, CNRS, Grenoble, Président
M. Kenji ISHIDA
Professeur, Kyoto University, Kyoto 606-8502, Japon, Rapporteur
M. Manuel BRANDO
Docteur, Max Planck Institute, Dresden, Allemagne, Rapporteur
M. Dai AOKI
Professeur, SPSMS, INAC, CEA-Grenoble et IMR, Tohoku University, Oarai, Ibaraki, Japon, Co-Directeur de thèse

Ferromagnetic quantum criticality in the uranium-based ternary compounds URhSi, URhAl, and UCoAl

Contents

Acknowledgements

Au moment d'apposer la dernière touche à ce manuscrit, je tiens à remercier les personnes qui ont contribué à cette réalisation.

Dai Aoki who took me for an internship and then for the PhD thesis on his ERC grant. He introduced me to the job and guided me all through. He helped me a lot while letting me a large freedom, in all aspects. Working under his supervision was a great experience.

Georg Knebel qui m'a pris sous son aile, devenant ainsi mon co-encadrant en cours de route. On a travaillé ensemble sur UCoAl, et il m'a aidé sur bien des aspects. Pendant la rédaction de la thèse, qui a été une période décisive, j'ai pu compter sur sa disponibilité et son soutien, pour tous les problèmes auxquels je faisais face et toutes les questions que je me posais.

Jacques Flouquet qui a impulsé beaucoup d'énergie au labo, et s'est battu pour que je sois pris en thèse sur l'ERC. Son expertise scientifique a été d'une valeur inestimable du début à la fin.

Jean-Pascal Brison qui m'a pris sous sa responsabilité en tant que directeur de thèse officiel.

The members of the jury: Klaus Hasselbach for the role of examiner and president of the jury, Pr. Kenji Ishida and Manuel Brando for the role of reporters and for having come from so far. Their questions during the defense and the remarks on the manuscript were highly valuable inputs, and they made me feel that this PhD has been a success.

Le European Research Council pour le financement de cette thèse, et le CEA-Grenoble et l'Université Joseph Fourier pour m'avoir donné cette opportunité.

Au sein du SPSMS, toute l'équipe IMAPEC dont je faisais partie: Alexandre Pourret, Daniel Braithwaite, Jean-Michel Martinod, Marie-Jo Blanchard, Iulian Mattei, Bernard Salce, Michel Boujard, et l'équipe du D5: Karine Mony, Gérard Lapertot, Christophe Marin.

Les collègues de passage qui m'ont apporté leur expertise: Shin Kambe, Pr. Ōnuki, Pr. Harima, William Knafo, Tatsuma Matsuda, Hisashi Kotegawa, Pierre Haen, Rikio Settai.

À l'ESRF (ID12), Fabrice Wilhelm et Andrei Rogalev pour les manips de XMCD et tout le travail d'interprétation.

À l'ILL, Éric Ressouche pour les manips de diffraction sur URhAl.

À l'Institut Néel, Carley Paulsen et Martin Jackson, pour les mesures de phénomènes de relaxation dans UCoAl.

Merci à Xavier Jehl, Julien Bertheau (CEA-Leti) et Thierry Klein (Institut Néel) pour leur aide dans le développement (inabouti) d'une sonde de Hall pour mesures d'aimantation sous pression.

L'équipe LATEQS avec qui on a vécu dans les mêmes murs, partagé le café, l'hélium, le foot, le lab ski day, la bière du vendredi: je pense à Claude Chapelier, Xavier Jehl, Max Hofheinz, Pierre Payet-Burin, Frédéric Poletti, Louis Jansen, François Lefloch, Silvano Defranceschi, Jean-Pierre Cleuziou, Jean-Luc Thomassin.

Les thésards qui m'ont accompagné durant ces quatre années: Mathieu Taupin, Alexandra Palacio Morales, Mounir Boukahil, Benoit Voisin, Charlène Tonnoir, Alexander Grimm, Andreas Pfeffer, Driss Badiane, Caroline Richard, Toai Le Quang, Natalia Ares, Jean-Eudes Duvauchelle, Amalia Fernandez Panyela, Ludovic Howald, Elena Hassinger, Valentin Taufour qui m'a converti à la thèse et qui m'a passé le flambeau, et Gaël Bastien qui reprend le flambeau après moi.

Les post-docs avec qui on a partagé des bons moments: Eduardo Lee, Eduardo Hering, Scheilla Ramos, Liam Malone, Byron Villis.

Mon co-bureau Yusei Shimizu, témoin de ma dernière année, avec qui on a construit des ponts au-dessus du gouffre culturel qui sépare le soleil levant de l'Occident, en sifflant des bières à l'Ouest, notamment.

Les collègues dont j'ai eu souvent besoin pour mes manips: les "frères" Dubois (Gilles et Didier) du Service de Radioprotection, toujours dévoués pour venir faire un contrôle de mes échantillons, pleins de professionalisme et de bonne humeur. Au C5, Jean-François Jacquot, qui fait en sorte que tout se passe bien au squid, et qui m'a souvent aidé, avec Jean-Luc, grâce à leur esprit de Geo Trouvetout.

Igor, de Wavemetrics, un magnifique logiciel de graphing et de traitement de données.

Cette thèse est l'aboutissement de tout un parcours, de bien des années d'études. À ce titre je remercie tous les profs qui aiment leur travail et qui m'ont transmis la passion pour la physique. Je cite ceux qui m'ont le plus marqué ; à Grenoble: Frank Hekking, Thierry Klein, Frédéric Faure, Antoine Delon; Patrik Öhberg (Edinburgh), Jay Smith (Salford), Frédéric Chausse (Clermont-Ferrand), et mes profs de collège et lycée: M. Farilekas, Joël Bouchitté, M. Peotta, M. Mazoyer, M. Minet, M. Grand.

À mes amis passionnés, mes frères de pensée, mes compagnons de cordée, qui m'ont donné le courage et l'envie d'aller au fond des choses: Ahmed Trabelsi, Guillaume Géranton, Illya Plotnikov, Yvan Buggy. La physique est passionnante grâce à des gens comme vous.

À tous ceux qui sont venus assister à ma soutenance: collègues, famille et amis, en particulier les Rieu, Lily, Thierry, Jean, Javier, Ondrej, Claire, Véro, Alejandro.

À ma famille, pilier de mon existence sans qui je ne serais jamais arrivé là: mon père qui m'a transmis sa sensibilité à la beauté de l'Univers ; ma soeur qui m'a ouvert la voie,

et pour tout le souci que tu t'es fait pour moi ; Maman pour m'avoir coaché et aiguillé quand j'étais dans les limbes ; mon frère pour m'avoir toujours compris.

À Radiohead, pour les nuits blanches à bosser. Aux esprits de mon monde: l'Arbre, la Bistance du Triaxe.

À mes super potes de ces années de thèse: Toby et Illya. À Marta pour avoir porté tout le stress et pour ton soutien sans faille.

Résumé en français

Dans cette thèse, on étudie la criticalité quantique ferromagnétique dans trois composés ternaires à base d'uranium, par des mesures thermodynamiques et de transport sur des échantillons monocristallins, à basse température et sous haute pression. URhSi et URhAl sont des systèmes ferromagnétiques itinérants, tandis que UCoAl est un système paramagnétique étant proche d'une instabilité ferromagnétique. Tous ont une phase ordonnée de type Ising. Dans le composé orthorhombique URhSi, on montre que la température de Curie diminue lorsqu'un champ magnétique est appliqué perpendiculairement à l'axe facile d'aimantation, et une transition de phase quantique est attendue autour de 40 T. Dans le système hexagonal URhAl, on établit le diagramme de phase pression–température pour la première fois, lequel indique une transition de phase quantique vers 5 GPa. Dans le composé isostructural UCoAl, on étudie la transition métamagnétique par des mesures d'aimantation, d'effet Hall, de résistivité et de dichroïsme circulaire magnétique des rayons X. On observe des phénomènes de relaxation magnétique intrigants, avec des sortes de marches. L'effet Hall et la résistivité ont été mesurés à des températures de réfrigérateur à dilution, sous pression hydrostatique jusqu'à 2,2 GPa, et sous champ magnétique jusqu'à 16 T. La transition métamagnétique se termine sous pression et champ magnétique au niveau d'un point critique quantique terminal. Dans cette région, il se produit une forte augmentation de la masse effective, et une différence intrigante entre champ montant et descendant apparaît dans la résistivité transverse. Ce pourrait être la signature d'une nouvelle phase, éventuellement reliée aux phénomènes de relaxation observés dans les mesures d'aimantation, et résultant de frustrations au sein du réseau quasi-Kagomé que forment les atomes d'uranium dans cette structure cristalline.

Abstract

In this thesis we explore the ferromagnetic quantum criticality in three uranium-based ternary compounds, by means of thermodynamical and transport measurements on single crystal samples, at low temperature and high pressure. URhSi and URhAl are itinerant ferromagnets, while UCoAl is a paramagnet being close to a ferromagnetic instability. All of them have Ising-type magnetic ordering. In the orthorhombic compound URhSi, we show that the Curie temperature decreases upon applying a magnetic field perpendicular to the easy magnetization axis, and a quantum phase transition is expected around 40 T. In the hexagonal system URhAl, we establish the pressure–temperature phase diagram for the first time, indicating a quantum phase transition around 5 GPa. In the isostructural compound UCoAl, we investigate the metamagnetic transition with measurements of magnetization, Hall effect, resistivity and X-ray magnetic circular dichroism. Some intriguing magnetic relaxation phenomena are observed, with step-like features. Hall effect and resistivity have been measured at dilution temperatures, under hydrostatic pressure up to 2.2 GPa and magnetic field up to 16 T. The metamagnetic transition terminates under pressure and magnetic field at a quantum critical endpoint. In this region, a strong effective mass enhancement occurs, and an intriguing difference between up and down field sweeps appears in transverse resistivity. This may be the signature of a new phase, supposedly linked to the relaxation phenomena observed in magnetic measurements, arising from frustration on the quasi-Kagome lattice of uranium atoms in this crystal structure.

Foreword

This manuscript presents the studies that I have carried out during my PhD, over the period 2010-2013, at the SPSMS laboratory of Université Joseph Fourier – CEA Grenoble, under the joint supervision of Dai Aoki and Georg Knebel.

When I started my thesis, there was an intense research activity on the compounds UGe_2, URhGe, and UCoGe, following the recent discovery of the microscopic coexistence of ferromagnetism and superconductivity in these materials, in the vicinity of a quantum phase transition. In this context, my PhD subject was aimed to study some compounds which are closely related to these ferromagnetic superconductors, with the hope to find an ideal system to study the ferromagnetic quantum criticality. In our team, we started a research activity on UCoAl, which is the main chapter of my thesis. Besides, I studied two other compounds: URhSi and URhAl, which form two smaller chapters. I present the general context of heavy fermion physics and the properties of uranium-based ternary intermetallic compounds. A chapter details the experimental techniques. For each compound studied here, I present some results of resistivity, specific heat, magnetization or thermal expansion measurements. I focus on the new results, such as AC calorimetry under pressure on URhAl. In the main chapter on UCoAl, I present the results of a synchrotron experiment of X-ray magnetic circular dichroism, and pressure studies of Hall effect and resistivity.

Keywords: Uranium compounds, strongly correlated electrons, ferromagnetism, low temperature, heavy fermions, quantum criticality, new quantum phases, resistivity, Hall effect, magnetization, XMCD, high pressure.

Chapter 1

Introduction

Many uranium-based intermetallic compounds are strongly correlated electron systems, showing a variety of peculiar electronic and magnetic properties. They have been extensively studied with the discovery of heavy fermion systems and unconventional superconductivity. Among the most famous examples, we could cite UPt_3, UBe_{13}, URu_2Si_2... They recently attracted additional interest with the discovery of the ferromagnetic superconductors UGe_2, URhGe and UCoGe. Finally, they are a play ground to study quantum phase transitions, where non-Fermi liquid behaviour and possibly new quantum phases may appear.

1.1 The key properties of uranium compounds

Uranium has $5f$ valence electrons carrying a magnetic moment dominated by the orbital part due to large spin-orbit interaction. The $5f$ bands are close to the Fermi surface so they participate directly or are coupled to the conduction electrons.

In addition, the $5f$ electrons have strong mutual Coulomb repulsion. The strong correlations give rise to high band mass and thus to a peaked density of states. In addition, the $5f$ electrons hybridize with the conduction electrons, and this mixing leads to the formation of quasi-bound states. This is called the Anderson-Kondo mechanism. It is a many-body effect that further enhances the density of states, and in some cases gives rise to spectacular effective mass enhancement: the heavy fermion systems.

In the subsequent sections, we introduce the basics of heavy fermion systems, by describing the correlations between f electrons and conduction electrons. After showing that this phenomenon results from competing mechanisms, and therefore in the vicinity of a quantum phase transition, we get to the subject of ferromagnetic quantum phase transitions. In particular, we describe the topic of ferromagnetic superconductors.

Finally, we replace the compounds studied in this thesis (URhSi, URhAl, UCoAl) in the family of UTX compounds, to unveil some systematic properties.

1.2 Heavy Fermions

Heavy Fermion systems are strongly correlated electron systems. They are intermetallic compounds (i.e. alloys of different metals) generally U, Ce or Yb based, in which the interactions between f electrons and conduction electrons give rise to quasiparticles of highly renormalized effective mass of about $10-1000$ times the free electron mass (hence the term «heavy» Fermions). However, these properties only appear at low temperatures ($T \sim 10\,\mathrm{K}$). This manifests experimentally as a high electronic contribution to the heat capacity, and a high electron-electron inelastic scattering contribution to the electrical resistivity at low temperature. At high temperatures, these systems behave like «normal» magnetic metals. The large effective mass enhancement results from a hybridization between localized and conduction electrons through the Kondo effect.

The original picture that describes the Kondo effect is an interaction between an isolated magnetic impurity (an atom with partially field f orbital) in a see of conduction electrons, which appears as an antiferromagnetic exchange coupling. In heavy fermion systems, the Kondo effect occurs on a lattice of magnetic ions, so the *Kondo lattice* picture is realized.

In the single impurity Kondo effect, the magnetic impurity is completely screened by the scattering electrons with which it forms a non-magnetic singlet state in the ground state. This state is a «virtual bound state», in which the conduction electrons are almost localized by resonant scattering at the site of the impurity. A consequence of this is the formation of a narrow peak in the density of states close to the Fermi level. This Kondo resonance peak has a bandwidth of the order of $k_\mathrm{B}T_\mathrm{K}$. The famous signature of the Kondo effect is a minimum of resistivity at T_K, followed by a logarithmic increase with decreasing temperature.

In the Kondo lattice picture, there is an overlap of the neighbouring Kondo clouds, and below $T_\mathrm{coh} < T_\mathrm{K}$, the coherence length of the Kondo clouds extends to a large-scale many-body band of strongly interacting quasiparticles. These interactions produce non-perturbative corrections to the free electron picture, so that the quasiparticles behave like electrons with a highly renormalized mass. The low temperature behaviour of such a Kondo lattice system differ drastically from the single impurity Kondo model, and the resistivity decreases again with decreasing temperature. At low temperature, the resistivity has a AT^2 dependence, characteristic of electron-electron scattering in the Fermi liquid picture, where the coefficient A scales with the square of the effective mass: $A \sim m^{\star 2}$.

1.2.1 Competition with RKKY interaction: Doniach phase diagram

In metals, there is an indirect exchange interaction between local moments via the conduction electrons, called RKKY interaction (Ruderman-Kittel-Kasuya-Yosida). The

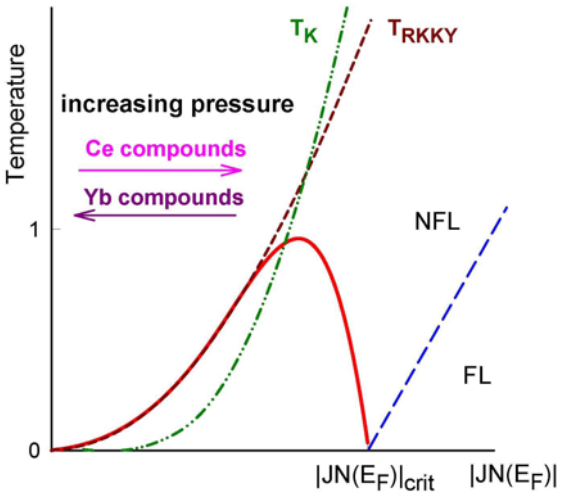

Figure 1.1: Doniach phase diagram of a Kondo lattice system. There is an opposite pressure response for Ce and Yb because of the opposite sign of the charge carriers. Credits: E. Bauer (TU Wien, Austria).

RKKY interaction is oscillatory with the distance, so the coupling can favor parallel or antiparallel spin alignment.

The RKKY interaction yields a magnetically ordered ground state, while the Kondo effect leads to a paramagnetic state. Both interactions are competing. Doniach [1] established that the energy scales for Kondo and RKKY have different dependence on the degree of hybridization. Figure 1.1 shows the famous Doniach diagram: T_K,T_{RKKY} vs the product $JN(E_f)$, where J is the coupling between f and conduction electrons, $N(E_f)$ is the DOS at the Fermi level. The ground state is magnetic when RKKY dominates, and non-magnetic when Kondo dominates. This diagram illustrates the possibility to tune the system between magnetic and non-magnetic state by varying the hybridization via pressure or doping. At zero temperature, for a critical value of $JN(E_f)$, a quantum phase transition occurs. In the frontier region, quantum critical fluctuations lead to non-Fermi liquid behaviour (NFL), and a superconducting phase sometimes appears.

This picture basically applies to localized magnetic systems such as rare earths compounds, but the validity is questionable in the case of uranium compounds, which are more itinerant. Nevertheless, it qualitatively explains the typical phase diagram of these materials.

1.3 Quantum phase transitions

The physics of quantum phase transitions was successfully studied in antiferromagnetic (AF) systems, where there is a continuous change of the order parameter at zero temperature, through a quantum critical point (QCP). In contrast, when it comes to itinerant ferromagnetic (FM) systems, the QCP seems generally pre-empted by the occurrence of a first-order transition.

1.3.1 Antiferromagnetic quantum critical point

There are two different scenarios for the state of the system in the vicinity of a QCP (see the review of Löhneysen *et al.* [2]):

- in a «conventional» QCP, the system is described in terms of quasiparticles interacting with spin fluctuations, resulting in effective mass enhancement. The Kondo temperature increases continuously and there is no change of the Fermi surface. Such AF QCPs are found in itinerant systems (= spin density wave) e.g. $CeCu_2Si_2$, $CeRu_2Si_2$...

- in the «unconventional» QCP, the Kondo temperature goes to zero, and there is a change of the Fermi surface, which becomes larger on going from the magnetic to non-magnetic ground state due to the inclusion of the $4f$ states into the Fermi sea. This scenario is referred to as *local criticality*, or *Kondo breakdown*. The candidates are $YbRh_2Si_2$ [3, 4] and $CeCu_6$ [5, 6].

1.3.2 Ferromagnetic systems: hidden QCP

In the usual case of a ferromagnetic system, the transition from paramagnetic to ferromagnetic state at the Curie temperature T_C is of second-order type. In the temperature-pressure phase diagram of several weak ferromagnets, the transition temperature decreases with pressure and reaches 0 K at some critical pressure P_c. At some pressure below P_c, the transition becomes of first-order type, and the ordered moments disappear discontinuously. The limit between the two regimes is a *tricritical point* (TCP). Such type of behaviour was observed in MnSi [7], UGe_2 [8], $ZrZn_2$ [9], and in the doped systems $Co(Si_{1-x}Se_x)_2$ [10] and $(Sr_{1-x}Ca_x)RuO_3$ [11] where the Se- or Ca- doping plays the role of tuning parameter. The existence of a tricritical point seems to be a general rule, since it has also been observed in simple ferromagnets like Fe,Co,Ni [12].

As a rule, a TCP occurs in the T-P phase diagram of a ferromagnet at low temperature, close to P_c, where $\mathrm{d}T_C/\mathrm{d}P$ diverges, or at least becomes very large, in difference to a second-order phase transition. It has been demonstrated theoretically by taking into account magneto-elastic coupling effects, that the transition becomes first-order when

the slope $-\mathrm{d}T_C/\mathrm{d}P$ is larger than a critical value which involves the compressibility and specific heat jump at T_C. [13].

This starting point is widely admitted among the community, but it seems not sufficient to explain the rather extended range of pressure-temperature in which first-order occurs (several orders of magnitude too low). The magneto-elastic coupling could be sufficient to explain the tricriticality in UGe_2, provided that we take into consideration the dimensionality and the anisotropy of the system [14].

Another way to explain the first-order transition is the existence of non-analytic terms in the Landau free energy. Such non-analytic terms generically arise in the presence of gapless excitations (soft modes) that couple to the fluctuations of the order parameter. In the case of metallic FM-PM transition, Belitz *et al.* [15] proposed that the soft modes in question are spin-triplet particle-hole excitations, which couple to the spin fluctuations. At the transition, the fluctuations become long-range, the interactions with the soft modes «dress» them with a mass. The massive modes have an energy cost, and thereby stabilize the system in either side of the transition, giving it the first-order character. This concept of mass-generation is very general. It is applicable to all metallic FM-PM transitions in dimension $d > 1$, even if the electron responsible for magnetism are not the conduction electrons. In this sense, this theory is above the debate of itinerant/localized FM picture.

1.3.3 Metamagnetic wing

Regardless of the physical mechanism producing the first order transition, a direct consequence of the first-order nature of a PM-FM transition is the *metamagnetism* above P_c, which can be understood by simple Landau free energy considerations. This is illustrated in Fig. 1.2, with the free energy F as a function of the order parameter M in different situations of temperature T and conjugate of the order parameter H (magnetic field applied parallel to M). The dots indicate the stable state: paramagnetic (PM) or ferromagnetic (FM).

In a second-order transition, there is only one minimum in the $F(M)$ expansion (Fig. 1.2-a). At the critical temperature T_C, the curvature at $M = 0$ changes sign, and the stable M continuously changes from zero to finite values. In the PM phase close to a second-order transition, H does *not* induce any transition (Fig. 1.2-b).

On the contrary, in the first-order case, there are two local minima in $F(M)$: one at zero M and one at finite M (Fig. 1.2-c). At T_C, there are two stable states separated by an energy barrier, and in the PM phase close to a first order transition, H *does* induce a transition (Fig. 1.2-d).

So far we only considered the two-dimensional temperature-pressure phase diagram. If we add an extra thermodynamical variable, the magnetic field H, we obtain the schematic phase diagram shown in Fig. 1.3. The tricritical point is actually the starting point of a line that extends above P_c in the T-P-H phase diagram. This is a line of *criti-*

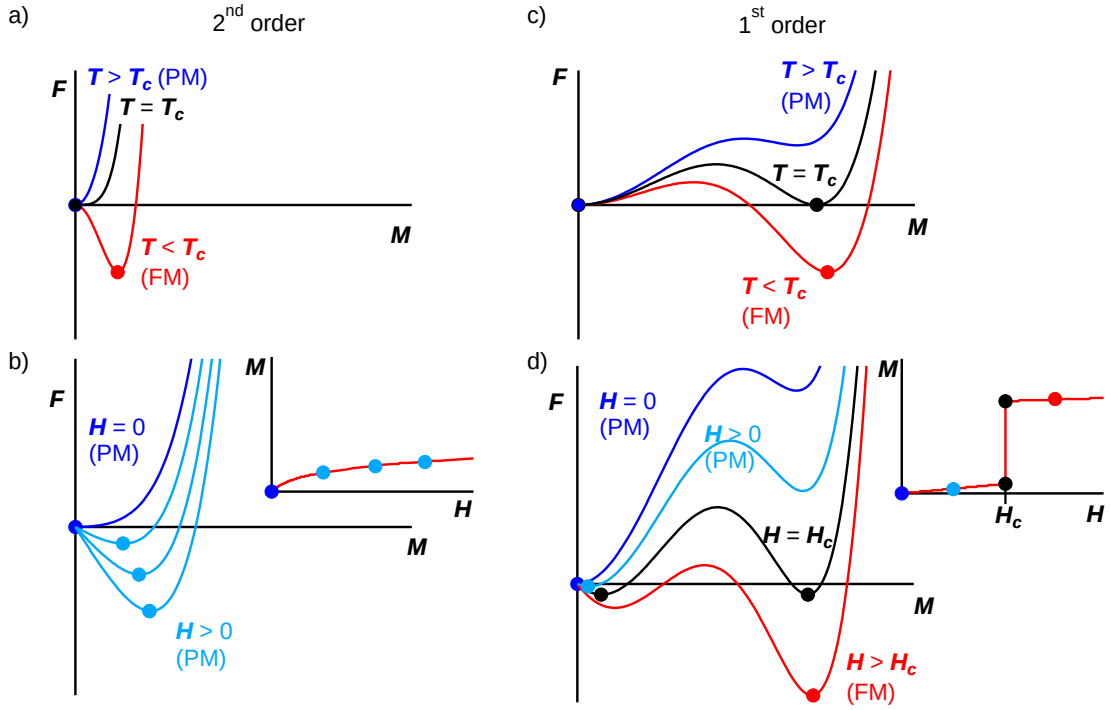

Figure 1.2: (taken from [19]) Free energy F as a function of the order parameter M (magnetization), in a FM system with second-order transition (a,b) and first-order transition (c,d). The panels illustrate the role of temperature at zero field (a,c), and the role of field $H \parallel M$ close to the FM transition (b,d). Dots indicate the stable states. Insets show the field dependence of M associated with panels b & d.

cal endpoints (CEP) below which a first-order metamagnetic transition is observed from the PM state to a field-induced FM state. As pressure is increased, the metamagnetic field H_m increases, and T_{CEP} decreases. This first-order transition plane in the T-P-H phase diagram was named «wing» [16]. The line of CEPs eventually reaches 0 K at a so-called *quantum critical endpoint* (QCEP), which is a new class of quantum criticality. The wing has been observed experimentally only in UGe_2 [17, 18], and in UCoAl where it occurs at ambient pressure. This is the main topic of Chapter 5.

1.4 UTX compounds

UTX compounds refer to the class of ternary intermetallic compounds of Uranium with T = late transition metal (3*d*: Fe,Co,Ni – 4*d*: Ru,Rh,Pd – 5*d*: Ir,Pt) and X = *p*-element (3*p*: Al,Si – 4*p*: Ga,Ge – 5*p*: In,Sn). It is a class of materials which have attracted much attention because the semi-delocalized $5f$ electrons of the U atoms give rise to a great

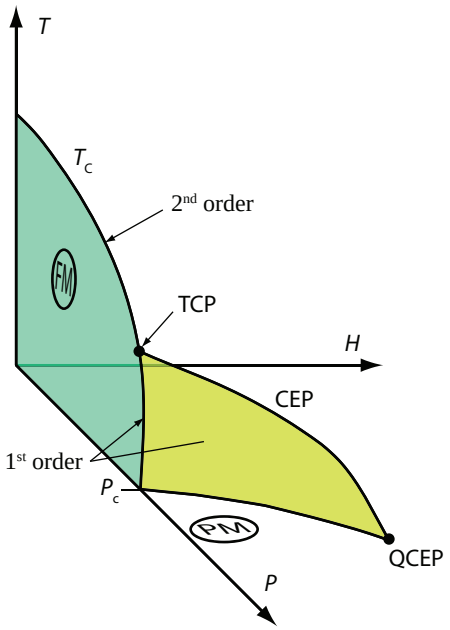

Figure 1.3: Schematic Temperature(T)–Pressure(P)–Field(H) phase diagram of an itinerant ferromagnet (FM), where the Curie temperature T_C is suppressed by pressure. The ground state is paramagnetic (PM) above the critical pressure P_c. The transition becomes first-order at the tricritical point (TCP). Above the critical pressure P_c, there is a metamagnetic «wing» at temperatures below the line of critical endpoints (CEP), which terminates at a quantum critical endpoint (QCEP).

diversity of magnetic properties.

Many of them have a magnetic ground state (ferro- or antiferromagnetic) with a reduced U moment compared to the free ion value, huge uniaxial anisotropy, and a moderately enhanced electronic specific heat compared to the bare band mass.

The majority of these compounds crystallize in either of the two crystallographic structures: the orthorhombic TiNiSi (Fig. 1.5) (or the closely-related $CeCu_2$)-type and the hexagonal ZrNiAl-type (Fig. 1.4). In this thesis, we study compounds of the two families: the orthorhombic URhSi, and the hexagonal URhAl and UCoAl.

The main mechanisms affecting the magnetic properties of these compounds are the overlap of neighbouring U $5f$ orbitals and the hybridization of U $5f$ orbitals with the orbitals of the other T and X atoms, generically referred to as $5f$-ligand hybridization. Both mechanisms lead to the delocalization of U magnetic moments, and the U moments will be coupled via direct $5f$ - $5f$ and via indirect exchange interaction involving other non-f electrons.

Hill [20] conjectured that for inter-U distance $d_{\text{U-U}} < 3.4\text{-}3.6\,\text{Å}$ (the so-called *Hill limit*), direct overlap of the U $5f$ orbitals leads to the delocalization of $5f$ electrons and ultimately yields to the washout of magnetic order. Above the Hill limit, the picture of localized magnetic moments ordering ferro- or antiferromagnetically is normally expected.

In the Hill limit region, the $5f$-ligand hybridization — which also tends to delocalize the $5f$ electrons — is the key that controls the magnetic properties. Indeed, the magnetic ordering seems intimately related to the degree of $5f$ - d hybridization via the degree of d-shell filling of the transition metal. Table 1.1 lists all the UTAl compounds with *ZrNiAl*-type structure, sorted by increasing d-orbital filling. On top of the list are the magnetically ordered systems (FM or AF), then when decreasing the d-orbital occupancy we find PM systems with strong FM correlations (UCoAl, URuAl), and finally the non-magnetic compound UFeAl. This tendency is also observed in the UTX compounds crystallizing in the TiNiSi-type structure (see Chapter 3).

Quite logically, the UTX materials (regardless of their crystal structure) with strongest electronic correlations (highest γ-value) are found in the borderline region of both hybridization mechanisms, where $d_{\text{U-U}}$ is close to 3.5 Å) and with intermediate d-filling of the T element : (URhGe, UNiAl, UCoAl, URhAl).

1.4.1 Hexagonal ZrNiAl-type

In the sub-group of UTX with *ZrNiAl*-type structure (space group $P\bar{6}2m$) (Fig. 1.4), the coupling is generally ferromagnetic within the hexagonal planes (only exception : UNiAl $\vec{q} = (0.1, 0.1, 0.5)$), and is either ferro- or antiferromagnetic (UNiAl, UNiGa,...) between the planes [23]. This fact does not necessarily yield a magnetically ordered ground state, but the FM correlations do play a role in URuAl (paramagnet with strong

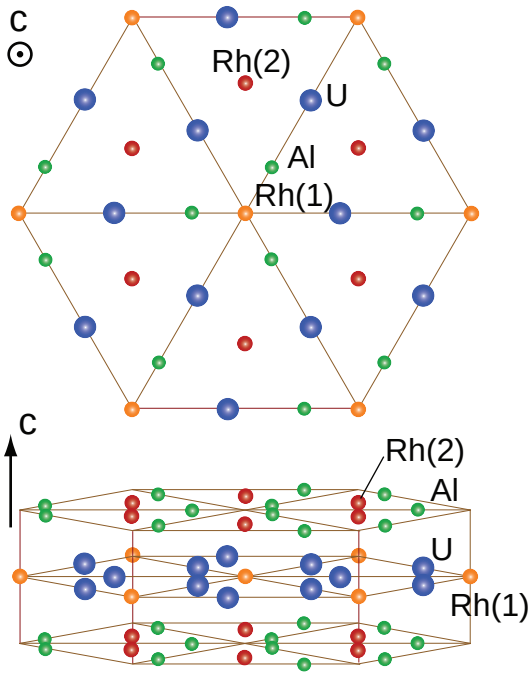

Figure 1.4: Crystal structure of URhAl (*ZrNiAl*-type, space group $p\bar{6}2m$), with two non-equivalent Rh positions, consisting of alternating hexagonal layers of U–Rh(1) and Al–Rh(2). Lattice parameters are $a = 696.5\,\mathrm{pm}$ and $c = 401.9\,\mathrm{pm}$ for in-plane and inter-plane distances, respectively (from [21]). Credits: Nohara *et al.* [22]

spin fluctuations) and UCoAl (paramagnet with metamagnetic transition to a FM state, see chapter 5).

For X = Al, the compounds with transition metal T = Fe, Co, Ni, Ru, Rh, Ir and Pt crystallize in the *ZrNiAl*-type structure. They have all been studied by Prague and Amsterdam groups (see [23] for an exhaustive review).

In the hexagonal ZrNiAl-type structure, the crystal electric field confines the electrons of large l orbitals in the basal plane, so that the hybridization mechanisms will be strongly anisotropic. As a consequence, since the strong spin-orbit coupling of the $5f$ states produces orbital magnetism, the moments will be locked in the c-direction, leading to Ising-like systems. It should be noted that this crystal structure (space group $p\bar{6}2m$) does not have inversion symmetry, thus a large Fermi surface splitting is generally expected [24]. Furthermore, the crystal structure forms the quasi-Kagome lattice, leading to a geometrical frustration.

Table 1.1: UTAl compounds with *ZrNiAl*-type structure (adapted from [23])

d-filling	compound	lattice parameters a (Å)	c (Å)	γ (mJ mol^{-1}.K^{-2})	$T_{N,C}$ (K)	ground state
$6s^15d^9$	UPtAl	7.012	4.127	69	46	FM
$4s^23d^8$	UNiAl	6.733	4.035	164	19.3	AF along c, quasi-FM planes (low-q in-plane modulation)
$5s^14d^8$	URhAl	6.965	4.019	67	27	FM
$6s^25d^7$	UIrAl	6.968	4.030	50	64	FM
$4s^23d^7$	UCoAl	6.686	3.966	65		PM with high χ, FM after metamagnetic transition
$5s^14d^7$	URuAl	6.895	4.029	45		PM with spin fluctuations
$4s^23d^6$	UFeAl	6.672	3.981	21		PM, 0.11 μ_B at 35 T, isotropic, no FM interaction

1.4.2 TiNiSi-type structure

URhSi belongs to the family of UTX compounds (T = late transition metal, X= Si or Ge) crystallizing in the orthorhombic TiNiSi-type structure (space group $Pnma$). In this structure, the U atoms are arranged in zig-zag chains along the a-axis (Fig. 1.5). There are 14 compounds in this family, showing a variety of magnetic ground states (see Fig. 1.6), which are believed to be controlled by the degree of $5f$-ligand hybridization which reduces with increasing filling of d orbitals of the T elements. Magnetic order is found in the compounds with higher d.

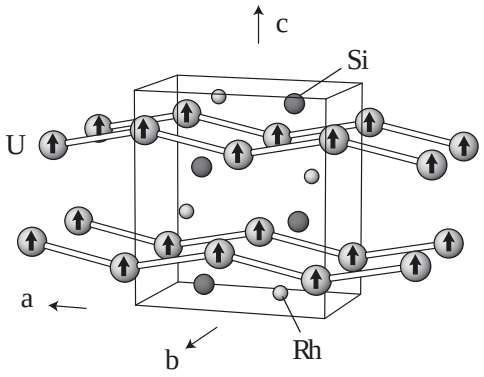

Figure 1.5: (taken from [29]) Crystal structure of URhSi (*TiNiSi*-type). The arrows on the U sites denote the direction of the magnetic moments.

Among this class of materials (shown in Fig. 1.6), the compounds URhSi, URhGe, and UCoGe are borderline cases between paramagnetic and magnetically ordered compounds, with intermediate degrees of hybridization. A consequence of this is the rather enhanced electronic correlations at low temperatures ($\gamma \sim 100 - 150\,\mathrm{mJ.mol^{-1}.K^{-2}}$), dual localized-itinerant magnetic properties, and strongly fluctuating spins.

URhGe and UCoGe attracted much attention because of the coexistence of ferromagnetism (FM) and superconductivity (SC) [25, 26]. These compounds have peculiar magnetic anisotropy profiles, c being the easy axis, a the hard axis, and b is intermediate (high susceptibility without spontaneous component). Upon application of a magnetic field along the b-axis, T_C decreases and eventually reaches 0 K at $H_{\|b} \approx 10-15\,\mathrm{T}$. There, a field-induced SC phase was discovered in URhGe [27], and an enhancement of T_{SC} in UCoGe [28]. (See the magnetization and phase diagram of URhGe, Fig. 1.7)

1.5 Ferromagnetic superconductors

In the case of s-wave pairing, magnetism and superconductivity (SC) are conflicting each other, since the spin-flip process is pair-breaking. Coexistence of antiferromagnetism (AF) and s-wave SC can be realized when the coherence length ξ_0 is much larger than the AF periodicity, so that the average value of magnetization is zero, but this situation is exceptional.

In strongly correlated electrons systems, the strong Coulomb repulsion undermines the s-wave pairing. In heavy fermion systems, high T_c cuprates and Fe-pnictides, the superconductivity is *unconventional*: the symmetry of the SC gap is either p-wave or d-wave, and the total angular momentum is not zero.

There are many examples of antiferromagnetism coexisting with superconductivity, but only 3 examples of ferromagnetic superconductors (with microscopic coexistence of

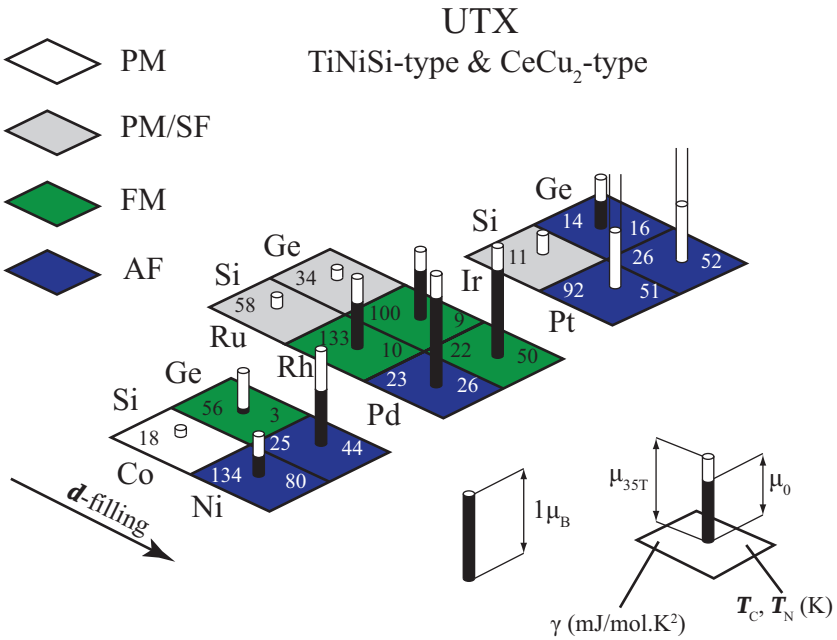

V. Sechovský & L. Havela, ***Handbook of Magnetic Materials***, vol. 11 (1998)

Figure 1.6: (taken and adapted from [23]) Schematic plot illustrating evolution of some electronic properties (type of magnetic ground state, magnetic ordering temperature, γ-value (linear coefficient of the specific heat), spontaneous magnetic moment (black part of a column), induced magnetic moment in field of 35 T (white top parts of a column) of UTSi and UTGe compounds with the orthorhombic TiNiSi-type structure or the closely-related $CeCu_2$-type structure. PM/SF stands for paramagnetic with spin fluctuations.

FM and SC): UGe_2 [30], URhGe [25], and UCoGe [26].

In UGe_2, SC occurs under pressure, in the vicinity of the transition between two FM states (FM_2/FM_1).

In UCoGe, it occurs a ambient pressure, but the maximum of T_{SC} corresponds to the pressure where the Curie temperature T_C reaches 0 K. That is, SC is observed both in FM and PM state.

In URhGe, T_{SC} decreases and T_{Curie} increases with pressure, indicating that pressure drives the system away from a quantum critical region. When the field is applied along the hard magnetization axis ($H \parallel b$) the FM fluctuations are strongly enhanced by suppressing T_{Curie} under magnetic field. Consequently, SC reappears with spin triplet state, where there is no Pauli paramagnetic effect.

This mechanism was understood as follows. In the orthorhombic crystal structure of URhGe, the U magnetic moments order ferromagnetically along the c–direction — which is the easy magnetization axis — below $T_C = 9.5$ K. The magnetic order is Ising–type, but with a rather pronounced susceptibility along the b–axis. When field is applied along the b–axis, at some point ($H = 12$ T) the magnetization reorients from the c– to the b–direction. The triplet pairing mechanism is attributed to the critical magnetic fluctuations associated to this spin-reorientation process [27].

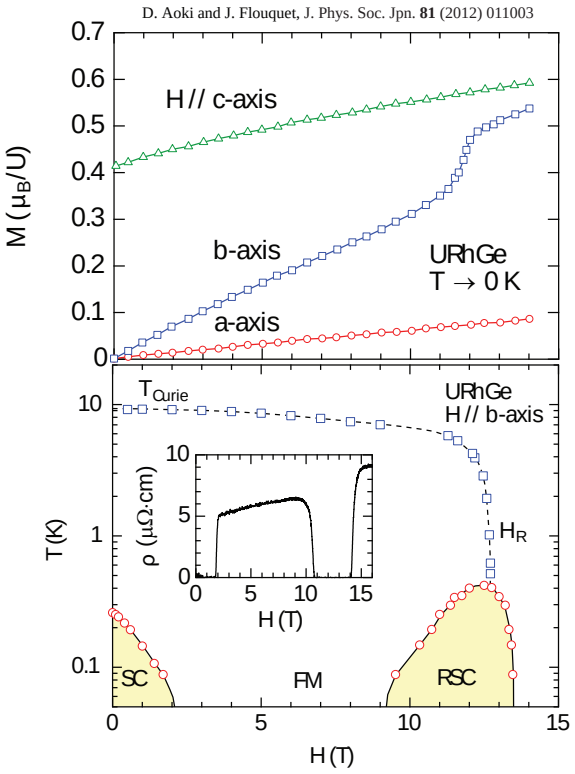

Figure 1.7: (taken from [29]) Magnetization curves and temperature-field phase diagram for $H \parallel b$-axis in URhGe. SC, RSC and FM denote superconductivity, re-entrant superconductivity and ferromagnetism, respectively. The inset shows the field dependence of resistivity at low temperatures ($\approx 80\,\mathrm{mK}$). It is noted that the field range of RSC is very sensitive against a small mis-orientation to the c-axis.

Chapter 2

Experimental techniques

2.1 Sample preparation

The compounds studied in this thesis (URhSi, URhAl, UCoAl) have been grown at our laboratory's crystal growth facility.

2.1.1 Crystal growth

The starting materials were prepared as follows:

- Uranium: (depleted — 0.2% of ^{235}U) purity: 99.9% (3N). Solid bars with oxidized surface. The desired amount is cut with electro-erosion. The oxide is removed by electro-etching, in a bath of 95% acetic acid and 5% perchloric acid, with 12 V_{DC} applied between U (anode, positive end) and a stainless steel plate (cathode, negative end).

- Rhodium: 99.99% (4N). Powder form. Very expensive ($\sim$ \$100 per gramm). It has to be melt in RF furnace first to obtain a pellet, otherwise the arc discharge would blow the powder. This process is performed under high vacuum (10^{-6} Torr) which allows the material to degas.

- Cobalt: (3N) $\sim$ 0.1 g chunks. Etching at 85 °C (30% nitric acid, 10% sulfuric acid, 10% phosphoric acid and 50% acetic acid) and rincing with 50% nitric acid and 50% water.

- Silicon: (6N) industry-grade quality wafers.

- Aluminium: (5N) high-purity chunks. Aceton cleaning.

The total mass of material for a crystal growth is typically $\sim$ 6 g.

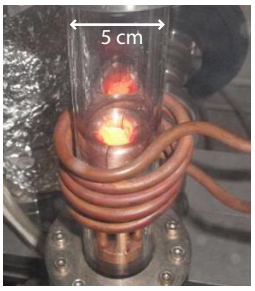

Figure 2.1: Picture of the radio-frequency furnace. We can see the coil and, inside the quartz tube, the material melting in the crucible.

The starting materials were prepared in stoichiometric proportions (all compounds studied here are congruent). We used two different furnaces to melt the materials: a radio-frequency furnace (under high vacuum), and a tetra-arc furnace (under Ar gas atmosphere).

In the case of RF furnace (Fig. 2.1), the material is contained in a copper crucible, and it is heated by induction from an external coil. The coil and the crucible are water-cooled. The crucible consists of an assembly of winglets which are separated by a gap. This construction is designed to avoid Eddy currents and thus minimize the heating of the crucible. High vacuum is obtained with an ion pump. The melt pellet is self-sustaining and hence it is quite unstable. This is why the RF furnace was used only to melt the starting material and let it degas. The single crystal was pulled using the tetra-arc furnace.

In the tetra-arc furnace, four torches (tungstene, 2% La doped) are positioned at $\sim 5\,\mathrm{mm}$ from the pellet (see Fig. 2.2). Electrical arcs ionize the gas between the torches and the pellet, which has electrical continuity to the crucible. The crucible is made of copper, and it is water-cooled. The crucible can rotate for homogeneous heating.

The single crystal is obtained by immersing a cold tip (tungstene) into the melt, and then slowly pulling upwards. The material crystallizes on the tip, and forms a long-shape ingot. Typical pulling rate of 15 mm/h is kept constant, while the position of the torches and the arc intensity control the thickness of the ingot. Approximately 1 cm below the tip, the thickness of the ingot is locally reduced to $\lesssim 1\,\mathrm{mm}$, and expanded again. This way, if there were several crystal grains forming at the beginning, this «necking» process singles out one orientation, thus favouring a single-crystal ingot building up afterwards. The ingot can be very fragile at the necking, and it sometimes break (as shown in Fig. 2.2).

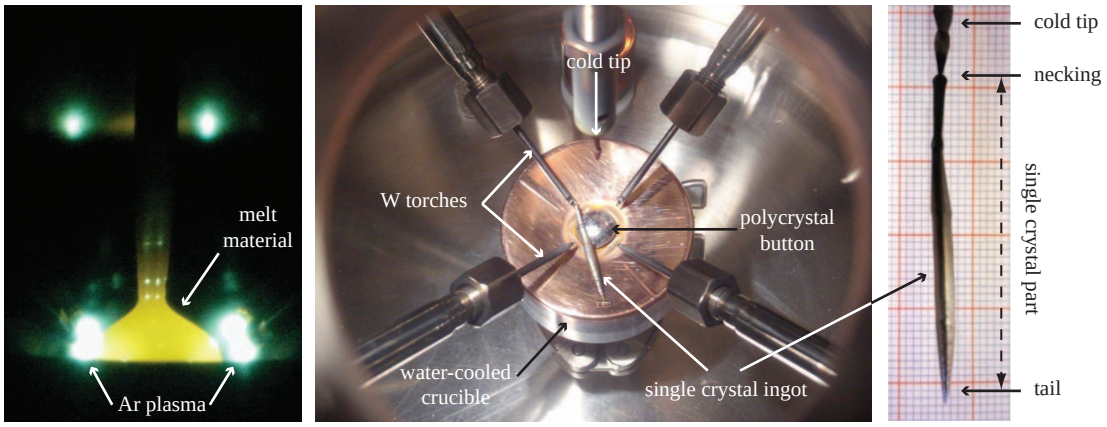

Figure 2.2: Crystal growth in a tetra-arc furnace by the Czochralski technique

2.1.2 Crystal orientation

The single crystal and orientation is checked with X-ray Laue photograph (Fig. 2.3). A sample is positioned in the X-ray beam (polychromatic), and the diffraction pattern is recorded in a back-scattering geometry. Historically, the diffraction pattern was recorded on argentic film, which necessitated long exposure time ($\sim$ 30 min) and developpement process in a dark room. The film was recently [1] replaced by a CCD camera, thus reducing the exposure time to $\sim$ 30 s.

A clean diffraction pattern is the fingerprint of a single-crystal phase. We use the software *OrientExpress* to index the diffraction peaks and find the orientation of the crystal. In Figure 2.3 we show a Laue photograph of a single crystal of UCoAl. We recognize the hexagonal pattern. The spot close to the center is the c direction. [2] The software then provides the possible combinations of rotations ϕ_x, ϕ_y, ϕ_z to orientate the crystal in a particular direction.

The sample is set on a goniometer and cut with an electro-erosion machine, which is a wire saw with a current flowing between the wire and the sample. It is performed in a petrol bath, to avoid spreading radioactive dust.

2.1.3 Safety considerations related to Uranium

In our crystal growth facility, the activity on uranium is controlled. Special rooms are dedicated to the handling of Uranium materials. These areas are supervised by the CEA radioprotection team. Access is restricted. As a staff working with uranium material,

[1] we used a film until 2011!

[2] The notation with 4 indices $(hkjl)$ with $h + k + j = 0$ is used for hexagonal structures, in order to lift the ambiguity between direct and reciprocal space: $0001 = c$, $10\bar{1}0 = a$ (direct space), $1\bar{1}00 = a^\star$ (reciprocal space).

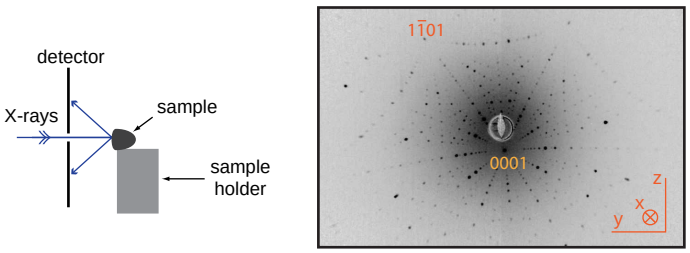

Figure 2.3: X-ray Laue schematic and photograph. Here in the case of UCoAl.

we have to attend special safety training, and we receive regular medical attention.

Natural uranium contains 3 isotopes : ^{238}U (99.275%), ^{235}U (0.72%) and ^{234}U (0.0054%), which are all radioactive. They are alpha-emitters, and they produce a series of short-lived alpha and beta-emitters, in addition to the gamma emission accompanying every decay.

The uranium used for our research is depleted uranium (0.2% of ^{235}U), which is a by-product of ^{235}U enrichment processes for the nuclear industry. The total activity of depleted U (15 kBq/g) is reduced compared to the natural composition (25 kBq/g), mainly owing to the reduction of the ^{234}U abundance, which is responsible for half of the activity in the natural U [31].

Because of its short penetration length, the alpha emission is potentially hazardous on ingestion or inhalation, while the beta and gamma emissions are potentially hazardous on external exposure.

Given the small quantities of material that we use, the external exposure is not a concern. At a distance of a few cm from the source, the activity of a few grams of U vanishes in the ambient radioactivity level.

On the contrary, internal exposure (by ingestion or inhalation) is a matter of serious concerns. For this reason, special care is taken to avoid producing dust: cutting and polishing are performed in a petrol bath, methodical cleaning of the furnace and tools is performed at every step of the processes.

The samples going out from the facility (to perform experiments in another building or outside the CEA) require an official declaration, and are subject to the radioactive material transport regulations.

2.2 Hydrostatic pressure techniques

2.2.1 Piston-cylinder cell

The piston-cylinder cells are used for hydrostatic pressures up to $\sim$ 3 GPa (1 GPa = 10 kbar). The advantage of this type of cells is the rather large sample space. The model shown in Fig. 2.4 has been used for resistivity, Hall effect, magnetization with Hall

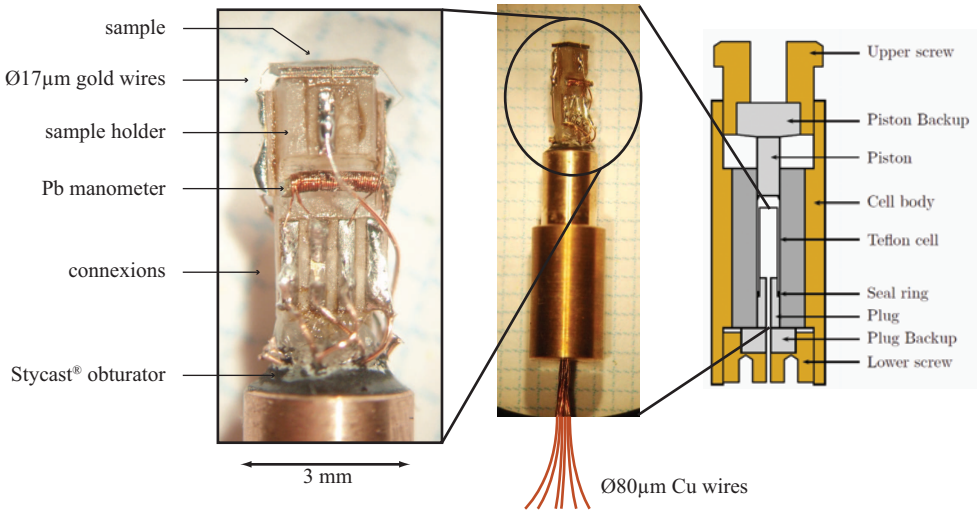

Figure 2.4: Details of a piston-cylinder pressure cell, with pictures of a setup (here, for Hall effect measurements).

sensor, and strain gauge magnetostriction measurements. It can reach ~ 3 GPa. The cylinder is made of CuBe and NiCrAl alloys (hybrid cell). The piston, piston-backup and plug-backup are made of WC (tungstene carbide). The plug (CuBe) has a thin shaft for the wires, which is sealed with Stycast. The sample holder is mounted on the plug. The setup is encapsulated in a teflon tube (not shown here) containing the pressure transmitting medium (Daphne oil 7373). Copper seal rings ensure etancheity on both side of the teflon capsule. Pressure is applied by pushing on the piston backup with a hydraulic press, and it is then clamped by the upper screw.

Pressure is determined by the superconducting transition temperature of lead. Two Cu wires (ø25 µm, ~ 20 turns) are wound around a piece of lead (ø200 µm). The superconducting transition temperature is determined by AC susceptibility measurement.

The dimensions of the setup shown in the pictures (Fig. 2.4) are ø3 mm and 6 mm high. The preparation requires some dexterity and self control!

A setup like this can only be used once, since once it has been used at high pressure, the plug is deformed and cannot be used again.

2.2.2 Pressure cell for magnetic measurements

A special pressure cell was used for magnetic measurements. It is made of a Cu-Ti alloy, which has a low magnetic response compared to other strong alloys such as NiCrAl or CuBe. This cell has been developped by Yusei Shimizu in 2009 at Hokkaido University. It is based on the models developped by Kobayashi *et al.* [32] and Tateiwa *et al.* [33].

This is a cell of very small dimensions (ø8.8 mm) which is designed to fit in a com-

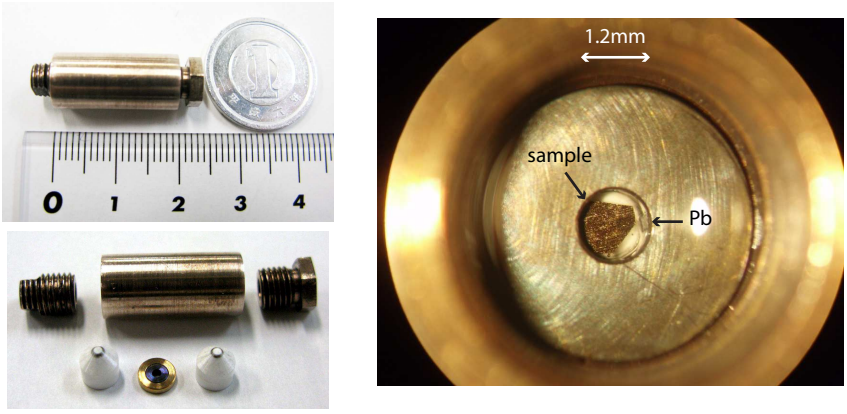

Figure 2.5: Pictures of the indenter-type pressure cell for magnetic measurements.

mercial SQUID magnetometer (MPMS, *Quantum Design*).

It consists of a Cu-Ti tube and locking nuts, two zirconia anvils, and a hybrid CuBe-NiCrAl gasket (see Figs. 2.5 and 2.6). This construction is called *Indenter-type*: the plateau of the anvils is smaller than the diameter of the hole in the gasket.

We used Daphne oil 7373 as a pressure transmitting medium.

Pressure was determined from the superconducting transition of Pb. The background — mainly due to the NiCrAl gasket — is punctual, and thus yields a simple dipolar signal which adds up to that of the sample. The magnetization of the sample is then obtained by simply substracting the magnetization of the cell, which is measured independently. The signal of the sample is of the same order of magnitude as the background. Figure 2.7 shows the magnetization of the empty cell (background), and with a sample of UCoAl inside. We can see the signal of the metamagnetic transition at 0.7 T (here, $P = 0$).

The pressure is determined by the detecting the superconducting transition of a piece of lead. The signal of the Pb is negligible compared to that of the sample, but just enough to detect an anomaly at T_{SC}. To detect the transition, it is necessary to apply field, while at the same time this decreases T_{SC}. Figure 2.8 shows the magnetization versus temperature at around 4 K, at various applied field close to 0. There is a clear anomaly associated with the SC transition of Pb. The anomaly grows with field (diamagnetic response of a superconductor), while T_{SC} decreases. The maximum of T_{SC} is inferred to be 7.18 K, which corresponds to zero pressure. The maximum occur at a finite value of applied field, which compensates the remanent field.

2.2.3 Diamond anvil cell

We use diamond anvil cells for high pressure studies (typically up to ~ 10 GPa).

The main difficulty is the small sample space. This type of pressure cell has been used during this thesis for AC calorimetry measurements.

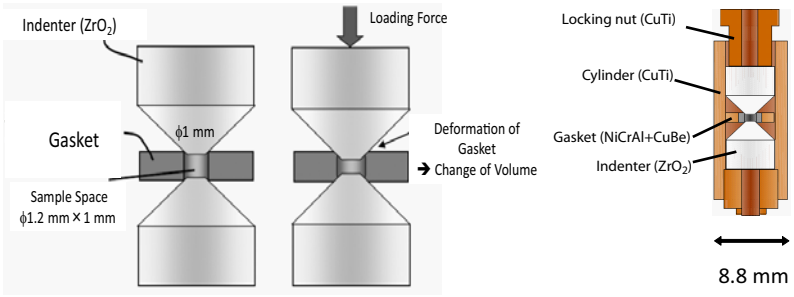

Figure 2.6: Sketch of the indenter-type cell for magnetic measurements. Credits: Y. Shimizu

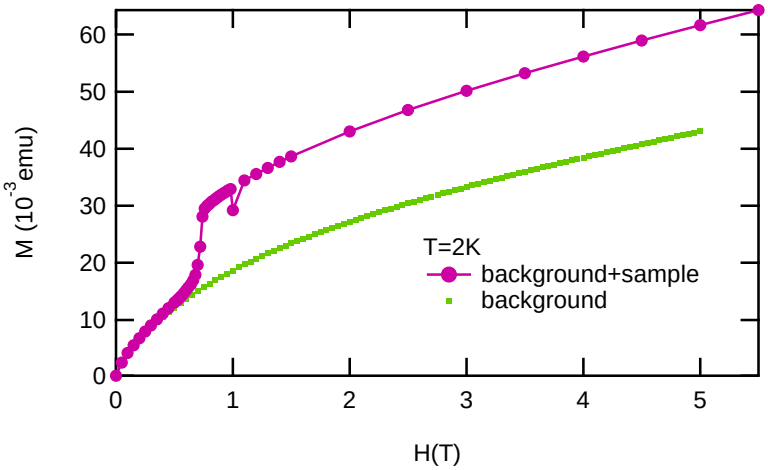

Figure 2.7: Magnetization of the empty cell (background), and with a sample of UCoAl inside. Here, $P = 0$.

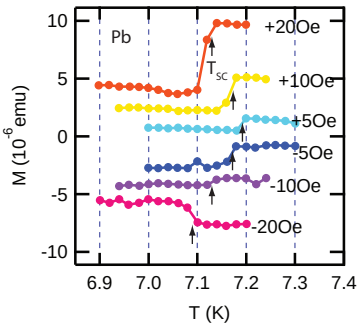

Figure 2.8: Magnetization vs temperature, at various constant fields, around the superconducting transition temperature of Pb. Arrows indicate the transition. The curves are shifted vertically for clarity.

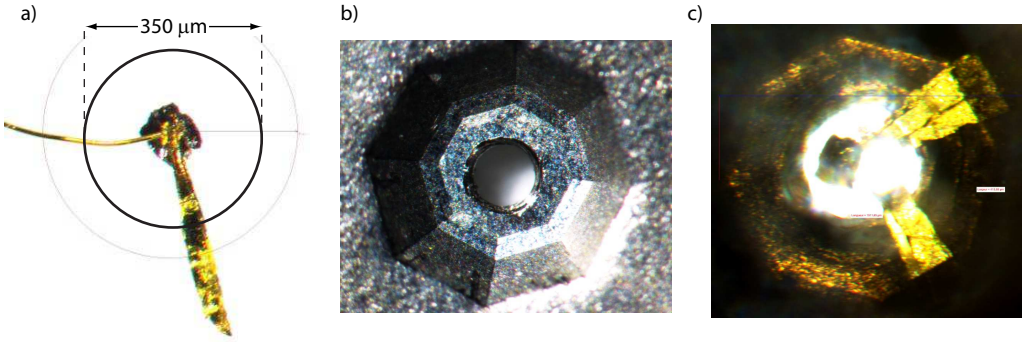

Figure 2.9: Diamond anvil cell pictures: a) sample of URhAl with thermocouple Au-AuFe for AC calorimetry; b) stainless steel gasket showing the footprint of the anvil and a hole of ø350 µm for the sample space; c) pressurized cell.

The pressure chamber consists of a hole drilled in a stainless steel gasket, clampled between two diamond anvils (Fig. 2.9-b). Liquid argon is used as a pressure transmitting medium.

The anvils are octogonal truncated pyramids, with a 700 µm wide plateau. First, the gasket is clamped once between the anvils, in order to get a crater in which the thickness of the gasket is reduced $\sim$ 100 µm. A ø350 µm hole is drilled at the center, and edges gently smoothed.

In order to allow electrical connections to squeeze in-between the gasket and the anvil, an insulating coating is made of an alumina-Stycast paste plated on the gasket. This operation follows a precise recipe: the density of the paste, the amount of paste deposited in the crater, the squeezing force, the baking temperature and time — all these are key parameters to obtain a hard enough, $\sim$ 30 µm thick coating. The connections are realized with gold stripes obtained from ø13 µm gold wires that are flattened between two glass plates with a hydraulic press. The final thickness is of the order of $\sim$ 1 µm.

In such a setup, the initial dimensions of the pressure chamber are ø350 µm by 130 µm. The sample size is typically ø170 µm by 60 µm thick. It is obtained by polishing, or cleaving. In the setup for AC calorimetry measurements, the thermocouple was realized by spot-welding two wires (Au-AuFe) on the sample (Fig. 2.9-a). The wires are squeezed onto the incoming stripes on closing the cell (Fig. 2.9-c).

The cell is closed in liquid argon, which serves as a pressure transmitting medium. A few ruby grains are trapped together with the sample. The pressure is determined by the fluorescence peak of ruby (which is pressure-dependent).

2.2.4 Changing the pressure in-situ

The AC calorimetry measurements were performed in a ^{4}He bath cryostat specially adapted to change the pressure *in situ* [34]. It is a cryo-pneumatic system fed with He gas and coupled to a force-amplifying lever stage, producing a force of several kN onto the pressure cell. It allows to change the pressure at low temperature. Hence this system allows to save a lot af time and liquid Helium consuption because it is not necessary to warm up the experiment to change the pressure. This consequently allows for very fine mapping of a phase diagram under pressure.

Pressure was increased in the pressure cell by pressurizing the bellow with He gas while monitoring the ruby fluorescence peak, until the desired pressure was reached. The bellow was then partially pumped in order to mechanically decouple the pressure cell from the thermal expansion of the gas inside the bellow, the pressure in the cell being maintained by the force-multipling lever system.

2.3 AC calorimetry

AC calorimetry is a technique which allows heat capacity measurement under pressure, while the relaxation method would be impossible due to the coupling of the sample to its environment. It is not a quantitative measurement since it is impossible to separate the sample contribution from the addenda, and to evaluate the power applied to the sample. But it provides a semi-quantitative information, which means that it is possible to compare curves between one another, provided that they are obtained in the same experimental conditions. In particular, it allows to determine the high pressure phase diagrams by a thermodynamical bulk probe. Here the AC calorimetry technique was used to draw the temperature – pressure phase diagram of URhAl (Chapter 4).

2.3.1 Principle of AC calorimetry

The sample is inside a diamond anvil pressure cell (DAC), which is transparent to visible light. The sample is heated by a laser which is chopped at a frequency ω in the kHz range. On the other side of the sample, a thermocouple measures the temperature oscillations T_{AC}. The amplitude R and the phase θ of the thermocouple signal are obtained by lock-in detection synchronized with the chopper. The amplitude of the signal is linked to the temperature oscillations T_{AC} through the thermoelectrical power of the thermocouple:

$$R = S_{th} T_{AC} \tag{2.1}$$

The basic model for AC calorimetry have been proposed by Sullivan *et al.* [35], and it is presented in Fig. 2.10. It is a first-order system, where the heat capacity C (sample + thermocouple) absorbs the power $P(t) = P_0\,(1 + \sin(\omega t))$, and relaxes to the bath

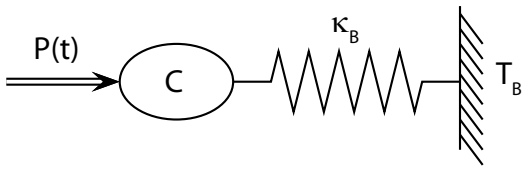

Figure 2.10: Simple model for AC calorimetry. The sample with a specific heat C receives the alternative power $P(t)$. It is coupled to the bath at the temperature T_B through a thermal leak of conductivity κ_B.

through a leak κ_B. C plays the role of a capacitance, and κ_B plays the role of the conductance. In this simple model we have:

$$T_{AC} = \frac{P_0}{\kappa_B + i\omega C} \tag{2.2}$$

In order to maximize the importance of C in comparison to κ_B in the signal, we should work at high frequencies. The main difficulty of the method in the pressure cell is that the power P_0 absorbed by the sample and the thermal leak κ_B are not known.

A more accurate model [36] takes into account the coupling κ_s between the thermocouple and the sample, which respectively receive a fraction of the power aP_0 and $(1-a)P_0$. In this case, there is a cut-off frequency at $\omega = \frac{\kappa_s}{C}$ above which the thermocouple starts to decouple from the sample. This typically limits the working frequency to the kHz range (in our experiment, we chose $\omega/2\pi = 1710\,\mathrm{Hz}$). Under such conditions, we can consider that:

$$C \propto \frac{P_0 S_{th}}{R} \tag{2.3}$$

Therefore the signal is inversely proportional to the total heat capacity C. At a phase transition, the specific jump of the sample will be detected as a jump in $1/R$. In the phase, the signature of a specific heat jump depends on the frequency, but in the region $\omega \approx \frac{\kappa_s}{C}$ it will appear as a positive jump in θ.

In order to get semi-quantitative data, the power received by the sample must be the same all along the experiment. But the defocusing of the laser beam throughout the optical path inevitably varies when working the mechanical system to change the pressure. The *ad hoc* solution consists in setting the laser power at the beginning of every scan so that to yield a DC temperature rise of 0.3 K above the bath temperature.

Another source of uncertainty is the thermoelectrical power of the Au:AuFe thermocouple, which is not known under pressure. We suppose it has low pressure dependence in our study. The thermocouple response also varies from one thermocouple to another. Because our thermocouple had not been calibrated, we applied a model reponse (Fig. 2.11) which is a fit obtained out of several thermocouple calibrations. As we can see, the temperature dependence of the thermocouple is particularly strong below 10 K.

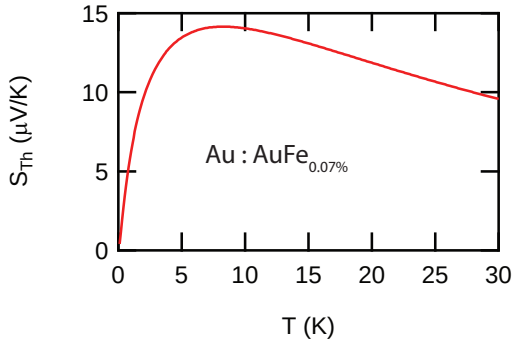

Figure 2.11: Thermocouple response used in the analysis of AC calorimetry data. This model was obtained by fitting an average over several different thermocouple calibrations.

2.4 Strain gauge dilatometry

Strain gauges are used for dilatation measurements. A strain gauge is a flexible foil supporting a long thin conducting path forming a zig-zag pattern. The strain gauge is glued on the surface of a sample (Fig. 2.13) to follow its deformation (=strain)[3]. The strains along the conductive pathway induce variations of the resistance ($R = \rho l/\sigma$).

The design of a strain gauge is such that it is unidirectional: it is sensitive to strains along the direction of the long thin parallel sections of conductor, while the short thick turns have a negligible contribution to the total resistance.

The response to a strain ϵ is:

$$\frac{\Delta R}{R} = \kappa\epsilon \tag{2.4}$$

where R is the resistance of the gauge and κ is the gauge factor (generally $\kappa \approx 2$).

We used standard commercial millimeter-size strain gauges (Kyowa), made of Ni-Cr alloy. The gauge must be tightly bound to the material, using a special cement (Kyowa PC-6).

The strain gauge is set in a Wheatstone bridge (Fig. 2.12) along with a «dummy» gauge, which is placed in the same conditions, so that to compensate the drift with temperature, field, pressure. This is called *active dummy method*. The dummy gauge is sticken on a piece of silicon, which has very low thermal expansion below 40 K. The other half of the bridge (outside the cryostat) consists of two simple resistors R_0 (which are chosen for their temperature stability), and a variable resistor (actually a decade box of resistors, which is more stable) mounted in parallel with one of the two resistors, to balance the bridge.

[3]do not confuse: a *strain* (synonym of *deformation*) is a relative variation of length (unitless), whereas a *stress* is a force per unit surface (dimension of a pressure).

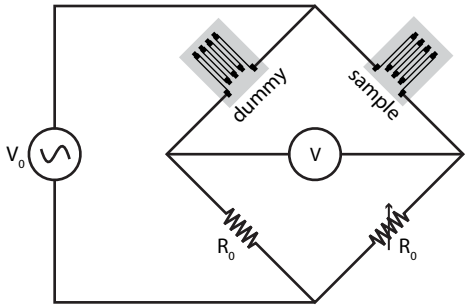

Figure 2.12: Electrical circuit with two strain gauges mounted in a Wheatstone bridge.

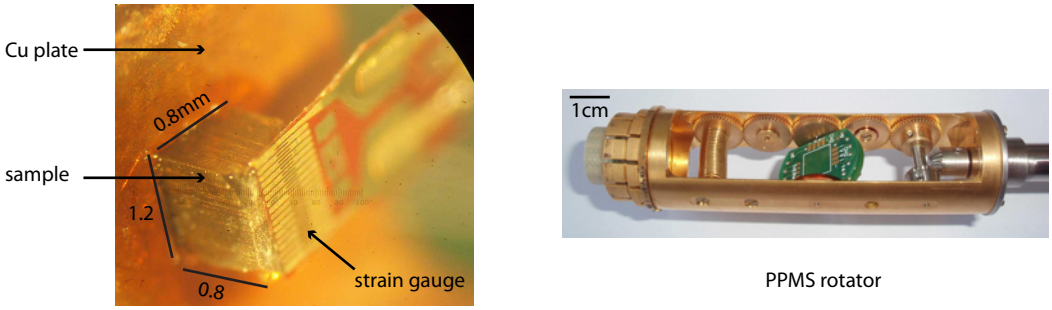

Figure 2.13: Picture of a strain gauge sticken on a sample of URhSi. The setup is mounted on a PPMS rotator.

When the bridge is balanced ($V \approx 0$), the signal is proportional to the variation of the straing gauge:

$$\frac{\Delta V}{V_0} = \frac{RR_0}{(R+R_0)^2}\frac{\Delta R}{R} \tag{2.5}$$

The resistors are normally chosen with value $R_0 \approx R$ (standard values are $120\,\Omega$ or $350\,\Omega$), so that the bridge factor reduces to $1/4$, and we have the simple relation for the strain $\epsilon = \frac{\Delta l}{l}$:

$$\frac{\Delta l}{l} \approx \frac{4}{\kappa}\frac{\Delta V}{V_0} \tag{2.6}$$

which is independent of the bridge resistances.

The measurements are performed with a lock-in detection at $\sim 17\,\mathrm{Hz}$. Typical value of the bridge excitation voltage is $V_0 = 0.1\,\mathrm{V}$, so that the power dissipated by the strain gauge is $< 0.1\,\mathrm{mW}$. A dilatation of 10^{-4} will thus produce a signal of $5\,\mu\mathrm{V}$.

This method can be used down to $T \sim 5\,\mathrm{K}$. At lower temperatures, the thermal drift of the strains is very large and the compensation cannot be achieved.

Chapter 3

URhSi

3.1 Introduction

URhSi attracted our attention because it is very similar to the ferromagnetic superconductor URhGe, with a FM ground state below $T_C \approx 10\,\mathrm{K}$ and a spontaneous moment of $\approx 0.5\,\mu_B$ along the c-axis (see e.g. [37]). The main target of our study was to test whether URhSi can also be tuned to a ferromagnetic quantum phase transition by applying magnetic field perpendicular to the easy magnetization axis (c-axis), as it is the case in URhGe [29].

3.2 Context

URhSi was first reported in 1988 [38], with X-ray powder diffraction establishing the orthorhombic structure (first believed to be $CeCu_2$-type, very close to TiNiSi-type) and magnetic measurements on polycrystalline samples establishing the FM ground state.

In the 90's, specific heat measurements showed a large jump at the FM transition at $T_C \approx 10\,\mathrm{K}$, and different γ values of $\sim 130 - 160\,\mathrm{mJ.mol^{-1}.K^{-2}}$ are found in the literature [37, 39], with still a significant magnetic contribution to C/T at $\sim 1\,\mathrm{K}$. In spite of the uncertainty on the electronic contribution to the specific heat, the authors could infer a rather small integrated value of the magnetic entropy $S_m \approx 0.1 - 0.2R\ln 2$, suggesting the itinerant nature of the magnetic moments. Furthermore, de Boer *et al.* [39] have reported an upturn of C/T on cooling below 0.6 K, most likely due to the nuclear contribution.

A large negative magnetoresistance of URhSi around T_C was reported, both in a polycrystal [40] and in a single crystal sample with field applied along c [37]. This was attributed to the rapid suppression of magnon scattering.

There has been a controversy about the value of the spontaneous moment ($0.11\,\mu_B$ [41], $0.27\,\mu_B$ [40]), which was partially settled in 2003 with magnetization and neutron

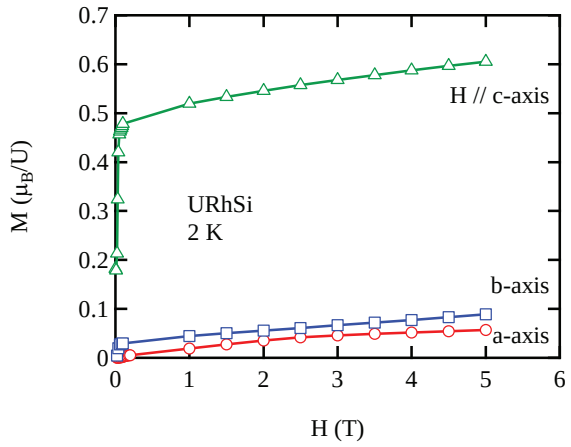

Figure 3.1: (courtesy of D. Aoki) Magnetization vs field in URhSi along the main crystallographic directions.

diffraction experiments on single crystal samples [42], who found 0.58 μ_B along the c-axis. Even then, there remained an ambiguity concerning the magnetic anisotropy since these magnetization experiments found a sizeable spontaneous component of $\sim 0.1\,\mu_B$ along a- and b- axes, suggesting a tilt of $\vec{\mu}$ off the easy axis, while neutron data [42, 43] only found collinear moments. One should note that all these experiments were performed on the same sample.

In our laboratory, new single crystal M-H measurements were performed using a rotator, since the detection of a magnetic component in the hard a-b plane is very sensitive to the field angle. Figure 3.1 shows the magnetization curves at 2 K along the principal axes. The results seem to lift the controversy : there is no spontaneous moment along a, and although a small spontaneous moment ($0.03\,\mu_B$) still remains along b-axis, these results seem to be basically consistent with the results of neutron experiments. It indicates that URhSi has a uniaxial magnetic anisotropy, but unlike URhGe (Fig. 1.7) there is no intermediate axis. It should be noted that the first nearest U atoms form zig-zag chains along the b axis in URhSi, while the zig-zag chain in URhGe is along the a axis, which may explain the different susceptibility along b.

3.3 Experimental results

3.3.1 Sample preparation

Crystal growth :

Several crystal growths were performed in order to get the best sample quality as possible. Starting material was depleted U (99.9% – 3N), Rh (3N) and Si (5N) in stoichiometric proportions. The components were melt in a tetra-arc furnace under Ar

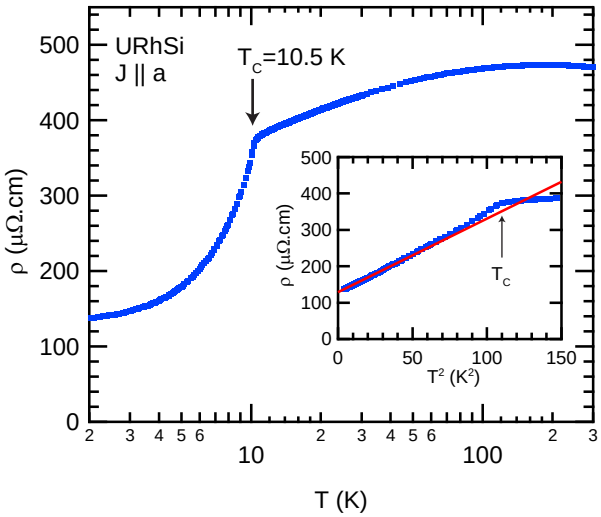

Figure 3.2: Resistivity vs temperature of URhSi, from 300 K to 2 K (logarithmic scale) measured on a bar-shape sample of RRR = 3.5, with current along a-axis. The arrow indicate the Curie temperature. Inset shows the data plotted against T^2, and a solid line shows a T^2 fit of the lowest temperature.

gas atmosphere, or in a radio-frequency furnace under ultra-high vacuum. Several ingots were pulled by Czochralski method with pulling rate of 15 mm/h. The single crystal was checked by X-ray Laue photograph, and the high-temperature phase with orthorhombic TiNiSi-type structure was obtained (there is also a low-temperature phase of URhSi [44]).

3.3.2 Resistivity

Fig. 3.2 shows the resistivity versus temperature measured from 300 K to 2 K on a bar-shape sample of URhSi, with current along a-axis. The residual resistivity ratio of the sample is ~ 3, which is poor but no better samples were obtained by other groups (to our knowledge).

The resistivity is rather flat down to the Curie temperature $T_C = 10.5$ K, below which it drops dramatically. At low temperature, the data can be fitted with a $\rho = \rho_0 + AT^2$ up to ≈ 7 K, then it deviates on approaching T_C. The obtained coefficient is $A = 2.0\,\mu\Omega.\mathrm{cm/K^2}$. This contrasts with the results of Prokeš *et al.* [37] who found a better fit with a $T^{\frac{5}{3}}$ law which is typical of spin-fluctuations close to FM instability.

This T^2 temperature dependence of resistivity is typical of FM metals. If local magnetic moments are considered, as it is almost the case for $T > T_K$, in a lattice of Heisenberg spins coupled with conduction electrons by exchange interaction J, perturbative development leads a magnetic contribution: $\rho_{\mathrm{mag}}(T) \propto |J|^2$, which is temperature-independent above T_C. In the FM state, typical spin-wave dispersion relations yield

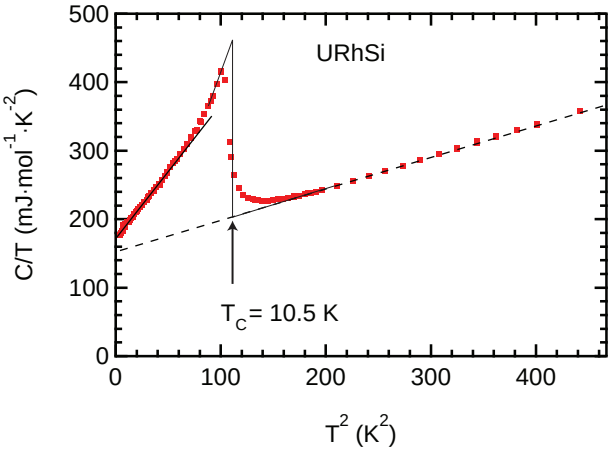

Figure 3.3: C/T vs T^2 of URhSi. The value of $T_C = 10.5\,\mathrm{K}$ is obtained by equal entropy partition (thin solid path). Fits to equation 3.1 are represented by the solid line (low temperature) and dashed lines ($T > T_C$).

$\rho_{\mathrm{mag}}(T) = A_{\mathrm{mag}}T^2$ [45].

Below T_C, the pseudo-parabolic temperature dependence of ρ which changes brutally at T_C therefore indicates that the magnon scattering contribution accounts for a large part of the A coefficient.

3.3.3 Specific heat

Heat capacity was measured in a PPMS (Quantum Design) by the relaxation method, between 2 K and 50 K, using $\approx 10\,\mathrm{mg}$ samples with a flat surface and Apiezon N grease for thermal contact. Heat capacity of URhSi is shown in a C/T vs T^2 plot (Fig. 3.3). The heat capacity shows a sharp peak at 10.5 K which is attributed to the PM-FM transition. At low temperature, C_p/T vs T^2 is successfully fitted by a straight line between 2 and 5 K according to the law:

$$C_p = \gamma T + \beta T^3 \tag{3.1}$$

with the value of the Sommerfeld coefficient $\gamma \approx 170\,\mathrm{mJ \cdot mol^{-1} \cdot K^{-2}}$, and the coefficient $\beta = 1.95\,\mathrm{mJ \cdot mol^{-1} \cdot K^{-4}}$ (which accounts for both lattice and magnetic contributions), in good agreement with the literature [37]. Above T_C, C_p/T vs T^2 can be also fitted by equation 3.1 with slightly lower $\gamma \approx 150\,\mathrm{mJ \cdot mol^{-1} \cdot K^{-2}}$, and $\beta = 0.46\,\mathrm{mJ \cdot mol^{-1} \cdot K^{-4}}$.

With the γ value below T_C and the A coefficient of resistivity determined before, the Kadowaki–Woods ratio $A/\gamma^2 \approx 70\,\mu\Omega.\mathrm{cm.(mol.K/J)^2}$ is almost one order of magnitude larger than for typical heavy fermion systems ($10\,\mu\Omega.\mathrm{cm.(mol.K/J)^2}$). This is probably because of the large magnon scattering contribution dominating the A coefficient.

The change of the β coefficient is ascribed to the magnetic contribution below T_C. Theoretical models predict a $T^{3/2}$ law for ferromagnetic magnons, logarithmic contribution for spin fluctuations in weak itinerant ferromagnets [46], and exponential behaviour in the case of gapped magnons [47], but none of these model could be singled out, owing to the lack of knowledge of the other contributions. The change of γ on either side of T_C is not surprising since electronic correlations are probably affected by the onset of magnetic order.

3.3.4 Thermal expansion with fine tuning of field direction

The main motivation of our study was to test if URhSi could be driven to a ferromagnetic instability by applying a magnetic field along b, like the closely related material URhGe, since they have many similarities. We chose to track T_C by measuring thermal expansion — which is a thermodynamical property — along the main crystallographic directions using strain gauges. The strain gauges were glued on the surfaces of a cubical single crystal sample of URhSi with dimensions $0.8 \times 1 \times 1.2\,\mathrm{mm}^3$. We measured the thermal expansion using a Wheatstone bridge with a «dummy gauge» glued on a piece of silicon in order to compensate for the temperature drift of the strain gauge.

Furthermore, it is important to have a precise alignement of the sample with respect to the field direction, since a tiny field component along the c-axis is known to kill the transverse spin fluctuations that are the driving force for FM instability in URhGe and UCoGe. In order to achieve the condition $\vec{H} \perp c$, the sample was mounted on a 1-axis rotator so that to have *in situ* control of the field angle in the $b - c$ plane.

3.3.5 Results

Thermal expansion of URhSi along the main crystallographic directions, at zero field, is shown in Fig. 3.4. A linear trend and an offset were substracted from the curves so that they match to zero above the Curie temperature. It is reasonable to do so because:

- the offset depends on the balance of the Wheatstone bridge
- the temperature drift of a strain gauge response being large in this temperature range, it is very unlikely to achieve perfect compensation with the dummy gauge.

The thermal expansion changes radically at T_C. On entering the FM phase, URhSi expands along the c- and a-directions and contracts along the b-direction. As infered from Fig 3.4, the jumps of thermal expansion coefficients α are negative along a and c axes, and positive along the b axis. Thus the thermal expansion in volume will be negative, which is consistent with the fact that T_C decreases with pressure [48], because of Ehrenfest relation. At least for the b- and c- directions, the thermal expansion seems

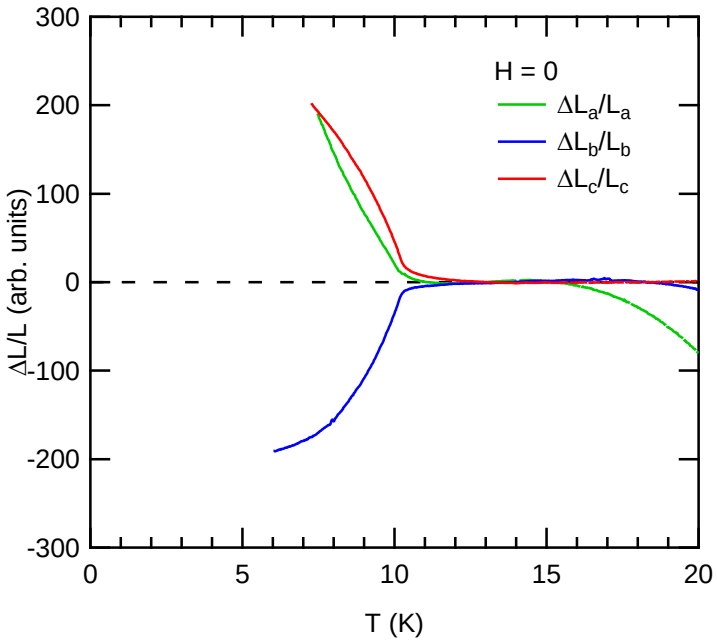

Figure 3.4: Thermal expansion of URhSi, measured with strain gauges along the crystallographic directions a, b and c.

to scale with magnetization. The data is not relevant below $\sim 5\,\mathrm{K}$, which is the lower limit for the strain gauge technique.

Magnetic field was applied along the b-direction. Temperature scans were performed at various angles by moving the rotator step by step, repeating the procedure for each strain gauge and every field value. The effect of field angle is illustrated in Fig. 3.5, showing thermal expansion curves $\Delta L_b/L_b$ at 9 T for various field angles around the perpendicular configuration. The curve with sharpest transition corresponds to the situation where $\vec{H} \perp \vec{c}$. When the field angle deviates from the $\vec{H} \perp \vec{c}$ situation, the transition broadens and T_C increases. In this example, with a field of 9 T along the b-axis, a misorientation of $0.25\,^\circ$ gives a field projection along the c-axis $H_{\|c} = 0.04\,\mathrm{T}$ which is already too much to observe the decrease of T_C. Such extreme field angle dependence was also observed in URhGe [27] and UCoGe [28], where a misalignement of less than $1\,^\circ$ kills the fluctuation-induced superconductivity. This fact stresses the necessity of having precise control over the sample orientation.

Figure 3.6 shows the temperature dependence of thermal expansion coefficients along the b and c axes, in the optimum angle configuration found by working the rotator to obtain the sharpest and lowest transition temperature. The most important result of these thermal expansion experiments is the fact that T_C decreases with $\vec{H} \parallel \vec{b}$. From $T_C = 10.5\,\mathrm{K}$ at zero field, T_C decreases to 9.5 K at 9 T, which was the maximum field available for this experiment. The evolution of T_C versus $H \parallel b$ is summarized in Fig.

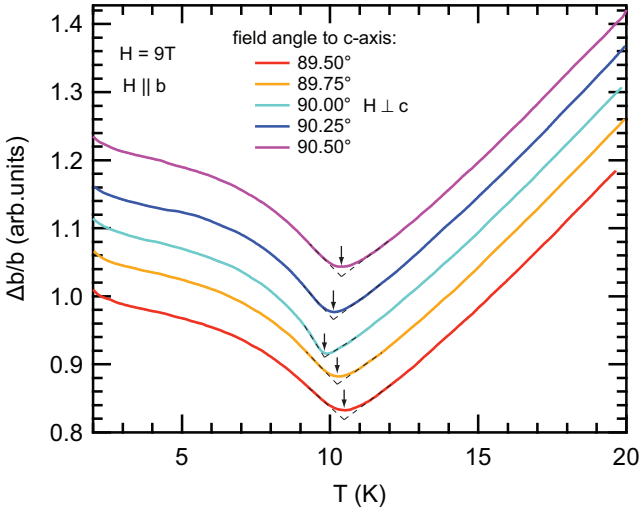

Figure 3.5: Thermal expansion along the b-axis, with a field of 9 T applied along the b-axis. The sample was mounted on a 1-axis rotator with angle varying from c- to b-axis by ± 0.25 deg steps around the $\vec{H} \perp \vec{c}$ position. Curves are shifted vertically for clarity.

3.7, drawing the H–T phase diagram of URhSi. The data points obtained from both b- and c-direction thermal expansion curves are in good agreement. After a low initial evolution, the decrease of T_C is more pronounced above 5 T.

3.3.6 discussion

The decrease of T_C is related to enhanced magnetic fluctuations along b–direction. The evolution of T_C up to 9 T is comparable to the case of URhGe, though the decrease is slower in URhSi. The decrease of T_C is theoretically explained by V. P. Mineev [49] on the basis of Ginzburg-Landau theory, when the field is applied perpendicular to the easy magnetization axis. According to this theory, the decrease of T_C is described by:

$$\Delta T_C \propto -H^2 \tag{3.2}$$

Our data can be fitted with this equation (see Fig. 3.7).

Further studies were performed at high fields by W. Knafo (LNCMI-Toulouse) by measuring magnetoresistivity and magnetization of URhSi with $H \parallel b$, but without rotator. His results (in proceedings of SCES2013) show a maximum in magnetoresistance around $H_\rho^{\max} = 42$ T at ~ 2 K (Fig. 3.8). It is associated to an anomaly in magnetization, such as in URhGe or UCoGe ([50]). As temperature increases, this anomaly shifts to lower field, until it collapses at 10 K in URhSi.

Figure 3.9-a shows the T-H phase diagram of URhSi built from the high-field resistivity data of W. Knafo and our thermal expansion data. There is a continuity between

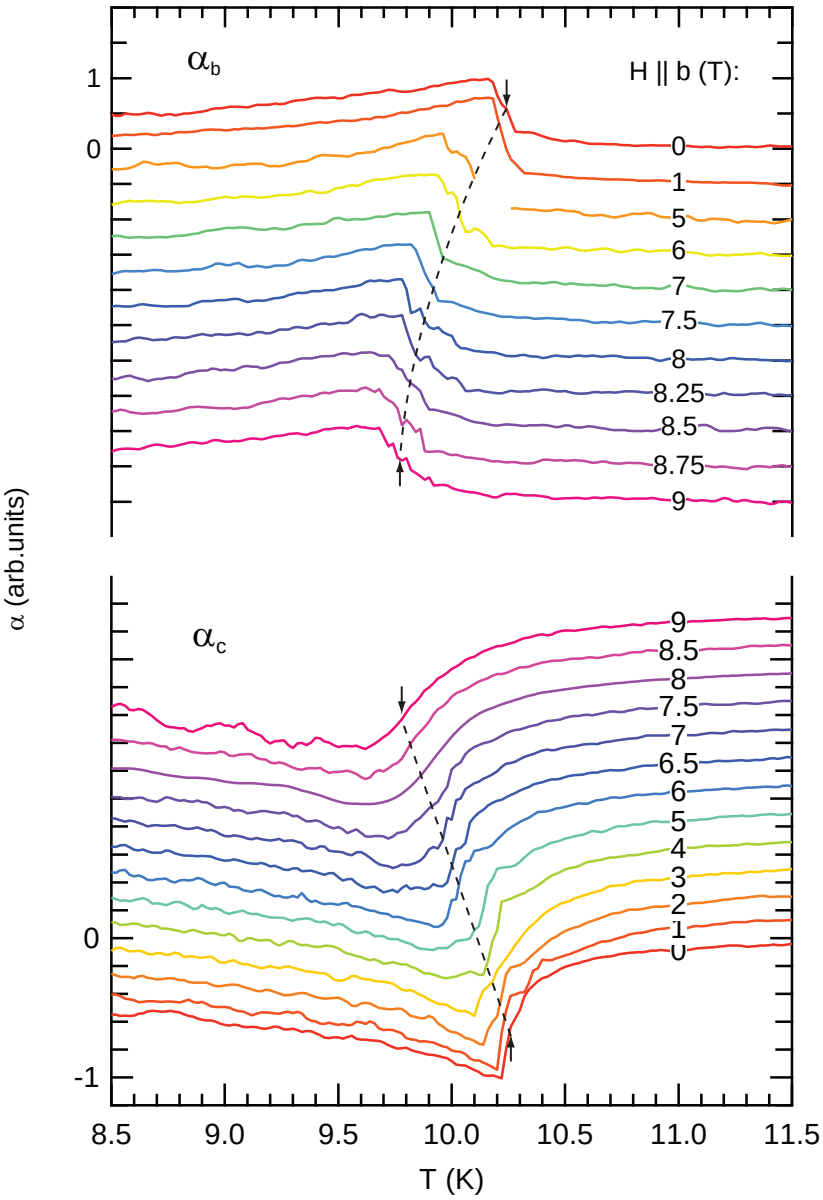

Figure 3.6: Field dependence of the thermal expansion coefficients along the b- and c-axes. Field was applied along b, and the sample was mounted on the rotator to ensure the $\vec{H} \perp \vec{c}$ condition. Curves are shifted vertically for clarity.

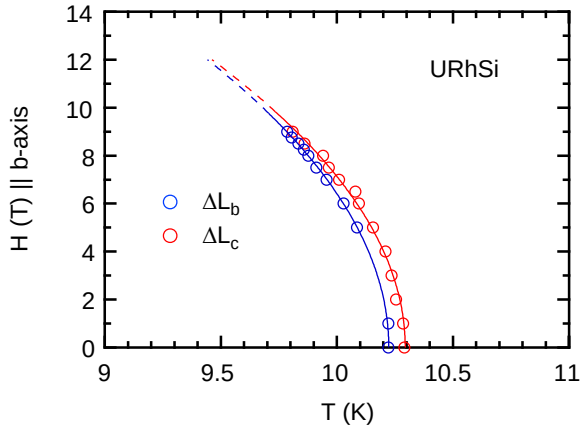

Figure 3.7: Field–temperature phase diagram of URhSi obtained from α_b and α_c curves of Fig. 3.6, for field applied along b, with the condition $\vec{H} \perp \vec{c}$ respected. Lines are fits using the relation $(T_C - T_{C0}) \propto (-H^2)$.

our data and the maximum of the derivative of $\rho(H)$, namely $H^{\max}_{\partial\rho/\partial H}$. Reciprocally, the fit of our data using Eq. 3.2 yields an extrapolated value at $0\,\mathrm{K}$: $H(0) \approx 43\,\mathrm{T}$, in excellent agreement with the maximum of magnetoresistance. It would be interesting to follow the magnetoresistance anomaly using a rotator, to clarify whether T_C connects to $H^{\max}_{\rho}$ or with $H^{\max}_{\partial\rho/\partial H}$. Nevertheless, it seems already clear that the high-field anomaly in magnetoresistance is connected to T_C at low field.

This is also the case in URhGe, but not in UCoGe. In the case of UCoGe, a similar anomaly in magnetoresistance occurs at $\approx 50\,\mathrm{T}$ at low temperature, and is connected at high temperature to a maximum in magnetic susceptibility rather than to T_C : $(T^{\max}_{\chi} \approx 35\,\mathrm{K}) \gg (T_C \approx 3\,\mathrm{K})$ (see Fig. 3.9-b). On the contrary, there is no such $\chi^{\max}$ in the case of URhSi and URhGe.

3.4 Conclusions

We obtained single crystals of URhSi with which we performed resistivity, heat capacity, and thermal expansion measurements.

Our resistivity and heat capacity data confirm the existence of a FM transition at $10.5\,\mathrm{K}$. A Fermi liquid behaviour is observed in below $\sim 6\,\mathrm{K}$, with a large magnon contribution to the resistivity. Our specific heat data follows the law $C/T = \gamma + \beta T^2$ in the FM phase, with a γ value of $\approx 170\,\mathrm{mJ \cdot mol^{-1} \cdot K^{-2}}$, which is higher than the one extrapolated from the PM phase ($150\,\mathrm{mJ \cdot mol^{-1} \cdot K^{-2}}$), in agreement with the literature. This is ascribed to a significant magnetic contribution to the specific heat at $2\,\mathrm{K}$.

The thermal expansion measurements The main result of our study on URhSi is the decrease of T_C by applying a magnetic field along b, and the high sensitivity to the field

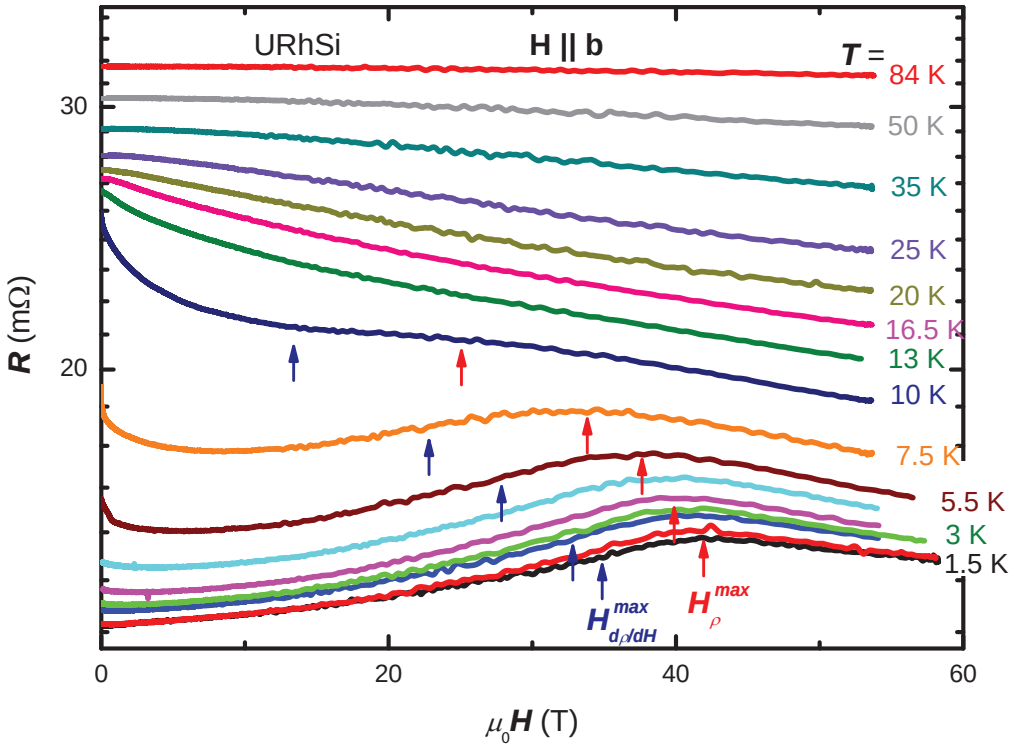

Figure 3.8: Pulsed-field magnetoresistance of URhSi with $H \parallel b$, for various temperatures (1.5 to 50 K). Courtesy of W. Knafo (LNCMI-Toulouse) (unpublished).

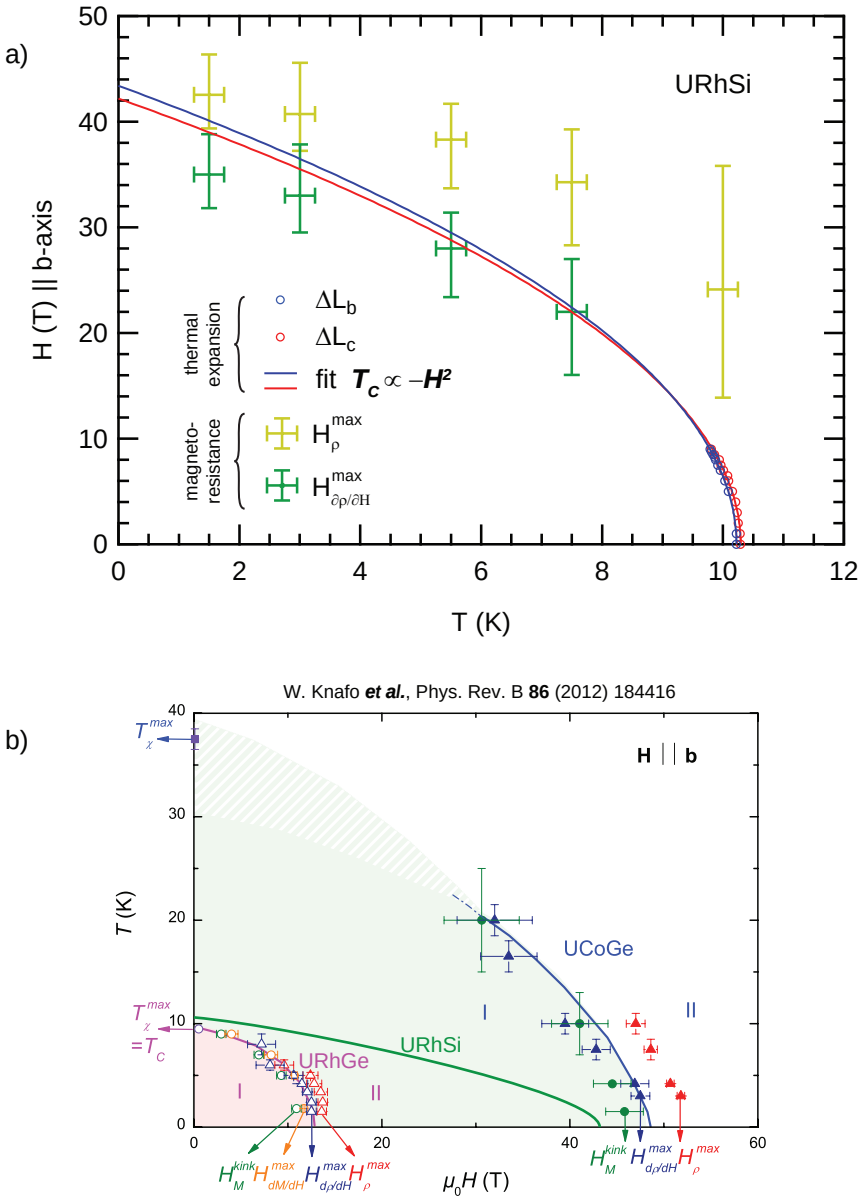

Figure 3.9: a) Field–Temperature plot of the high field magnetoresistance anomaly ($H_\rho^{\max}$ and $H_{\partial\rho/\partial H}^{\max}$) (courtesy of W. Knafo, LNCMI-Toulouse) and the Curie temperature measured by thermal expansion with a rotator (circles). Lines are fits of the thermal expansion data using the relation $(T_C - T_{C0}) \propto (-H^2)$. b) Temperature–field phase diagram of URhGe and UCoGe taken from Ref. [50], with the line representing $T_C|H_{\partial\rho/\partial H}^{\max}$ of URhSi added on top.

orientation. We can therefore think of URhSi as a system driven towards FM instability by spin fluctuations, like URhGe and UCoGe: a field along b enhances the fluctuations, but a small component of H along c stabilizes the moments in the easy direction and kills the fluctuations.

Finally, we show that the high-field magnetoresistance anomaly measured by W. Knafo along the b axis is in the continuity of T_C, thus suggesting that URhSi is tuned to a FM instability at $H_{\|b} \approx 43\,\mathrm{T}$. Further efforts should be devoted to improve the quality of the crystals of URhSi, since the $RRR \sim 3$ at the present stage is too low to expect any superconductivity.

Chapter 4

URhAl

URhAl belongs to the UTX family (T = transition metal , X = p-element), and has the layered hexagonal *ZrNiAl*-type structure (Fig. 1.4), which is the most common structure in the UTX family. The inter-U distance $d_{\text{U-U}} = 3.63\,\text{Å}$ is in the upper Hill limit region, and the ground state is FM below $T_C \approx 27\,\text{K}$, with a moment $M_0 \approx 0.9\,\mu_\text{B}$ per U-atom along the c-axis with a huge uniaxial anisotropy [51].

Since Rh is located just below Co in the periodic table, and given the larger lattice constants compared to UCoAl, one can naively infer that URhAl corresponds to the negative pressure case of UCoAl. Therefore, the suppression of T_C by applying pressure can be expected. Pressure studies of the lattice parameters of URhAl at room temperature [52] have reported a linear compressibility $\kappa_a \approx 2.8 \times 10^{-3}\,\text{GPa}^{-1}$ along the a-axis, and negligible along the c-axis. Reported pressure dependence of T_C by AC susceptibility measurements on URhAl [53] pointed to a quasi neglible pressure dependence of T_C up to 6 kbar. Our study was aimed to investigate this compound under high pressure for the first time, to establish the phase diagram of URhAl, and to check the existence of a quantum phase transition at a reachable pressure.

4.1 Present state of knowledge on URhAl

4.1.1 Anisotropic hybridization

Magnetization density obtained with polarized neutron experiments [54] have shown that a considerable portion ($\sim 30\%$) of the total magnetization is induced on the Rh atoms that lie in the U-Rh plane, but not on the equidistant Rh atoms that lie in the Rh-Al plane. Furthermore, these polarized neutron results give an orbital-to-spin moment ratio $\mu_L/\mu_S = -1.81$ (later confirmed by XMCD studies [55]) which is reduced compared the free ion value (~ 3). These observations suggest a large degree of delocalization of the $5f$ electrons by hybridization with the Rh $4d$ electrons, which explains the large magnetic

anisotropy of URhAl.

4.1.2 Band structure calculations

Ab initio LSDA-based band structure calculations of URhAl were performed by several groups [56–60]. These studies indicated that the U $5f$ - Rh $4d$ hybridization plays a dominant role in the bonding and in the magnetic properties, and successfully accounted for many properties such as lattice volume and compressibility, magneto-crystalline anisotropy, and could reproduce reasonably well the shape of the XMCD and Kerr spectra [55, 61]. The γ-value arising from band structure calculations amounts to $\approx 45\,\mathrm{mJ.mol^{-1}.K^{-2}}$, which would mean a many-body effect enhancement of ~ 1.5 in the experimental value ($\approx 67\,\mathrm{mJ.mol^{-1}.K^{-2}}$ [62]). The main shortcoming of the LSDA-based band calculations in URhAl is the largely underestimated value of the total magnetic moment, even when introducing on-site repulsion (LSDA+U) and orbital polarization corrections (LSDA+U(OP)).

4.1.3 Localized vs itinerant picture

As for many other U-based compounds, URhAl has the puzzling particularity of behaving like a localized or an itinerant magnetic system depending on which property we look at. Several spectroscopy studies were reported on URhAl that illustrate the localized/itinerant duality:

On the one hand, inelastic neutron scattering experiments showed a peak at 380 meV, interpreted as the signature of an inter-multiplet transition, thus promoting the localized picture. [63] On the other hand, the magneto-optical Kerr spectrum measured on URhAl was reported to compare quite well with the calculated spectrum based on the assumption of delocalized $5f$ electrons. [57, 61]

In order to find a compromise, Oppeneer *at al.* speculated that the $5f$ electrons in URhAl might be divided into two groups, based on the strongly anisotropic $5f$-ligand hybridization: the possible inter-multiplet transition concerns the rather localized $5f$ electrons out of the plane, whereas Kerr spectroscopy probes the rather delocalized $5f$ orbitals in the plane.

4.2 Sample characterization

The crystal growth of URhAl was very successful and the ingot was single crystal all through, as attested by Laue photographs, with the c-axis along the pulling direction. Various samples of single crystal URhAl were characterized by resistivity and heat capacity measurements. All samples showed the FM transition at $T_C \approx 28\,\mathrm{K}$. The residual resistivity ratio of the different crystals is around 12.

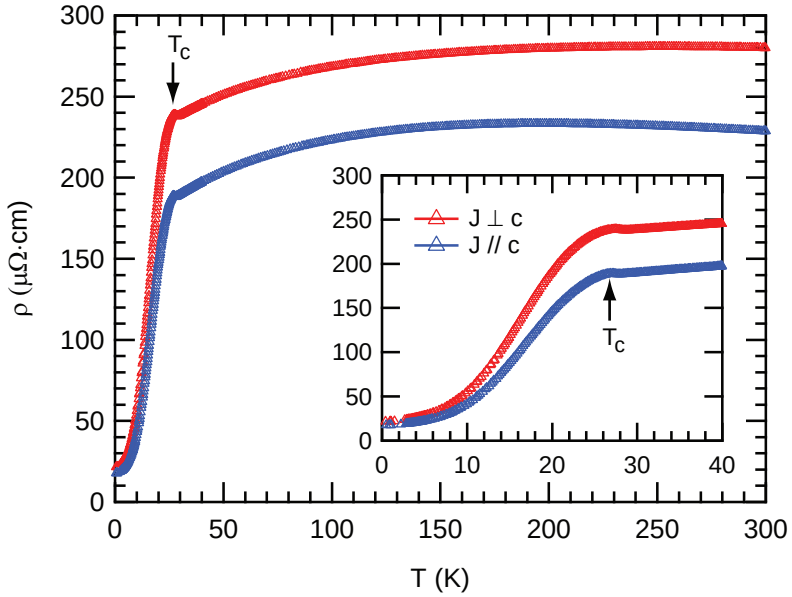

Figure 4.1: Resistivity of URhAl with current along the reciprocal $a^\star$ direction (red symbols) and c direction (blue symbols). Inset focuses on the low temerature part. Arrows indicate the Curie temperature.

4.2.1 Resistivity

Figure 4.1 shows the temperature dependence of the resistivity along two different crystallographic directions. In a wide temperature range (300 K – 30 K), ρ is almost temperature independent. There is a sharp change around 28 K which corresponds to the Curie temperature. ρ drops dramatically on cooling below T_C, like in the ferromagnet URhSi (see 3.3). A small hump at T_C could indicate a drop of the carrier number, suggesting the opening of a gap in the Fermi surface.

Finally, URhAl obeys the Fermi liquid model over a wide temperature range with the T^2 law of resistivity being valid up to 6.2 K. Inelastic terms $A_{J\perp c} = 0.27$ and $A_{J\parallel c} = 0.19\,\mu\Omega.\mathrm{cm.K}^{-2}$ are probably largely due to the magnon contribution, as in URhSi (see Chapter 3).

4.2.2 Heat capacity

The heat capacity of URhAl (Fig. 4.3) shows a peak at $T_C = 27.5$ K, in good agreement with resistivity (Fig. 4.1) and magnetization (Fig. 4.6). The T-linear term of $C(T)$ amounts to $\gamma = 76\,\mathrm{mJ.mol}^{-1}.\mathrm{K}^{-2}$, which is that of a moderate heavy fermion system. In URhAl, there is no broad hump like in UGe_2 associated to the crossover between FM_1/FM_2 phases at $T^\star \approx \frac{T_C}{2}$, neither in C/T vs T nor in ρ vs T. This suggests a single

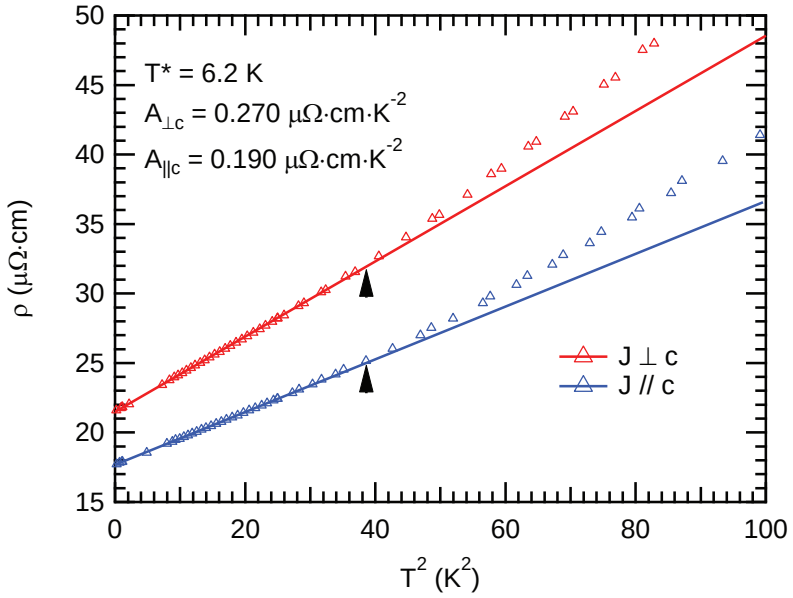

Figure 4.2: Resistivity of URhAl vs T^2 for current along a^* (red symbols) and c-axis (blue symbols), and their respective low-temperature fit (straight lines). The T^2 fit is valid up to $T^\star \approx 6.2\,\mathrm{K}$ for both directions, with elastic scattering coefficients $A_{J\perp c} = 0.27$ and $A_{J\parallel c} = 0.19\,\mu\Omega.\mathrm{cm.K}^{-2}$.

FM phase for URhAl.

The Kadowaki-Woods ratio $A/\gamma^2 = 33$ and $47\,\mu\Omega.\mathrm{cm.(mol.K/J)}^2$ for the current $\parallel$ and $\perp$ to the c-axis, respectively. This is several times larger than the value of $10\,\mu\Omega.\mathrm{cm.(mol.K/J)}^2$ found for «heavier» systems UPt_3, $CeCu_2Si_2$, $CeCu_6$ etc. It is probably because the A coefficient of resistivity is largely dominated by the magnon scattering contribution.

4.2.3 Thermal expansion

Thermal expansion measurements were performed on URhAl along the c- and a-axes, using strain gauges (see section 3.3.4 for experimental details). Results are presented in Figure 4.4.

The thermal expansion curves $\frac{\Delta L}{L}$ vs T were normalized to 0 just above T_C (Fig. 4.4-a). On entering the FM phase, there is a dilatation along c which amounts to 10^{-4} at 10 K and a contraction perpendicular to c which amounts to -0.5×10^{-4}. The volume expansion $\frac{\Delta V}{V} = \frac{\Delta L_c}{L_c} + 2\frac{\Delta L_a}{L_a}$ is close to zero, suggesting a flat initial pressure dependence of T_C via Ehrenfest relation, in good agreement with the reported value ($\partial T_C/\partial P = -0.03\,\mathrm{K.GPa}^{-1}$) [53]. The temperature derivatives of the $\frac{\Delta L}{L}$ curves, i.e. the thermal expansion coefficients α_c and α_a, are plotted in Figure 4.4-b. On approaching

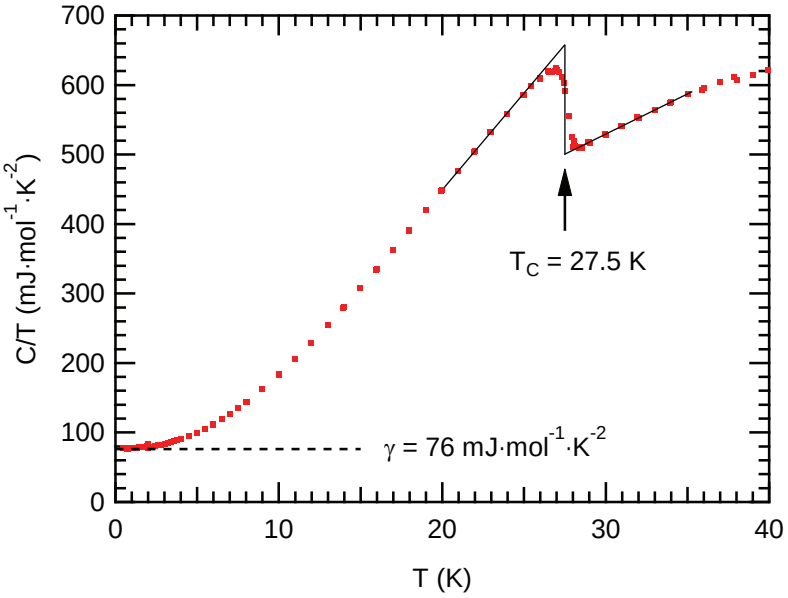

Figure 4.3: Heat capacity of URhAl as C/T vs T. A specific heat jump occurs at the Curie temperature $T_C = 27.5\,\mathrm{K}$, and the Sommerfeld coefficient γ amounts to $76\,\mathrm{mJ.mol^{-1}K^{-2}}$.

T_C from the FM phase, there is a little enhancement of α_c above 22 K. At the transition, the change of α is very sharp.

4.3 Magnetic properties

Magnetic measurements on URhAl were performed using a commercial SQUID magnetometer (*MPMS, Quantum Design*) down to 2 K and up to 5.5 T.

The Ising-type nature of URhAl is shown in Fig. 4.5 which shows the field dependence of the magnetization at $T = 2\,\mathrm{K}$. The saturation magnetization of $0.9\,\mu_\mathrm{B}$ along the c-axis (with a hysteresis loop when sweeping between positive and negative field) contrasts with the low, linear magnetic response when $H \perp c$.

The PM-FM transition appears around 28 K on the field-cooling magnetization curves (Fig. 4.6). At low field ($H << 0.1\,\mathrm{T}$), there is a sharp increase of $M(T)$ just below T_C saturating at a value which is far below $M_0 = 0.9\,\mu_\mathrm{B}$ probably because of the partial cancellation of FM domains. There is an anomaly around 25 K suggesting a two-step transition, probably due to domain walls blocking on crystalline defects. At 0.1 T, the sample seems single domain since the magnetization saturates at M_0. At higher field ($H > 0.1\,\mathrm{T}$), the transition becomes smooth and there is only little increase of M at low temperature.

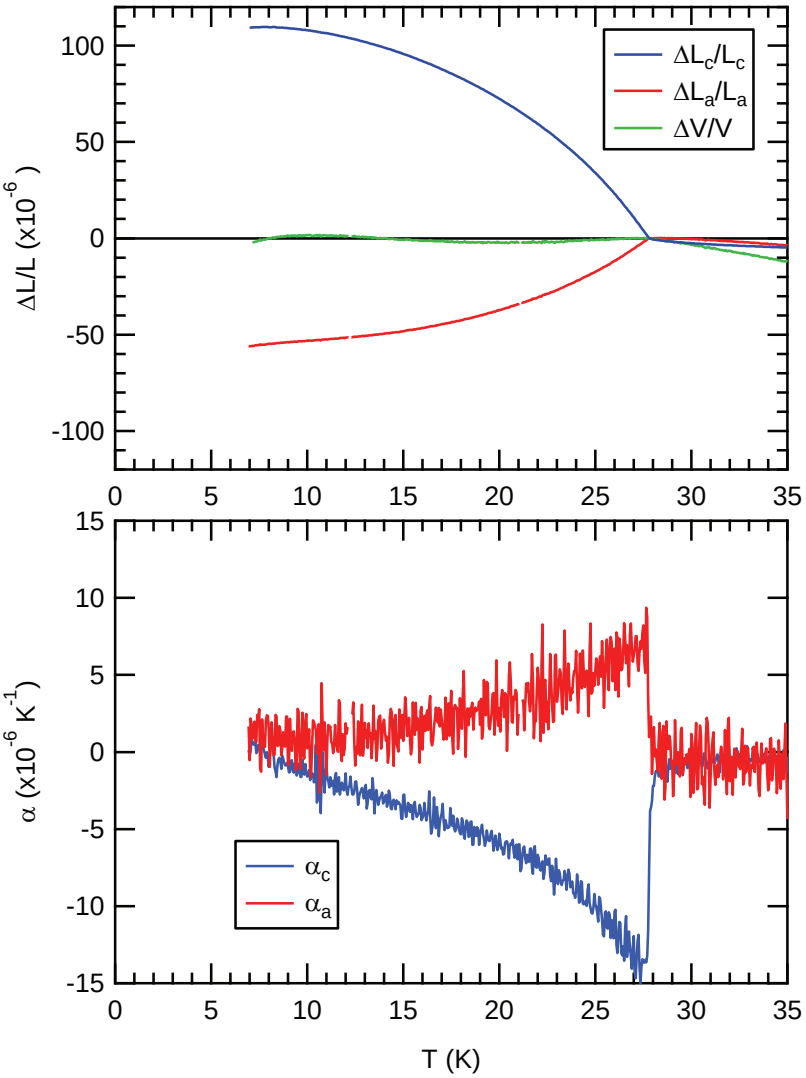

Figure 4.4: a) Thermal expansion of URhAl along c- and a-axes, and volume expansion (green). b) Thermal expansion coefficients along c- and a-axes.

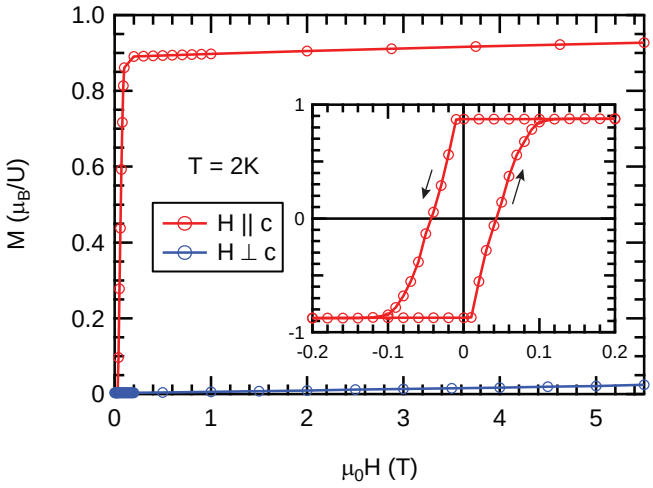

Figure 4.5: Magnetization of URhAl versus magnetic field along c (red symbols) and a-axis (blue symbols), at 2 K. Inset shows the hysteresis loop of the magnetization reversal.

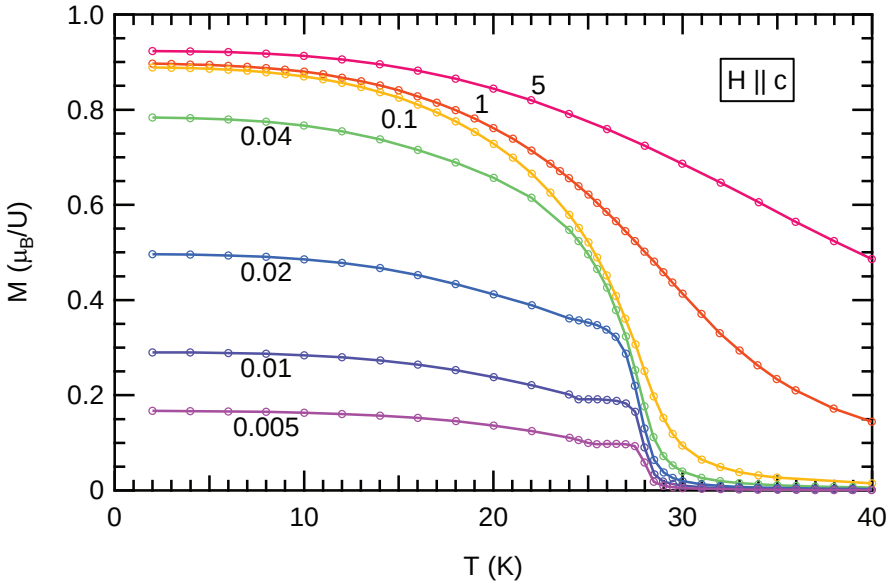

Figure 4.6: Field-cooling magnetization of URhAl versus temperature with field applied along c-axis. Labels indicate field values in Tesla.

4.3.1 Critical behaviour

We performed Arrott–Noakes analysis of the PM-FM transition of URhAl by using field-sweep magnetization measurements around T_C. This analysis is based on the equation of state first proposed in 1956 by K. P. Belov and A. N. Goryaga [64] and soon after by A. Arrott [65]. They started with the Ginzburg–Landau expansion of the free energy:

$$F(M) = -HM + a\,(T - T_C)\,M^2 + bM^4 + ... \tag{4.1}$$

and they derived the equation of state in the vicinity of T_C:

$$M^2 = -\frac{a}{b}\frac{(T - T_C)}{T_C} + \frac{1}{b}\frac{H}{M} \tag{4.2}$$

According to equation 4.2, the so-called *Arrott plot* consists of M–H isotherms around T_C plotted as M^2 vs $\frac{H}{M}$ which should form straight and parallel lines. This technique is used to determine T_C by the isotherm crossing the origin. However, this description fails in the case of weak itinerant ferromagnets such as pure Ni metal. A. Arrott and J. E. Noakes [66] generalized Eq. 4.2 into:

$$\left(\frac{H}{M}\right)^{1/\gamma} = \frac{T - T_C}{T_1} + \left(\frac{M}{M_1}\right)^{1/\beta} \tag{4.3}$$

where M_1 and T_1 are constants dependent on the material, and β,γ are critical exponents. According to equation 4.3, the *modified Arrott plot* now consists of M–H isotherms plotted as $M^{1/\beta}$ vs $\left(\frac{H}{M}\right)^{1/\gamma}$. This technique was applied in Fig. 4.7 to determine the critical exponents β and γ. Straight lines have been obtained with $\beta = 0.5$ and $\gamma = 1.3$.

From equation 4.3, we can derive the saturation magnetization $M_S = \lim_{H\to 0} M(H)$ and the inverse initial susceptibility $\chi_0^{-1} = \lim_{M\to 0} \frac{H}{M}$:

$$M_S(T) = M_0\left(1 - \frac{T}{T_C}\right)^{\beta} \qquad \text{for } T < T_C \tag{4.4a}$$

$$\chi_0^{-1}(T) = \frac{h_0}{M_0}\left(\frac{T}{T_C} - 1\right)^{\gamma} \qquad \text{for } T > T_C \tag{4.4b}$$

In the vicinity of a second-order phase transition, due to the divergence of the correlation length, M_S (eq. 4.4a) and χ_0^{-1} (eq. 4.4b) follow universal scaling laws, and the critical exponents β and γ only depend on the spin and dimensionality of the system (see Table 4.1).

In the modified Arrott plot (Fig. 4.7), the critical exponents under which the M–H curves are straight lines are $\beta = 0.5$ and $\gamma = 1.3$. Then, from the Y and X intercepts of the modified Arrott plot, we can plot the saturation magnetization M_S and the inverse

Table 4.1: Critical exponents predicted by mean field theory (MF) and 3D Ising model [67]

Model	β	γ
MF theory	0.5	1.0
3D Ising	0.325	1.24

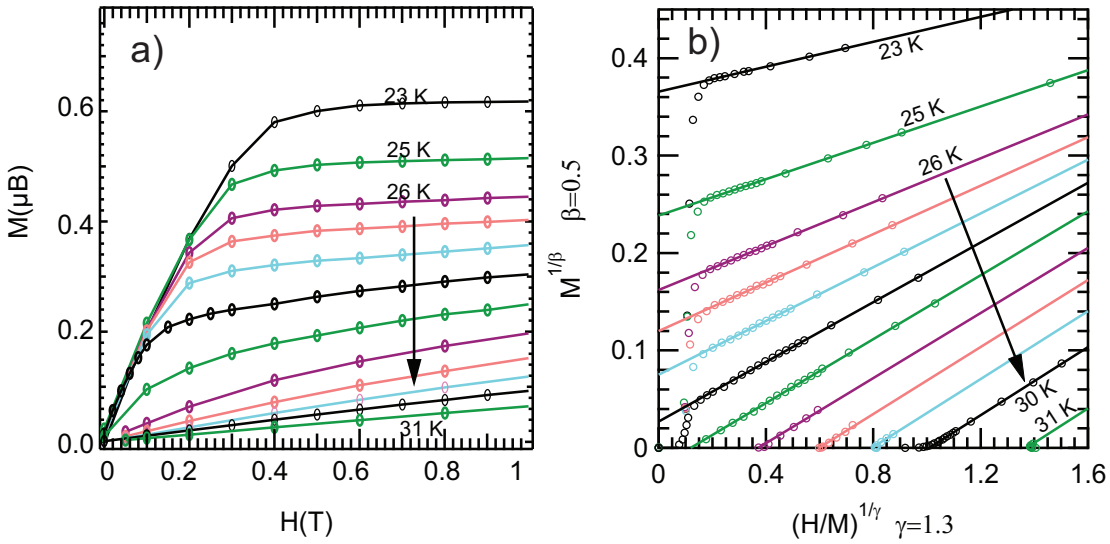

Figure 4.7: a) M-H isotherms of URhAl around T_C; b) modified Arrott plot of URhAl obtained with critical exponents $\beta = 0.5$ and $\gamma = 1.3$. Labels indicate the temperature (every 0.5 K between 26 K and 30 K). Lines show linear fits. T_C is located between 27.5 and 28 K, when $M^{1/\beta} \propto (H/M)^{1/\gamma}$.

initial susceptibility χ_0^{-1} as a function of temperature (Fig. 4.8-a). The Curie temperature can be identified with great precision by extrapolating both M_S and χ_0^{-1} to 0, and we obtain $T_C = 27.9$ K

The temperature dependence of M_S and χ_0^{-1} were fitted by equations 4.4a and 4.4b in a log–log scale (see Fig. 4.8-b and 4.8-c). The fit to universal scaling laws is successful for M_S only in the vicinity of T_C, with $\beta = 0.47$ (in good agreement with the value obtained by the modified Arrott plot), and an extrapolated value of $M_0 = 1.5\,\mu_B$, which is far beyond the spontaneous magnetization at $T \to 0$ ($0.9\,\mu_B$). This is not surprising since the relations 4.4a and 4.4b are valid only in the critical region. For χ_0^{-1}, the fit gives $\gamma = 1.03$, which is quite different from the Arrot plot value (1.30).

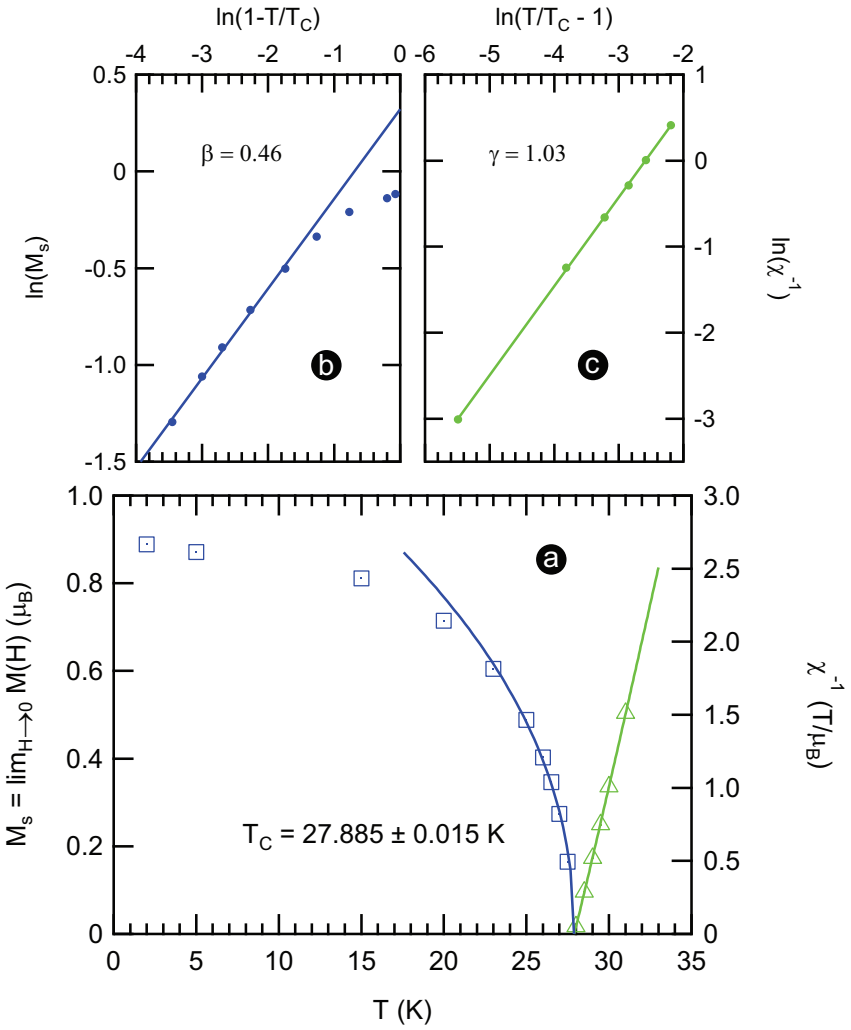

Figure 4.8: a) Temperature variation of $M_S(0,T)$ obtained from Y intercepts and χ_0^{-1}(T) from X intercepts in Figure 4.7, b) $\ln(M_S)$ vs $\ln(1-T/T_C)$ and c) $\ln(\chi_0^{-1})$ vs $\ln(T/T_C-1)$, along with the fits (solid lines) to Eqs. 4.4a and 4.4b, respectively.

4.3.2 Discussion

The Arrott–Noakes equation of state fails to describe correctly our magnetization data in the vicinity of the PM-FM transition of URhAl:

- the modified Arrott plot shows straight lines which are not parallel, indicating that the parameters T_1,M_1 vary accross the transition
- different values of the critical exponent γ are obtained according to the modified Arrott plot (1.3) or the inverse initial susceptibility χ_0^{-1} (1.03)
- the critical exponent β is found to be ≈ 0.5 in the vicinity of T_C, which is that of a mean field system (see Table 4.1), although URhAl is obviously a 3D Ising system.

These observations suggest that the PM–FM transition of URhAl is complicated by the variation of some microscopic parameters, possibly the exchange coupling and/or the quenching of the U orbital moments due to enhanced correlation effects on cooling.

4.4 Probing the magnetic order with neutron scattering

URhAl belongs to the large family of *UTX* compounds cristallizing in the hexagonal ZrNiAl–type structure (space group $p\bar{6}2m$). Since the U atoms form a quasi-Kagome lattice, it is naturally expected to have frustrated magnetic moments. As explained in section 4.1, all UTX compounds with the same crystallographic structure as URhAl have FM planes which are ordered ferro- or antiferromagnetically along c, appart from UNiAl which has a low q in-plane modulation in addition to an AF order along c ($\vec{q} = (0.1, 0.1, 0.5)$). In this context, we decided to perform a neutron diffraction experiment on a single crystal of URhAl, to look for possible in-plane or out-of-plane modulations of the magnetization.

The neutron diffraction experiment was performed with E. Ressouche at ILL, Grenoble, with the 2-axis diffractometer D23. The sample was a $12\,\mathrm{mm}^3$ single-crystal with roughly cylindrical shape. The structure was refined at 35 K and 2 K using 728 and 594 non-equivalent reflections, respectively. Several q-scans were performed above and below T_C (at 35 K and 2 K), so that the reciprocal space was scanned along a dozen of directions (in-plane and out-of-plane), which are listed in Table 4.2. As an example, Figure 4.9 shows the scans (q_h,0,0), $0.3 < q_h < 3.3$, in the PM and FM phases, along with the substrated spectrum. There is only minor shouldering of the peaks, thus indicating the quasi perfect single crystal sample. Diffraction peaks only appear at integer values of q_h, corresponding to lattice reflections. The small temperature-independent peaks around $q_h = 2.3$ and 2.8 are ascribed to the copper sample holder. For all q-scans, the systematic substraction of the PM scans from the FM scans yielded no additional reflections.

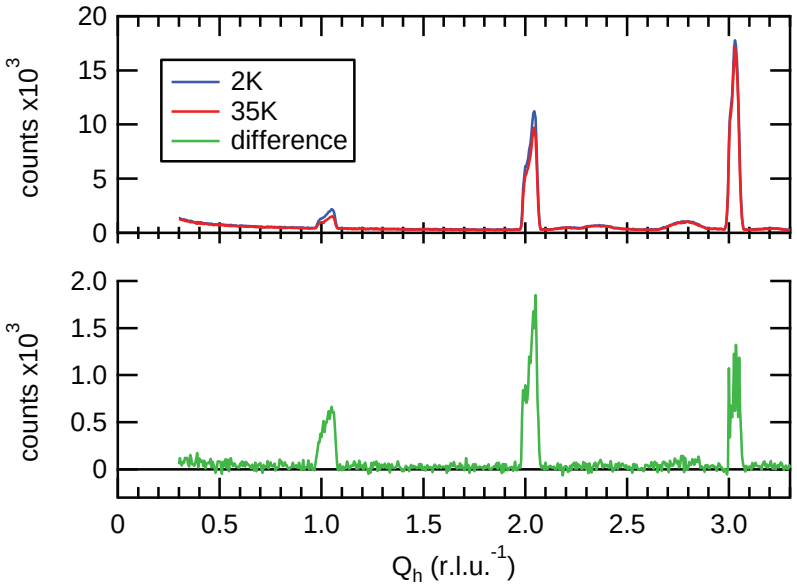

Figure 4.9: q-scans of neutron scattering on URhAl along the (q_h,0,0)-direction below (2 K, blue curve) and above (35 K, red curve) the Curie temperature. The difference (green curve) between the two scans is plotted on an expanded scale. q_h is expressed in inverse relative lattice units.

As a conclusion, we performed various q-scans spanning the main reciprocal space directions, and found no superlattice reflections. We thus confirm that URhAl has a pure FM ground state.

4.5 AC calorimetry under pressure

AC calorimetry measurements have been carried out under pressure, using a Diamond Anvil Cell (DAC), in order to obtain the temperature–pressure phase diagram of URhAl.

4.5.1 Experimental setup

The measurements were carried out using a system that allows to vary the pressure *in-situ*. The details of the apparatus, of the DAC, and the principle of AC calorimetry are presented in Chapter 2.

The sample size was 150 µm diameter by 60 µm thick, and the pressure chamber initial dimensions were 350 µm diameter and 150 µm thick. The thermocouple Au-AuFe(0.07%) was spot-welded onto the sample, using 17 µm-thick Au wire and AuFe foil. The pressure cell was closed with liquid argon as a pressure transmitting medium, setting an initial

scan	q_h		q_k		q_l	
	min	max	min	max	min	max
a	0.3	3.3	0	0	0	0
b	0.2	3.2	0.2	3.2	0	0
c	0	3.1	0	0	-0.25	-0.25
d	0	3.1	0.1	3.1	-0.25	-0.25
e	0	3.1	0	0	-0.333	-0.333
f	0	3.1	0.1	3.1	-0.333	-0.333
g	0	3.1	0	0	-0.5	-0.5
h	0	3.1	0.1	3.1	-0.5	-0.5
i	0	0	0	0	-0.2	-3.2
j	1	1	0	0	0	-3.2
k	1	1	1	1	0	-3.2

Table 4.2: List of q-scans performed at ILL-D23 on URhAl at 35 K and 2 K, in search for non-FM magnetic structure. Values of $q_{h,k,l}$ are expressed in inverse relative lattice units (r.l.u.$^{-1}$).

pressure of 3 kbar at 300 K. Once cooled to liquid Helium temperature, the residual pressure was 0 kbar.

The experiment was performed by increasing pressure step by step, from 0 to 4.8 GPa in a first run, and from 0 to 5.8 GPa in a second run. Between the two runs, the force has been released and the experimental setup has been warmed up to room temperature, but the pressure cell kept the pressure transmitting medium (Ar) inside. These two runs assessed the reproducibility of our measurements.

The AC calorimetry data was obtained by performing temperature scans, starting from the base temperature of the ^{4}He bath (4.2 K) and increasing the current through a heater attached to the body of the pressure cell. Sometimes the base temperature was decreased by pumping on the bath to start the scan from 2 K.

The same working frequency of 1710 Hz was kept during the entire experiment. The data were smoothed by averaging within 0.1 K windows. The amplitude of the signal is usually presented as $\frac{S_{th}}{RT}$, which we will now refer to as «C/T», keeping in mind that this is only approximatively proportional to the total heat capacity (sample + addenda). The C/T vs T curves were scaled manually to match one another at high temperature. Such corrections ($\pm 10\,\%$) compensate the variations of the heating power between two scans.

4.5.2 Results

AC-calorimetry results for URhAl are presented in Figure 4.10. Figure 4.10-a shows $\frac{S_{th}}{RT} \propto \frac{C}{T}$ vs T, and Figure 4.10-b offers an expanded view of the former plot by substracting

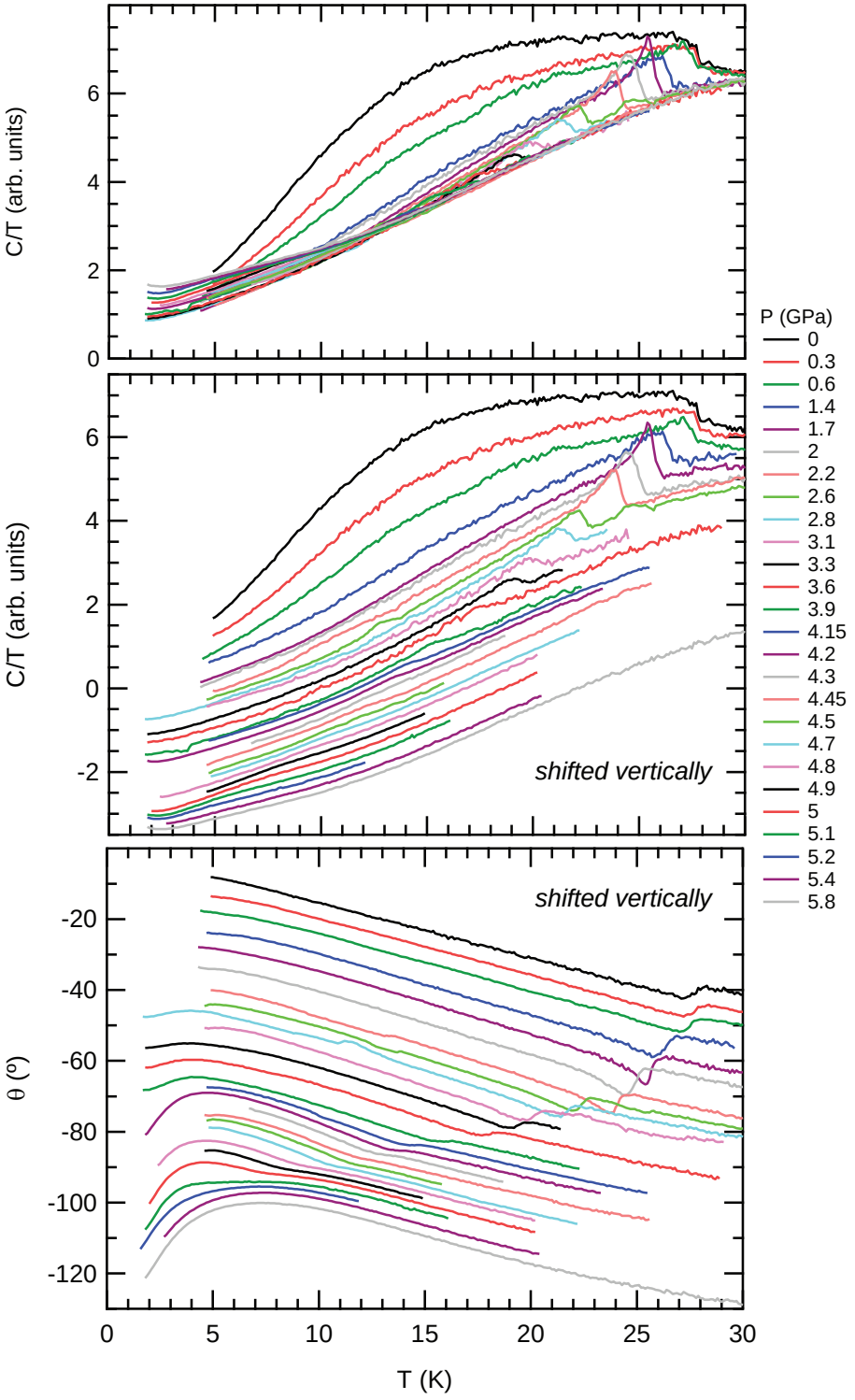

Figure 4.10: Results of AC calorimetry of URhAl under pressure: temperature dependence of a) $\frac{C}{T}$, b) $\frac{C}{T} - \frac{C}{T}_{5.8\,\mathrm{GPa}}$ and c) phase shift θ. Legend indicates the pressure values. Curves in (a) and (b) are shifted vertically for clarity.

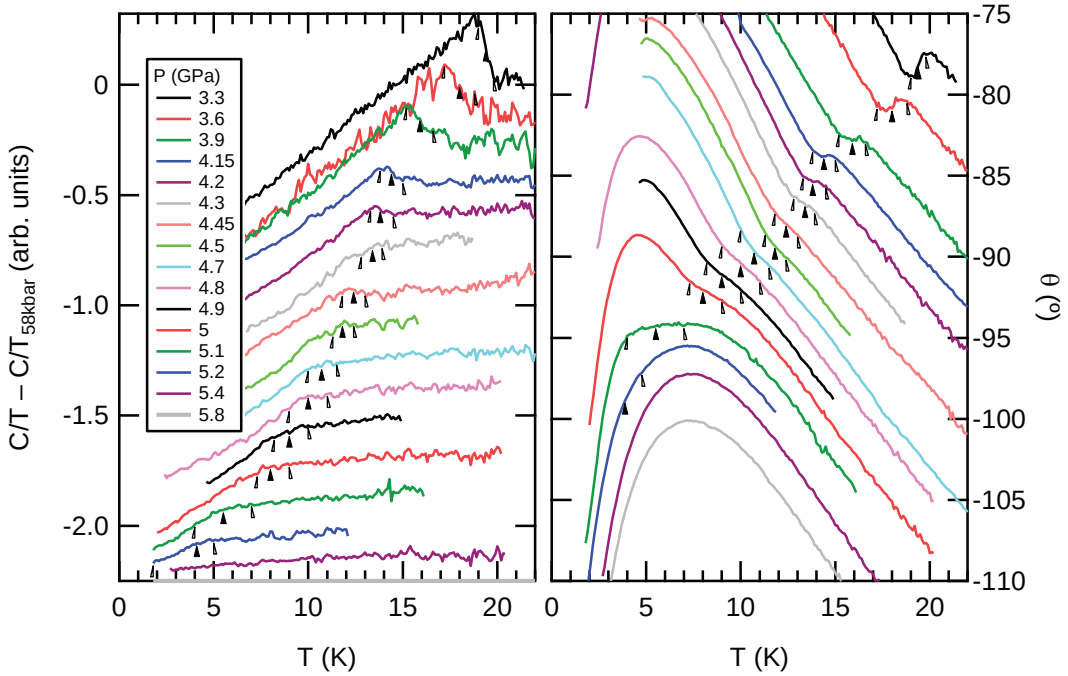

Figure 4.11: Focus on the high pressure curves of Figs. 4.10-b (left) and 4.10-c (right). Full arrows indicate T_C, and empty arrows indicate the lower and upper limits of the transition. These arrows are located at the same coordinates in both graphs. Curves are shifted vertically for clarity.

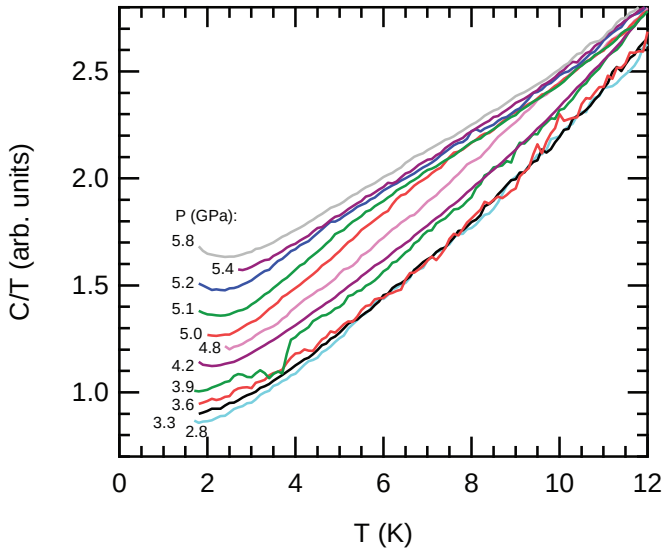

Figure 4.12: Focus on the low temperature part of selected curves from Fig. 4.10-a.

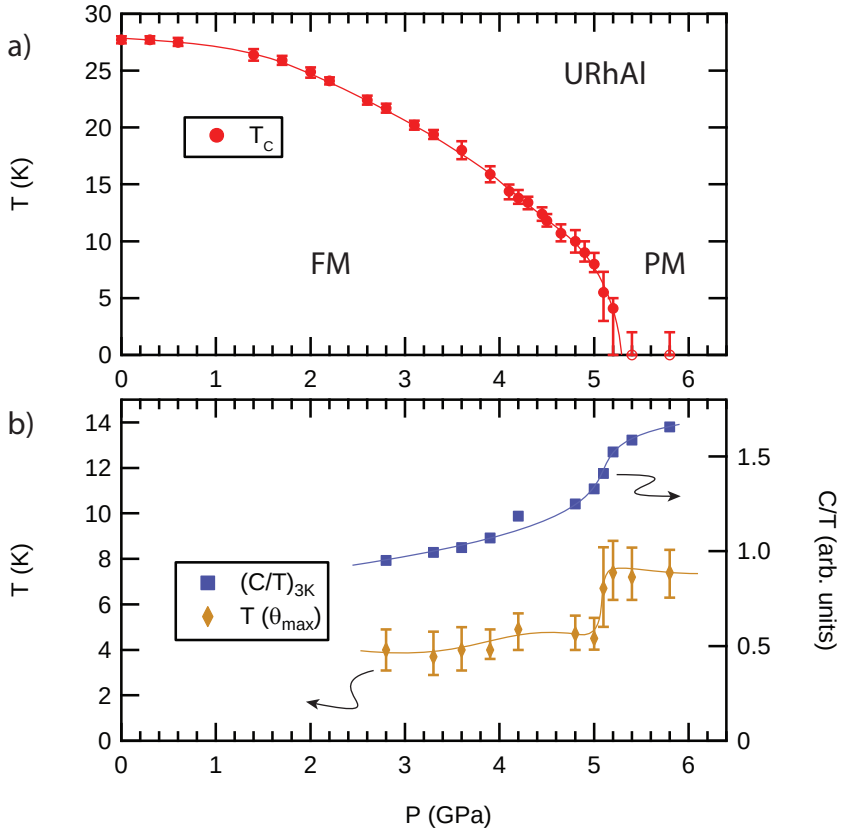

Figure 4.13: a) Temperature–Pressure phase diagram of URhAl obtained from AC calorimetry measurements. The values of T_C and error bars are set according to Fig. 4.11; b) pressure evolution of $T_\theta^{\max}$ (left axis) and $\frac{C}{T}_{3\,\mathrm{K}}$ (right axis).

$\frac{C}{T}_{5.8\,\mathrm{GPa}}$ to all curves. The phase θ is plotted in Figure 4.10-c.

At $P = 0$, a clear anomaly signals the PM-FM transition at $T_C = 27\,\mathrm{K}$, in both C/T and θ vs T curves. The initial pressure dependence of T_C is completely flat up to 0.6 GPa, in agreement with the negligible volume expansion measured previously (section 4.2.3). Then T_C decreases gradually with pressure. At $P = 0$, the transition appears as a downward step in C/T vs T, and an upward step in θ vs T. There is a broad hump in C/T vs T centered around 15 K, which is not present in the absolute specific heat measured outside the pressure cell by relaxation method (see Fig. 4.3). This shows that the hump is an artifact. As pressure increases ($0 < P < 1.7\,\mathrm{GPa}$), this hump in C/T disappears progressively, and a peak starts to develop just before the step (visible in both C/T and θ). At 1.7 GPa, the peak is sharpest (more spectacular in C/T), and then gradually decreases with pressure. The broad hump vanishes completely around 2.5 GPa.

The high pressure curves are better seen in Fig. 4.11, which offers a closer view to $\frac{C}{T} - \frac{C}{T}_{5.8\,\mathrm{GPa}}$ and θ vs T. On every curve, the transition region is delimited by two cursors, and an arrow indicate the probable transition point. Around 4.3 GPa, the sharp step in θ turns into a broad shoulder-like anomaly, and the peak structure in C/T smears out.

Further increasing pressure, an anomaly associated to the transition continues to appear. It consists of a change of the slope in $\frac{C}{T} - \frac{C}{T}_{5.8\,\mathrm{GPa}}$ (visible up to 5.2 GPa). In parallel, the transition appears at the same temperature values in θ vs T as a shoulder-like anomaly, clearly visible up to 5.1 GPa. The transition temperature is plotted versus pressure in Figure 4.13-a, drawing the phase diagram of URhAl. Above 5.2 GPa, no transition can be detected, at least down to 2 K.

Low temperature behaviour

On cooling below 4.2 K, θ shows a downturn below $T_\theta^{\max} \approx 4\,\mathrm{K}$. This is considered to be an artifact caused by the rapid decrease of the thermocouple response at low temperature. The shoulder-like anomaly merges with the downturn of θ, in such a way that the maximum of θ becomes a broad plateau [4 – 7 K] at 5.1 GPa. Above this pressure, no signature of a transition can be seen in θ, but the maximum is shifted to $T_\theta^{\max} \approx 7\,\mathrm{K}$.

Figure 4.12 shows C/T vs T in the region of pressure and temperature where T_C collapses. We observe an increase of C/T with pressure. The pressure evolution of C/T taken at 3 K and of $T_\theta^{\max}$ is plotted in Fig. 4.13-b. The error bars on $T_\theta^{\max}$ reflect the broadness of the maximum : they delimit the temperature interval within which $\theta > \theta^{\max} - 0.4\,°$. There is a pronounced increase of both $\frac{C}{T}_{3\,\mathrm{K}}$ and $T_\theta^{\max}$ between 5.0 and 5.2 GPa, which corresponds to the collapse of T_C.

4.5.3 Discussion

At low pressure, the broad hump in C/T vs T around 10 – 20 K) indicates that the data below 2.5 GPa have a problem, since there is no such anomaly in the specific heat measured at ambient pressure with the relaxation method (Fig. 4.3). Therefore, we consider the sharp peak in C/T at 1.7 GPa to be an artifact. Above $\sim$ 2.5 GPa, the C/T vs T curves recover a normal shape.

An anomaly associated to the Curie temperature can be tracked under pressure up to 5.1 GPa in both C/T and in the phase θ. There is an ambiguity at 5.2 GPa (anomaly in C/T only), and no anomaly above. This allows to draw the T–P phase diagram of URhAl (Fig. 4.13-a). By extrapolating to 0 K where T_C collapses, a quantum phase transition is expected at $P_C = 5.3 \pm 0.1$ GPa.

We may infer that the ground state of URhAl just above P_C is similar to the case of UCoAl at zero pressure. According to the reported lattice parameters measurements under pressure [52], in URhAl the lattice parameter $a = 696.5$ pm at ambient pressure reduces to $\approx$ 688 pm at P_C, which is 1/3 the way to UCoAl ($a = 668.5$ pm), while $c = 402$ pm remains unchanged (in UCoAl: $c = 396.5$ pm). These lattice considerations are consistent with the picture that the closer in-plane packing increases the $5f$-ligand hybridization and wipes out the magnetic moments.

Around P_C, there is an increase of C/T at low temperature (see Fig. 4.12 and 4.13-b), and also a shift of $T_\theta^{\max}$, which are both too sharp to be merely ascribed to a change in the sample environment. Therefore, it is probably due to an increase of the sample heat capacity. This suggests an increase of the Sommerfeld coefficient γ, as it is normally expected in the vicinity of a quantum phase transition.

A tricritical point (TCP) is expected close to P_C, where $\partial T_C/\partial P$ starts to diverge, as for example in the case of UGe_2: $P_C - P_{\mathrm{TCP}} = 0.8$ GPa. But in the case of UCoGe, the FM-PM transition seems already weakly first order at ambient pressure, as suggested by a discontinuous splitting of the ^{59}Co NMR spectrum at T_C [68]. A way to identify the TCP would be the observation of metamagnetic «wings» upon application of a magnetic field. Next target will be to probe the possible «wings» and to study the properties of URhAl below 1 K around P_C using a resistivity setup in a dilution refrigerator.

4.6 Conclusion

We obtained high quality single crystals of URhAl, which have been characterized by resistivity, heat capacity, thermal expansion, and magnetization measurements. The FM order occurs below $\sim$ 28 K, to an Ising-type ordered state with 0.9 μ_B along the c axis. The Sommerfeld coefficient $\gamma = 76\,\mathrm{mJ.mol^{-1}.K^{-2}}$ is slightly larger than the reported value ($67\,\mathrm{mJ.mol^{-1}.K^{-2}}$ [62]). The resistivity shows a T^2 dependence up to $\sim$ 6 K, and is largely dominated by magnon scattering contribution.

We performed magnetization measurements along the c-axis around the Curie temperature. The modified Arrott plot analysis fails to describe the critical behaviour correctly, probably because T_C is comparable to the onset of the Kondo lattice so the size of the magnetic moment and the degree of delocalization are dynamically changing with temperature.

We checked the magnetic order with neutron diffraction along various reciprocal space directions. No superlattice reflections have been observed at 2 K, thus confirming the simple FM order in URhAl.

Finally, we established the phase diagram of URhAl under pressure by means of AC calorimetry measurements. The Curie temperature decreases and reaches 0 K around 5.3 GPa. At the critical pressure, we observed an increase of C/T which may be related to an effective mass enhancement associated with the quantum phase transition.

Chapter 5

UCoAl

UCoAl belongs to the UTX family of compounds with hexagonal ZrNiAl-type structure, as URhAl (which is presented in Chapter 4). Its ground state is paramagnetic (PM), but it has the very peculiar feature that a ferromagnetic (FM) state is induced when magnetic field is applied along the c-axis. This is a first-order PM-FM transition called *metamagnetic* transition.

In this chapter, we first review the characteristics of UCoAl and replace it in the general context of FM quantum criticality. Then we present our studies on this compound: pressure studies of Hall effect and resistivity, magnetization, and X-ray magnetic circular dichroism (XMCD).

5.1 Introduction

5.1.1 Motivation

Ferromagnetic quantum criticality

The metamagnetism in strongly correlated electron systems with Ising–type ferromagnetic (FM) behaviour is intensively studied because it produces a variety of unconventional effects. In some itinerant ferromagnets, such as UGe_2 [17, 18] or $ZrZn_2$ [9], one can drive the Curie temperature T_C to 0 K by tuning an external control parameter like pressure, and the ground state is found to be paramagnetic (PM) above the quantum phase transition. In theory, it has been suggested — and in some cases experimentally shown — that the second order ferromagnetic transition changes to first order at a tricritical point [69]. By applying a magnetic field above the critical point in the paramagnetic phase, such systems eventually recover their ferromagnetic state by undergoing a first–order metamagnetic transition at H_m, drawing a wing–shape first order transition plane in the temperature (T) – pressure (P) – field (H) phase diagram. The first-order transition terminates at high pressure and high field at $T = 0$ at the so–called quantum

critical endpoint (QCEP). In this critical region, only few experiments were carried out because of the severe experimental conditions of low temperature, high pressure, and high field [9, 17, 18, 70].

Due to the recent focus on quantum criticality, the metamagnetism in itinerant ferromagnets has been revisited theoretically (see e.g. Ref. 71, 72). The main debate is whether a Lifshitz–like transition is associated with the occurrence of metamagnetism, as discussed in the case of $CeRu_2Si_2$ [73].

UCoAl : a good candidate for FM criticality studies

A good candidate to investigate itinerant metamagnetism is the heavy fermion compound UCoAl, with ZrNiAl–type hexagonal structure, space group $P\bar{6}2m$. At ambient pressure, its ground state is paramagnetic, with strong uniaxial magnetic anisotropy. By applying magnetic field along the easy magnetization axis (c–axis), a sharp first–order metamagnetic transition occurs at low temperature at a critical field $H_m \sim 0.7\,\mathrm{T}$ [74, 75]. The first–order nature of the metamagnetic transition terminates at a critical end point (CEP) at $T_0 \sim 12\,\mathrm{K}$, and changes into a crossover at higher temperature [76–78].

By applying pressure, resistivity and magnetostriction experiments [76, 79] have shown that the critical field increases up to the QCEP, located at $P_{QCEP} \sim 1.6\,\mathrm{GPa}$ and $H_{QCEP} \sim 7\,\mathrm{T}$, where an acute enhancement of the effective mass $m^\star$ of the quasiparticles has been detected. Previous magnetization experiments under pressure are in good agreement with an initial pressure increase of H_m [75]. It is worthwhile to remark that just above P_{QCEP} in the paramagnetic ground state in high magnetic field, sharp pseudometamagnetism at H_m will replace the sharp first order metamagnetism below P_{QCEP} [71]. Further increasing pressure must lead to a broadening of the pseudometamagnetic transition.

5.1.2 State of the art on UCoAl

Magnetic anisotropy

The metamagnetic behaviour of UCoAl was first reported by Andreev *et al.* in 1985 [74].

It is a highly anisotropic system, with Ising-like behaviour: At low temperature, along the c-axis, there is a high initial susceptibility. A first-order transition occurs at $0.7\,\mathrm{T}$ to the FM state with $0.3\,\mu_\mathrm{B}$, and the magnetization keeps on increasing in the ordered state, with no sign of saturation up to the highest fields ($0.6\,\mu_\mathrm{B}$ at $40\,\mathrm{T}$). On the contrary, perpendicular to c, there is a low paramagnetic response, with only $0.1\,\mu_\mathrm{B}$ at $40\,\mathrm{T}$. The magnetic anisotropy is already visible at high temperature ($\sim 300\,\mathrm{K}$) with a much stronger magnetic susceptibility along the c-axis. The temperature dependence of the susceptibility exhibits a Curie-Weiss law above $40\,\mathrm{K}$ with $\mu^{\mathrm{eff}} \approx 1.8\,\mu_\mathrm{B}$ — much larger than the ordered moment of $0.3\,\mu_\mathrm{B}$ in the FM state. This indicates the itinerant

nature of magnetism in UCoAl.

$T_\chi^{\max}$

The susceptibility along c shows a broad maximum at $\sim 20\,\mathrm{K}$ [76, 80]. This $\chi^{\max}$ was observed in other itinerant metamagnets : the Co-based pseudo binaries $Co(S_{1-x}Se_x)_2$, YCo_2, $LuCo_2$, etc. [10], which are isotropic systems. The singularity of UCoAl, beside the Ising-like anisotropy, is the much lower energy scale ($T_\chi^{\max}$, T_{CEP},H_m), of one or two orders of magnitude compared to the former materials.

Microscopic point of view

Polarized neutron diffraction experiments [81, 82] mapped the magnetization density and found that the magnetic moment is exclusively present on the U sites, and that the orbital moment is twice as large and antiparallel to the spin moment. This has been also inferred from band structure calculations and X-ray Magnetic Circular Dichroism experiments [59, 60].

A recent ^{59}Co NMR study [22] has confirmed that the magnetic moment on the Cobalt must be very low ($\mu_{\mathrm{Co}}/\mu_{\mathrm{U}} <\sim 0.01$). They found a linearly M-dependent, positive Knight shift on the Co(1) site (on the same hexagonal plane as U). Because of the strong Co hyperfine coupling constant ($A_{\mathrm{Co}} \approx -10\,\mu_{\mathrm{B}}/\mathrm{T}$), any sizable moment on the Co would have given a contribution to the Knight shift, which would have been non-M-linear since U-5f – Co-d hybridization must be different in the PM and FM states due to lattice change.

UCoAl in the framework of UTX compounds

Systematic studies of UTX compounds have established that UCoAl is a borderline system between non-magnetic and magnetically ordered materials. As a rule, the 5f-ligand hybridization is regarded as the tuning parameter in this family of compounds. Several studies against doping $UCo_{1-x}T_xAl$ showed a high sensitivity of the metamagnetism to small substitutions. But the effect of doping in UCoAl can be quite misleading and counter-intuitive. A typical example is the antagonist effect of Fe/Ni substitution for Co, which are the left- and right- hand side direct neighbours of Co in the periodic table: Fe doping (d-electron depletion) stabilizes a FM ground state with as little as 2% Fe substitution, while Ni doping (d-electron filling) causes the metamagnetic field to increase [83]. As it happens, this is exactly the opposite of what we would naively expect, that the increasing d-filling normally leads to magnetic states (UFeAl is non-magnetic while UNiAl is antiferromagnetic). In UCoAl, the ground state is also affected by the lattice strain induced by substitutions, and thus there is no simple rule.

Magnetoelastic properties

There is a large magnetostriction effect of the order of 10^{-4}, which is negative along the c-axis and positive in the perpendicular direction [74], and the total volume expansion is positive. The corollary of this large magnetostriction is the high sensitivity to external pressure: a uniaxial stress of $\sim$ 0.3 kbar along c tunes the system to a FM ground state with $T_C \sim 15$ K [84], while hydrostatic pressure increases H_m and decreases the magnetization in the polarized state [75, 85].

Non-Fermi liquid behaviour

At rest, UCoAl is close to a FM instability, and the PM ground state is characterized by strong spin fluctuations and non-Fermi liquid behaviour. Electrical resistivity exhibits $T^{5/3}$ or $T^{3/2}$ dependence in the PM state, as predicted by the renormalization group theory for 3D Ising FM ($T^{5/3}$) or AF ($T^{3/2}$) spin fluctuations [45]. UCoAl recovers a usual Fermi liquid T^2 dependence in the FM state [86, 87]. The NFL behaviour in the PM state was also attested with thermoelectric measurements by a diverging S/T at the lowest temperature [78]. ^{59}Co and ^{27}Al NMR studies have further confirmed the 3D spin fluctuations, with longitudinal propagation direction. Furthermore, these NMR studies have evidenced the enhancement of spin fluctuations in the vicinity of the CEP, with critical exponents corresponding to the 3D Ising class of criticality (isomorphic to the gas-liquid transition of water) [22, 77].

The extension of the NFL behaviour under pressure is unclear.

In 2002, Honda *et al.* [79] performed the first pressure study of resistivity on UCoAl down to ≈ 4 K, and they concluded to the suppression of NFL behaviour under pressure. This points out to spin fluctuations being responsible for the NFL state in the proximity of the FM instability.

But in 2006, Havela *et al.* [88] measured the resistivity in the range [1-18 K] and concluded to a very extended NFL region up to $\sim$ 5 GPa. This is similar to the case of the helimagnet MnSi above the critical pressure, where NFL behaviour ($\rho \sim T^{3/2}$) is observed in a very extended pressure range [89]. Such a robust NFL state in UCoAl may be related to frustrated AF correlations between the U atoms arranged on a quasi-kagome lattice.

5.2 Hall effect

The content of this section has been published in September 2013, in the Journal of the Physical Society of Japan [90]. In this section, we sometimes have to distinguish between the applied magnetic field H and the magnetic induction B. For convenience, we decided to generically use the notation B throughout the entire section on Hall effect, except when it is explicitly stated otherwise.

An interesting tool to unveil the physical properties in the vicinity of a QCEP is the Hall effect as it has two main contributions: the normal Hall effect (NHE), which is linked to the type of carriers and their number, and the anomalous Hall effect (AHE), which is linked to the magnetization M. Changes in the effective mass (m^*) associated (or not) to a Fermi surface instability at the QCEP may have a specific signature.

In this section we present detailed Hall effect measurements performed on a single crystal of UCoAl, at low temperatures down to 150 mK, under hydrostatic pressure up to 2.2 GPa and magnetic field up to 16 T.

5.2.1 Experimental

Single crystals of UCoAl were prepared from depleted U (99.9% – 3N), Co (3N) and Al (5N) in stoichiometric proportions. The components were melt in a tetra–arc furnace under Ar gas atmosphere and a single crystal ingot was pulled by Czochralski method with pulling rate of 15 mm/h. The single crystal was checked by X–ray Laue photograph. A flat c–plane rectangular sample of $1.8 \times 1.2 \times 0.2\,\mathrm{mm}^3$ was cut with a spark–cutter for the Hall effect measurements. Its residual resistivity ratio $RRR = 14$ is within the highest reported for UCoAl indicating the very good quality of the crystal.

Magnetization measurements at ambient pressure were performed on another sample from the same ingot, with a commercial SQUID magnetometer (Quantum Design) down to 1.8 K and up to 5.5 T. The metamagnetic critical field $B_m = 0.6$ T of that crystal is slightly lower than that of the crystal used for the Hall effect experiment where we found $B_m = 0.7$ T. This shows the high sensitivity of B_m to the quality and/or homogeneity of the single crystals.

The Hall effect ρ_{xy} was measured using a four–probe AC lock–in technique. The current was applied perpendicular to the c–axis in the hexagonal planes (typically 1 mA at a frequency $f \sim 17$ Hz) and positive and negative fields were applied along the c–axis, which is the easy magnetization axis, in order to cancel out contributions of the magnetoresistance R_{xx} due to a small misalignement of the transverse voltage contacts. The symmetric magnetoresistance R_{xx} has been analysed too and good agreement with previous resistivity measurements [76] has been observed. The sample was set in a hybrid CuBe – NiCrAl piston cylinder cell for the pressure studies with Daphne oil 7373 as pressure transmitting medium. The pressure was determined from the superconducting transition temperature of Pb by AC susceptibility measurements. The Hall effect measurements were performed both in a PPMS (Quantum Design) (2 to 300 K ; 0 to 9 T) and in a homemade dilution refrigerator (0.15 to 10 K ; 0 to 16 T).

5.2.2 Hall effect at ambient Pressure

Figure 5.1(a) shows the field dependence of the magnetization at ambient pressure for $B \parallel c$ and $B \perp c$–axis at various temperatures. At low temperatures ($T = 2$ K) a sharp

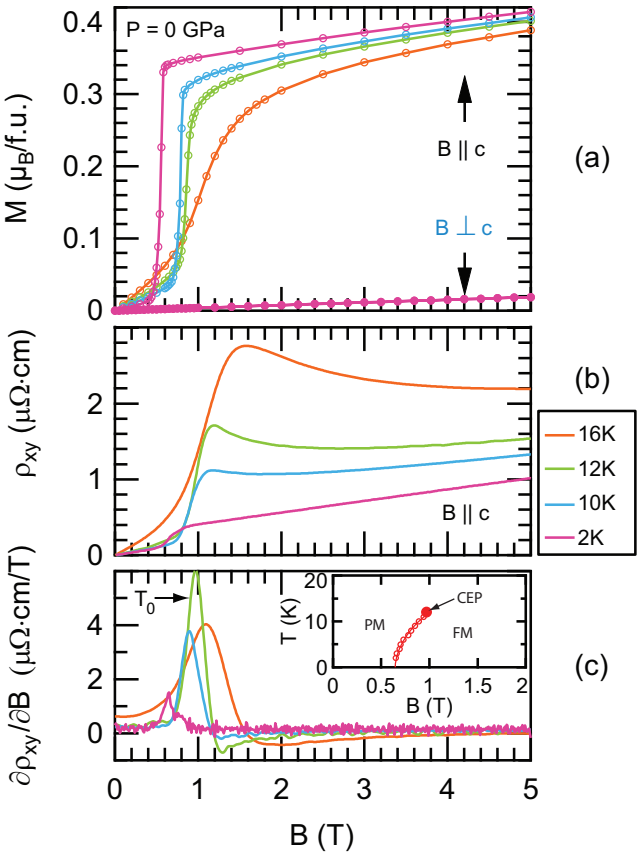

Figure 5.1: (a) Magnetization ($B \parallel$ and $\perp$ c–axis), (b) Hall effect ρ_{xy} ($B \parallel c$), and (c) $\partial\rho_{xy}/\partial B$ vs B at ambient pressure at various temperatures $(2, 10, 12, 16\,\mathrm{K})$. The temperature of the critical end point of the first order transition $T_0 = 12\,\mathrm{K}$ is taken as the maximum of the derivative in (c). The inset in (c) shows the (T, B) phase diagram at ambient pressure from the Hall effect.

metamagnetic transition is observed for $B \parallel c$ at $B_m \approx 0.7\,\mathrm{T}$ from a paramagnetic ground state to a polarized ferromagnetic state with an ordered moment $M_0 \approx 0.3\,\mu_\mathrm{B}/\mathrm{U}$. The magnetization for $B \perp c$ increases linearly and $M \approx 0.023\,\mu_\mathrm{B}/\mathrm{U}$ is found for $B = 5\,\mathrm{T}$, indicating the strong Ising–type anisotropy.

The metamagnetic transition at B_m is of first order, attested by a hysteresis between increasing and decreasing field magnetization curves [74, 76]. The hysteresis reduces and the metamagnetic transition gradually broadens as temperature increases, until it ends at $T_0 = 12\,\mathrm{K}$, marking the first–order critical end point (CEP). For $T > T_0$ a pseudo–metamagnetic transition fades out into a broad crossover region [78].

The Hall resistivity $\rho_{xy}(B)$, see Fig. 5.1(b), is positive through the entire magnetic field range along the c axis. In difference, a negative Hall resistivity has been reported for $B \perp c$ [91] indicating the multi–band character. At the lowest temperatures, the metamagnetic transition appears as a step–like increase in $\rho_{xy}(B)$. This feature is a clear illustration of the interplay between ρ_{xy} and the magnetization. With increasing temperatures ($4\,\mathrm{K} < T < T_0 \sim 12\,\mathrm{K}$), a peak develops just above the critical field B_m. Further increasing temperature, the step–like increase at B_m fades out and only a broad maximum is observed in $\rho_{xy}(B)$ above T_0. Similar features were also found in transverse magnetoresistance $\rho_{xx}(B)$ [76]. This peak in ρ_{xx} was interpreted as an enhancement of the magnetic scattering contribution due to strong magnetic fluctuations around the CEP [22, 77].

From the field derivative of ρ_{xy}, the differential Hall constant $\tilde{R}_H = \partial\rho_{xy}(B)/\partial B$, see Fig. 5.1(c), we locate the critical field B_m at the peak in $\partial\rho_{xy}(B)/\partial B$. The height of the peak is maximal at $T_0 = 12\,\mathrm{K}$, while the width does not broaden with increasing temperature until T_0. Above T_0, the peak height decreases and the width is strongly increasing. We will use the same criterion to determine the first–order critical end point at $(B^\star_m, T_0)$ under pressure. Let us note that the differential Hall coefficient $\tilde{R}_H$ shows little change across B_m (15% decrease), going from $0.18\,\mu\Omega\cdot\mathrm{cm/T}$ in the PM region to $0.15\,\mu\Omega\cdot\mathrm{cm/T}$ in the FM region. By plotting $\partial\rho_{xy}(H,T)/\partial B$ we can draw the (T,H) phase diagram of UCoAl at ambient pressure (see inset in Fig. 5.1(c)) in excellent agreement with previous work [76]. The crossover region extends at least up to 20 K in the continuity of the metamagnetic transition.

Figure 5.2 shows the temperature dependence of the linear Hall coefficient $R_H = \rho_{xy}/B$ at low field ($B = 0.2\,\mathrm{T}$). As we can see, R_H has a maximum around 30 K, connected with a maximum of the magnetic susceptibility χ at $T = 20\,\mathrm{K}$. The inset of Fig. 5.2 shows R_H plotted against χ with the temperature as an incipient parameter. R_H is proportional to the magnetic susceptibility χ from 300 K down to 70 K. In general, the Hall effect can be expressed as the sum of NHE proportional to the carrier contribution and an anomalous contribution from left–right asymmetric scattering due to the ordered magnetic moments (AHE):

$$\rho_{xy}(B) = R_0 B + R_S M \tag{5.1}$$

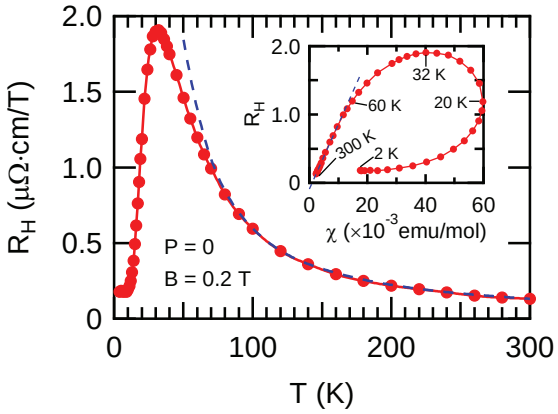

Figure 5.2: Temperature dependence of the Hall coefficient R_H for $B = 0.2\,\mathrm{T} \parallel c$–axis (full circles). The dotted line is a high temperature fit using magnetic susceptibility data (dotted line). The inset shows R_H plotted against the magnetic susceptibility. The linear dependence indicates that the high temperature regime is dominated by the AHE. We obtain $R_0 = -0.1\,\mu\Omega \cdot \mathrm{cm/T}$ and $R_S = 97\,\mu\Omega \cdot \mathrm{cm/T}$.

where the second term $R_S M$ accounts for the AHE and the $R_S \propto \rho_{xx}$ or ρ_{xx}^2 for dominant skew scattering or side–jump scattering processes, respectively.

The proportionality $R_H - R_0 \propto \chi$ is expected in the incoherent high temperature regime with strongly anisotropic crystal field [92]. However, we have to mention that the data can be described similarly by $R_H = R_0 + C\rho\chi$, where R_0 is the normal Hall effect and C a constant [93], as ρ is weakly T–dependent in this temperature range. Thus, regardless of the underlying model, the Hall effect is dominated by the AHE in a large temperature range ($70\,\mathrm{K} - 300\,\mathrm{K}$). R_H is field independent (and so are R_0 and R_S), so it can be fitted using magnetic susceptibility data to obtain $R_0 = -0.1\,\mu\Omega \cdot \mathrm{cm/T}$ and $R_S = 97\,\mu\Omega \cdot \mathrm{cm/T}$ for the high temperature regime as shown in the inset in Fig. 5.2.

The normal contribution to the Hall effect emerges only at low temperature. Figure 5.3 gives an insight to the relation between Hall effect and magnetization at 2 K, to separately account for the NHE and AHE contributions.

In the ferromagnetic region ($B > B_m$), at low temperature (2 K), both $\rho_{xy}(B)$ and $M(B)$ show only weak variations. Therefore, R_0 and R_S are assumed to be field independent. Indeed, on a plot $\rho_{xy}(B)/B$ vs $M(B)/B$, see Fig. 5.3(a), the high field data ($B > B_m$) fall on a straight line which can be fitted by eqn. 5.1 to obtain $R_0 = 0.14\,\mu\Omega \cdot \mathrm{cm/T}$ and $R_S = 3.51\,\mu\Omega \cdot \mathrm{cm/T}$ in good agreement with Ref. 91. In the PM phase, since both ρ_{xy} and M increase linearly with field, the low–field points ($0\,\mathrm{T} < B < 0.4\,\mathrm{T}$) shrink altogether into a single point. This point falls close to the FM line. The data $0.4\,\mathrm{T} < B < 0.8\,\mathrm{T}$ corresponds to the metamagnetic transition regime. Obviously, there is no drastic change of R_0 between PM and FM phases through the metamagnetic tran-

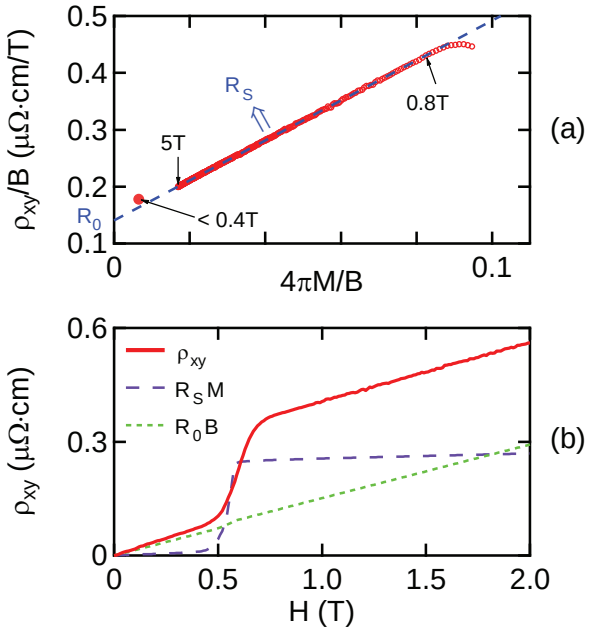

Figure 5.3: a) Determination of the coefficients R_0 and R_S in the FM phase: ρ_{xy}/B vs $4\pi M/B$ plot at 2 K ($P = 0$) up to 5 T, where M is the magnetization density expressed in 10^{-4} emu $\cdot$ cm^{-3} and $B = H + 4\pi M$ is the internal field in Tesla. The high–field part (0.8 T $< B <$ 5 T) is fitted by eqn. 5.1 (dotted line) and we obtain $R_0 = 0.14\,\mu\Omega \cdot$ cm/T and $R_S = 3.51\,\mu\Omega \cdot$ cm/T. The low–field points ($0 < B <$ 0.4 T) shrink altogether into a single point. The data $0.4 < B <$ 0.7 T is not shown here since it corresponds to a transition regime which has no physical interest (different samples for ρ_{xy} and M measurements). b) ρ_{xy} and its constituent contributions R_0B (NHE) and R_SM (AHE) vs H (external field), in the same experimental conditions and using the values of R_0 and R_S obtained in (a).

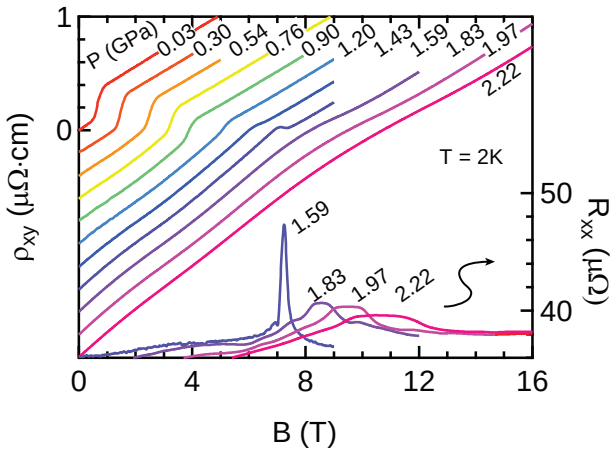

Figure 5.4: Pressure evolution of ρ_{xy} vs B at 2 K for different pressures (labels indicate the pressure in GPa). The curves are vertically spaced by 0.2 $\mu\Omega \cdot$ cm for clarity. In addition, we plot the symmetric part of the measured signal, the magnetoresistance R_{xx}, at $T = 2$ K as a function of B for different pressures (1.59, 1.83, 1.97, and 2.2 GPa, right scale).

sition, thus there is no direct evidence of a Lifshitz transition at B_m.

Figure 5.3(b) shows the field dependence of ρ_{xy} at $T = 2$ K. On the same scale, we plotted the contributions of $R_0 B$ and $R_S M$ as determined in the FM phase shown in Fig. 5.3(a), to compare the relative weight of NHE and AHE. The normal contribution $R_0 B$ is basically linear with H except for a small kink at 0.6 T due to the magnetization density which suddenly amounts to 10% of the internal field ($4\pi M/B \approx 0.1$) when the system becomes ferromagnetic. But since the magnetization only increases very slowly in the FM phase, its consequence on the internal field is negligible, so that $B \approx \mu_0 H$, the applied field. As a consequence, the slope of the $\rho_{xy}(B)$ curve is mainly determined by the NHE ($\partial\rho_{xy}(B)/\partial B \simeq R_0$), and the step of $\rho_{xy}(B)$ at the transition is due to the AHE, mainly. In a simple approach, the jump in the AHE is due to a step–like increase of the magnetization ($\Delta\rho_{xy} \simeq R_S \Delta M$). However, from the experimental data we cannot exclude that also R_S may be affected at the metamagnetic transition, as the resistivity ρ_{xx} — at least in a longitudinal configuration — shows such a step–like increase. Finally, we should mention that the transition appears broader in $\rho_{xy}(B)$ than in $M(B)$. This difference marks the complex interplay between intrinsic and extrinsic (impurity) contributions to the AHE.

5.2.3 Hall Effect under High Pressure

In our pressure study, the Hall effect $\rho_{xy}(B)$ has been measured by performing field scans upwards at various temperatures in the range from 0.15 K up to 20 K. Figure

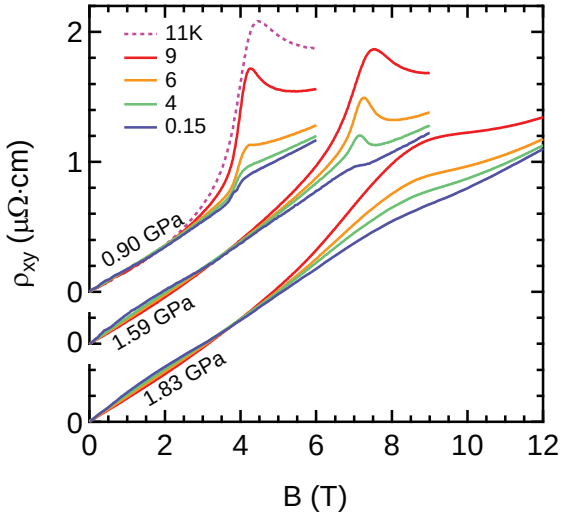

Figure 5.5: ρ_{xy} as a function of field at various temperatures (0.15 to 11 K) under pressure (0.90/1.59/1.83 GPa). For clarity, curves at 1.59 and 1.83 GPa are shifted vertically by -0.4 and $-1\,\mu\Omega\cdot$cm, respectively.

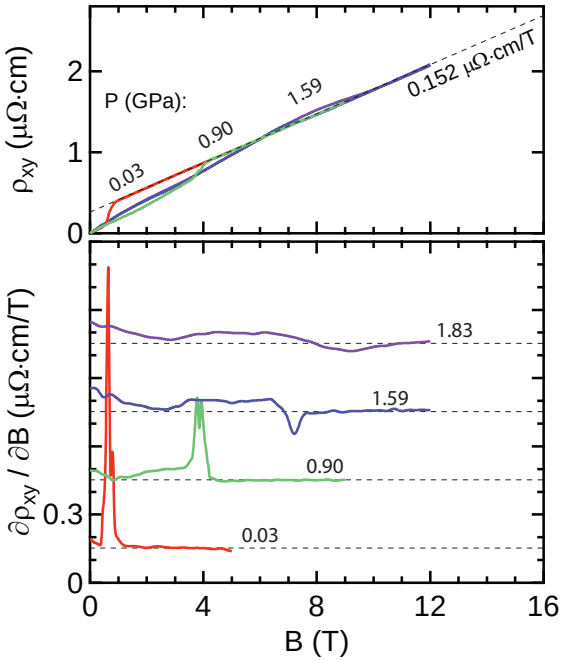

Figure 5.6: (upper panel) ρ_{xy} vs B for various pressures extrapolated to $T = 0$ (labels indicate the pressure in GPa). The dotted line indicates the pressure independent linear increase of ρ_{xy} in the ferromagnetic state above B_m which has a linear slope of 0.152 μΩcm/T. (lower panel) Field dependence of the differential Hall coefficient $\partial\rho_{xy}/\partial B$ for different pressures.

5.4 represents ρ_{xy} as a function of B at $T = 2\,\mathrm{K}$ for various pressures up to 2.22 GPa (the curves are vertically spaced by 0.2 $\mu\Omega cm$ for clarity, respectively). While at low pressures ($P \leq 1.2\,\mathrm{GPa}$) a clear jump of ρ_{xy} at B_m is observed, which is qualitalively similar to the behaviour at ambient pressure, above 1.6 GPa only a rather broad cross–over is observed. This is a first indication that the first order metamagnetic transition collapses in the pressure range from 1.2 GPa to 1.6 GPa, thus the pressure of the quantum critical end point P_{QCEP} is located in this pressure window. In agreement with previous measurements [76], a strong field dependence of ρ_{xx} is also detected at $T = 2\,\mathrm{K}$. The magnetoresistance R_{xx} shows a very sharp peak at $P = 1.59\,\mathrm{GPa}$ while for higher pressures a plateau–like enhancement of R_{xx} is observed. On cooling, it was proved [76] and verified here that the simultaneous enhancement of the residual resistivity and the enhancement of the A coefficient is correlated with crossing through the QCEP.

Next we concentrate on the behaviour of $\rho_{xy}(B)$ at different temperatures which is shown in Fig. 5.5 for $P = 0.9\,\mathrm{GPa}$, 1.59 GPa, and 1.83 GPa. The Hall resistivity ρ_{xy} at different temperatures at 0.9 GPa is rather similar to that at ambient pressure (see Fig. 5.2(b)) with a steplike anomaly at lowest temperatures and a peak which appears with increasing temperature just above B_m. At $P = 1.59\,\mathrm{GPa}$ the behaviour appears likewise, except at lowest temperature (see below). For $P = 1.83\,\mathrm{GPa}$ no sharp anomaly can be detected, but a broad crossover even at the lowest temperature. Furthermore, below 2 K, the temperature dependence of the Hall resistivity is very small for $P < 1.6\,\mathrm{GPa}$ which is close to P_{QCEP}.

While low temperature data have been measured only in the pressure regime where the QCEP is expected, we extrapolated $\rho_{xy}(B)$ measured at finite temperature down to $T = 0$ with a polynomial of second degree for all pressures. As we can see in Fig. 5.5, below 2 K the temperature dependence of the Hall resistivity is very small for $P < 1.6\,\mathrm{GPa}$ — which is supposed to be close to P_{QCEP} — in such a way that the extrapolated $\rho_{xy}(B, T = 0)$ almost coincides with the one measured at the lowest temperature. Figure 5.6 (upper panel) illustrates the pressure evolution of the Hall resistivity in the limit $T \to 0\,\mathrm{K}$ for selected pressures in absolute values. Interestingly, in the entire pressure range, all the $\rho_{xy}(B)$ curves almost match together in the high field part ($B > B_m$). This clearly shows that the normal contribution to the Hall effect, which dominates the field dependence above B_m, as shown in Fig. 5.3, is pressure independent in the polarized ferromagnetic regime and has a constant slope $\mathrm{d}\rho_{xy}/\mathrm{d}B = 0.152\,\mu\Omega\mathrm{cm/T}$ (indicated by the dashed line). The lower panel of Fig. 5.6 shows the field dependence of the differential Hall coefficient $\tilde{R}_H = \partial\rho_{xy}/\partial B$ for selected pressures. At low pressure, a very sharp maximum marks the metamagnetic transition. With increasing pressure, the height of the maximum decreases, while the width stays constant. Apparently, $\mathrm{d}\rho_{xy}/\mathrm{d}B$ has changed its sign at 1.59 GPa, while above 1.6 GPa only a broad crossover appears. The dashed lines in the lower panel of Fig. 5.6 indicate a constant slope of $\mathrm{d}\rho_{xy}/\mathrm{d}B = 0.152\,\mu\Omega\mathrm{cm/T}$ which is pressure independent in the FM state above B_m.

In contrast to the FM phase, the Hall coefficient in the PM phase below P_{QCEP} varies

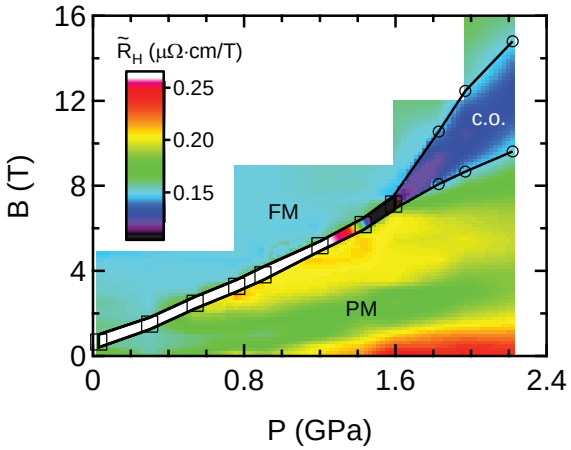

Figure 5.7: Field–pressure phase diagram of UCoAl at 0 K obtained by Hall effect measurements. The colour scale maps the differential Hall coefficient $\tilde{R}_H = \partial\rho_{xy}/\partial B$ obtained from extrapolated curves of Figure 5.6. The bold lines delimit the width of the transition and the lower and upper limits of the crossover region (c.o.). The QCEP is located around (1.6 GPa, 7 T), above which the transition suddenly broadens.

with field and pressure. Even though the $\rho_{xy}(B)$ curves for $P \leq 0.30$ GPa are linear in the low field PM phase, this is not the case at higher pressure, for $P \to P_{QCEP}$.

To summarize the presentation of the experimental data, we plot in Fig. 5.7 the differential Hall coefficient $\tilde{R}_H$ in a (B, P) phase–diagram. It appears clearly that $\tilde{R}_H$ is never constant in the paramagnetic state while it varies little in the ferromagnetic state, as discussed above. The width of the step–like transition at B_m is delimited by solid lines for $P < 1.6$ GPa. One can reasonably affirm that the QCEP is located in the pressure window between the characteristic pressures $P_M = 1.2$ GPa and $P_\Delta = 1.6$ GPa. At P_M, the differential Hall effect is changing sign, while above P_Δ the broadening of the crossover is clearly visible. The robustness of the FM phase contrasts with the variations in the PM phase, in which a valley of low $\tilde{R}_H$ separates two regions of high R_H, one at low field and one at high field. It is interesting to observe that there is no drastic difference between the low pressure FM phase and the polarized paramagnetic phase (PPM) which is expected to occur for $P > P_{QCEP}$ through the crossover regime. As a matter of fact, the pressure decrease of the magnetization in the FM region has no effect in the high magnetic field regime.

The pressure dependence of B_m, defined by the extrema of $\tilde{R_H}$ shown in Fig. 5.7 is in excellent agreement with previous transport measurements [76]. Magnetization measurements [75] led to lower pressure dependence of B_m, as mentioned above. This discrepancy probably comes from pressure inhomogeneities or differences in the crystal quality. The condition of good hydrostaticity may be crucial in UCoAl since the linear compressibility along the a–axis is known to be about 5 times larger than that along the

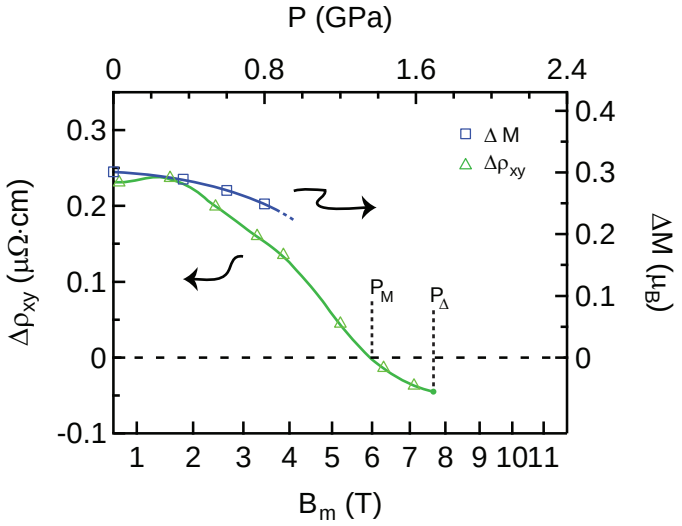

Figure 5.8: Comparison of the jump in $\rho_{xy}(B)$ and $M(B)$ taken from Ref. 75. Data are plotted versus B_m to correct for discrepancy in pressure determination. Top axis indicates our corresponding pressure scale. Lines are guides for the eye. At P_M the positive jump $\delta\rho_{xy}$ vanishes, and above P_Δ only a crossover from the PM to the field induced FM state occurs.

c–axis [52, 94]. In Figure 5.6, at low field, ρ_{xy} appears P–independent. This observation is in good agreement with pressure magnetization data [75] and recent magnetostriction experiments [76] which led to the conclusion that the respective Grüneisen parameter of the magnetization $\Omega_M = \frac{1}{M}\frac{\partial M}{\partial V}V$ is near 2 for $B < B_m$ and 35 for $B > B_m$, while Ω_{B_m}, the Grüneisen parameter of B_m, is near 140.

Figure 5.8 shows the jump $\Delta\rho_{xy}$ at the metamagnetic transition plotted against the critical field B_m. It is compared to the corresponding evolution of the jump of the magnetization ΔM taken from Ref. 75 which decreases slightly with pressure. In order to correct for differences either in P determination, in hydrostaticity or in crystal quality, the data are plotted as a function of B_m. (The upper scale indicates the correspondence with our P determination). In a simple approach $\Delta\rho_{xy} \propto \Delta(R_0 B) + \Delta(R_S M)$. At least up to $P_M = 1.2$ GPa the main contribution to $\Delta\rho_{xy}$ will be the jump in the magnetization ΔM at B_m. However, at 1.43 GPa and 1.59 GPa, the corresponding anomaly in ρ_{xy} at B_m is no more a finite positive $\Delta\rho_{xy}$, but it appears slightly negative. Thus above 1.2 GPa, the apparent signature of the first order metamagnetic transition is not directly detected in the Hall effect measurement. Clearly, above 1.59 GPa no first order transition has been observed, indicating that the QCEP lies between $P_M = 1.3$ GPa and $P_\Delta = 1.7$ GPa. As already mentioned above, previous resistivity measurements pointed out the strong increase of the inelastic term, namely the A coefficient. Obviously, the associated change of the effective mass has a strong influence on the Hall resistivity.

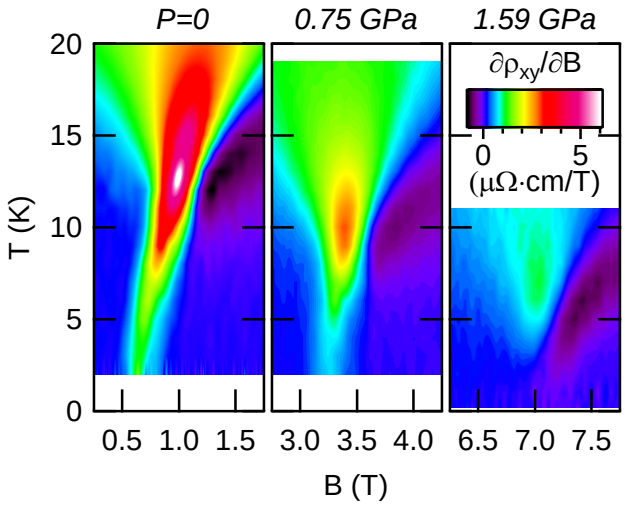

Figure 5.9: (B, T) phase diagram of UCoAl and its evolution under pressure as obtained by Hall effect measurements. The colour scale corresponds to $\partial\rho_{xy}/\partial B$. Each image was obtained from a mesh of field scans at $P = 0$, 0.75 and 1.59 GPa.

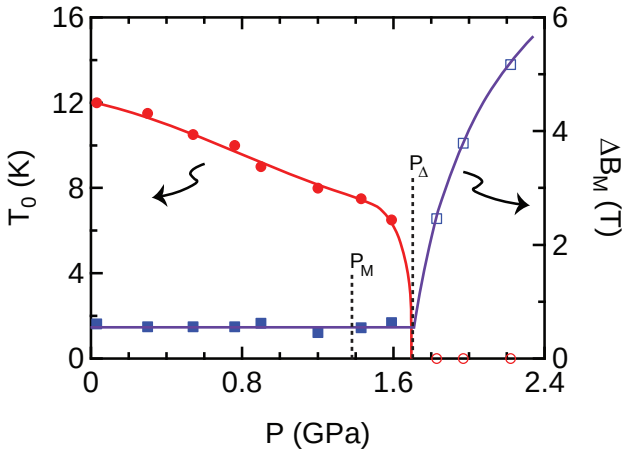

Figure 5.10: Pressure evolution of the critical temperature T_0 (left axis) and the width of the transition at lowest T (right axis), illustrating the clear termination of the transition at $P_\Delta \approx 1.7$ GPa. Lines are guides for the eye.

Finally, in Fig. 5.9 we show $\partial\rho_{xy}(B,T)/\partial B$ for different pressures as a function of magnetic field and temperature for different pressures in a colour plot. The evolution of $\tilde{R}_H(T,B)$ with increasing pressure can be described in simple terms. At ambient pressure, the position of the critical end point is well defined by a sharp maximum in $\tilde{R}_H$. With increasing pressure, the amplitude of $\tilde{R}_H$ at the critical end point decreases, T_0 decreases, and the critical field increases. Figure 5.10 shows the pressure evolution of the temperature of the critical end point T_0 (defined by the maximum of $\tilde{R}_H$) and the width of the metamagnetic transition ΔB_m (width of the peak in $\partial\rho_{xy}/\partial B$). Surprisingly, T_0 is not suppressed continuously to zero temperature but rather drops from $T_0 = 6\,\mathrm{K}$ to zero in the vicinity of $P_\Delta = 1.7\,\mathrm{GPa}$. This pressure also corresponds precisely to the end of the sharp metamagnetism, unambiguously attested by the sudden increase of the transition width ΔB_m on entering a crossover region beyond the QCEP.

5.2.4 Discussion

The Hall effect experiments give detailed insights on the behaviour of the metamagnetic transition in the itinerant heavy fermion system UCoAl. For $T \ll T_0$, the step–like feature of the $\rho_{xy}(B)$ curves is connected to the magnetization jump via the anomalous Hall effect. The constant Hall coefficient in the FM phase at low temperature (field– and pressure–independent) strongly suggests that the coefficients R_0 and R_S do not change with pressure and are the same as at ambient pressure, where they are known with precision. On approaching the QCEP, a drastic change occurs in the Hall signal on crossing B_m. We associate this to the enhancement of the average effective mass detected via the A coefficient in resistivity measurements.

For Ising–type Uranium ferromagnets, as the jump of the magnetization at B_m is often strong (near $0.5\,\mu_\mathrm{B}$) and the renormalized Fermi energy is low, Fermi surface reconstruction can be expected at P_c and B_m as clearly observed in UGe_2 [95]. In the case of UCoAl, at least at low field ($B \ll B_m$) and at high field ($B > B_m$), no major variation of the Hall constant can be pointed out. There is no evident signature of a Fermi surface reconstruction on sweeping from the PM to FM phase for $P < P_{QCEP}$ and from the PM to a polarized paramagnetic phase for $P > P_{QCEP}$. Recent thermoelectric power experiments at ambient pressure were interpreted only via the decrease of the heaviest hole effective mass through B_m [78]. There was also no signature of a Lifshitz transition. By contrast, in the case of the ferromagnetic superconductor UGe_2, the crossing from PM to FM is accompanied by a sign change of the Hall coefficient in excellent agreement with a Fermi surface reconstruction detected in quantum oscillations experiments [96]. However, in these multiband heavy fermion systems, the Hall resistivity response can be complex. A pathological example is the pseudo–metamagnetic transition in $CeRu_2Si_2$ where no clear signature of a Fermi surface reconstruction is detected in

the Hall constant [97] [1] while there is direct evidence of a Fermi surface change through B_m by quantum oscillations experiments [98] associated with a Lifshitz transition. So the question remains open for UCoAl.

It is interesting to recall the case of the ferromagnetic itinerant system $ZrZn_2$ ($T_{Curie} \sim 28.5\,K$, $M_0 \sim 0.17\,\mu_B$ per Zr atom), which is an isotropic Heisenberg system. As in UGe_2, evidences are found for two emerging FM phases (FM_2,FM_1) at low pressure ($P_C \sim 1.65\,GPa$) and one field–induced FM_1 phase when a field is applied from the PM phase above P_c. However, at least for FM_1, it seems that P_{QCEP} almost coincides with P_c [9]. As a consequence, at 2.1 GPa, the crossover metamagnetic field is so low (0.05 T) that the observation of the Fermi surface in the PM regime is proscribed [99]. De Haas – van Alphen measurements pointed out the crossover between the FM_1 and FM_2 phases with an invariance of the Fermi surface topology. The change in the exchange splitting of the Fermi surface is the signature of the field crossover FM_1/FM_2. Let us point out that in the case of $ZrZn_2$ the Fermi energy is weakly renormalized, thus the local fluctuations are negligible compared to the case of U compounds where the itinerant–localized duality is a major part of the puzzle.

Finally, a striking point in our results is the appearance of different field regimes in the low field PM response ($B < B_m$) on approaching P_{QCEP}. It may be connected to the particularity of the quasi–Kagome structure of UCoAl, leading to a complex interplay between frustrated magnetic fluctuations and sole FM interactions. Other evidences of non–conventional FM character of UCoAl is the observation of non–Fermi liquid properties in the PM regime at pressure far below P_{QCEP} [78]. To solve the UCoAl puzzle, key experiments are now to extend the magnetization measurements through the QCEP and of course to succeed to directly observe the Fermi surface.

5.2.5 Conclusions

Hall effect experiments at ambient and at high pressure have been presented in the itinerant metamagnet UCoAl. At the metamagnetic transition B_m, the jump of the Hall effect is dominated by the AHE contribution which scales with the magnetization. The jump at B_m disappears at $P_M \approx 1.3\,GPa$, and above $P_\Delta \approx 1.7\,GPa$ only a broad pseudo–metamagnetic transition could be detected. While the Hall effect in the polarized ferromagnetic state seems to be pressure independent, the interpretation of the field dependence in the paramagnetic state below B_m under pressure on approaching the QCEP appears less straightforward and needs to be revised in the future. Finally, our Hall effect experiments do not allow to conclude on a possible Fermi surface change through the QCEP.

[1] although we must say that a kink in the Hall resistivity was ascribed to a Lifshitz transition in Ref. 73, but in conjunction with other signatures.

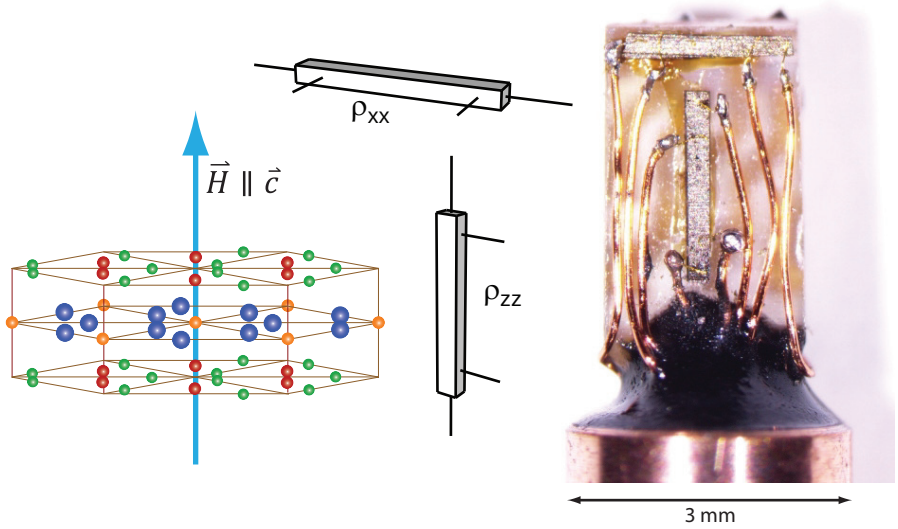

Figure 5.11: Picture of the experimental setup for resistivity measurements of UCoAl under pressure. There are two samples (for the transverse and longitudinal configurations) with $\vec{H} \parallel \vec{c}$.

5.3 Resistivity under pressure

In this section we present a pressure study of the resistivity of UCoAl, down to very low temperature (50 mK), and up to 13 T. Hydrostatic pressure was applied using a piston-cylinder cell. Two samples were mounted in the longitudinal (current $\vec{J} \parallel \vec{H}$) and transverse ($\vec{J} \perp \vec{H}$) configurations, respectively, with field applied along the c-axis (easy magnetization axis) in both cases. (Fig. 5.11). A very low noise level is achieved by using cold transfomers thermalized at the temperature of the 1 K pot, which amplify the signal by a factor 100. In the first subsection, we study the Fermi liquid behaviour using temperature scans of the transverse resistivity. In the second subsection, we study both the transverse and longitudinal magnetoresistivity, with a special focus on hysteresis effects at the metamagnetic transition.

5.3.1 Temperature dependence

Temperature scans of the longitudinal and transverse resistivity (ρ_{zz} and ρ_{xx}, respectively) in the range [0.05-0.7 K] were performed at various fields and pressures. Above $\sim$ 20 K the measurements were perfomed step by step due to the slow thermalization. In the dilution fridge, the T-dependent measurements were performed by continuously recording while decreasing temperature (typical rate -0.2 K/h). The raw data have been processed afterwards, by removing outliers and down-sampling to 2 mK intervals with boxcar smoothing.

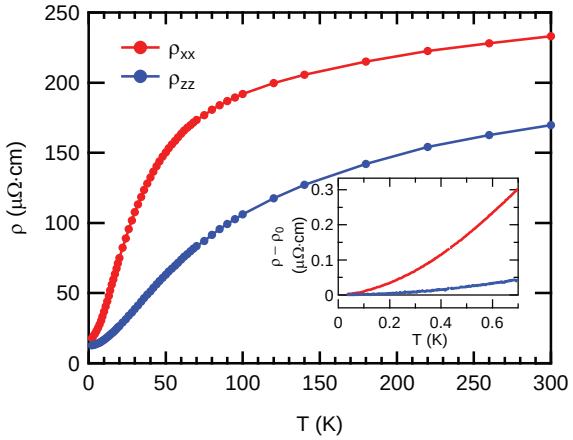

Figure 5.12: Resistivity versus temperature up to 300 K at zero field and $P = 0.28$ GPa, for the transverse (ρ_{xx}) and longitudinal (ρ_{zz}) configurations. Inset shows the low temperature dependence of $(\rho - \rho_0)$.

We started the T-scans at $H = 0$ and increased the field step by step in one direction. As will be discussed in the next subsection (5.3.2), there are strong hysteresis effect between up and down field sweeps around the metamagnetic transition which also influences the value of the A coefficient.

Figure 5.12 shows the resistivity of both samples between 50 mK and 300 K. The residual resistivity ratio $\rho(300\,\mathrm{K})/\rho_0$ is ≈ 13.5 for both samples. In the inset we plot the low temperature part as $(\rho - \rho_0)$. The variation of $\rho(T)$ from 0 K to 700 mK is about 6 times stronger for current along the a axis than along the c axis. In this section we only show the transverse configuration, since the longitudinal has much weaker A coefficient, thus the analysis is much less precise.

In order to test the Fermi liquid behaviour, $\rho_{xx}(T)$ was fitted with a power law of the form:

$$\rho = \rho_0 + AT^{\alpha} \tag{5.2}$$

On the left hand side of Figure 5.13 (for $P < 1$ GPa) and Figure 5.14 (for $P > 1$ GPa), the data are plotted as $(\rho_{xx} - \rho_0)$ vs T^2 together with the fit. On the right hand side, the fit parameters ρ_0, A and α are plotted against the magnetic field. The residual term ρ_0 will be discussed in details in the next subsection (5.3.2). A vertical line indicates the metamagnetic field H_m which is determined by the field sweep measurments, also discussed later.

At the lowest pressure $P = 0.05$ GPa (Fig. 5.13-a) the value of A decreases by a factor ~ 3.5 between 0 and 1 T. The exponent $\alpha \approx 1.5$-1.6 is found at low field, and it changes to $\alpha \approx 1.9$ between 0.6 and 0.8 T, which corresponds to the field

range of the metamagnetic transition ($H_m = 0.7\,\mathrm{T}$) [2]. This is in rather good agreement with previously reported experiments in which ρ_{xx} was fitted with a $T^{5/3}$ dependence [86] in the PM phase, and with a T^2 dependence (Fermi liquid) in the FM phase. The residual resistivity ρ_0 first increases between 0-0.4 T, then shows a plateau (0.4-0.8 T), and finally decreases at 1 T.

As P increases (0.28-0.71 GPa) (Fig. 5.13-b&c) the low-field value of α increases to 1.7-1.85 but is still clearly below 2. Surprisingly, α reaches 2 at a field H_0 which is clearly below H_m: the Fermi liquid character is recovered *within the PM state*. In parallel, the A coefficient shows a two-step decrease : the first decrease occurs around H_0, the second one just before H_m. The residual term ρ_0 shows a similar feature as before : a first increase at low field, followed by a plateau between H_0 and H_m, where it decreases. It increases again at higher fields, in a parabolic fashion. This will be explored in the subsequent part.

At 0.90 GPa (Fig. 5.13-d) the FL behaviour is fully established with $\alpha = 2$ at all fields. The value of A at $H = 0$ is 3 times smaller compared to the ambient pressure. In the field dependence of A, a first decrease occurs at $H_0 = 1$-1.5 T in the continuity of previous pressures, and it is connected with the first maximum of ρ_0. The second shoulder-like anomaly in A grows up, forming a bump just before H_m, while there is now a positive jump in ρ_0 at H_m. Above H_m, A slowly decreases towards a constant value of $0.1\,\mu\Omega.\mathrm{cm.K}^{-2}$.

At higher pressures (Fig. 5.14) A continues to initially decrease, while ρ_0 symmetrically increases up to $H_0 \sim \frac{H_m}{2}$. A now shows a maximum just before H_m, which is sharpest at 1.42 GPa, and then broadens. The amplitude of the positive jump in ρ_0 at H_m increases continuously with pressure, even beyond 1.42 GPa, and at least up to 1.80 GPa, which is the maximum pressure at the current stage.

Summary on the non-Fermi liquid behaviour

The Fermi liquid behaviour is fully established for all fields in the pressure range [0.90-1.22 GPa], but it breaks down at 1.42 GPa at very low temperature. At this particular pressure, $\rho_{xx}(T)$ cannot be fitted with a power law in the entire temperature range [0.05-0.7 K]. Below $\sim$ 400 mK, a power law fit with exponent $\alpha \approx 1.5$ is found at low field, and $\alpha \approx 1.7$ at high field. Above this temperature, $\rho_{xx}(T)$ follows a T^2 law at all fields. Due to the limited temperature range of the power law fit, there is a dispersion of the values α, but it seems that the change of α from ≈ 1.5 to ≈ 1.7 occurs at 4 T.

This «re-entrant» NFL behaviour is also noticeable at 1.62 GPa below 2-3 T, and maybe at 1.80 GPa as well, at zero field only. Around H_m, because of hysteresis effects

[2] the criterion to define H_m is discussed in the field-scans of resistivity.

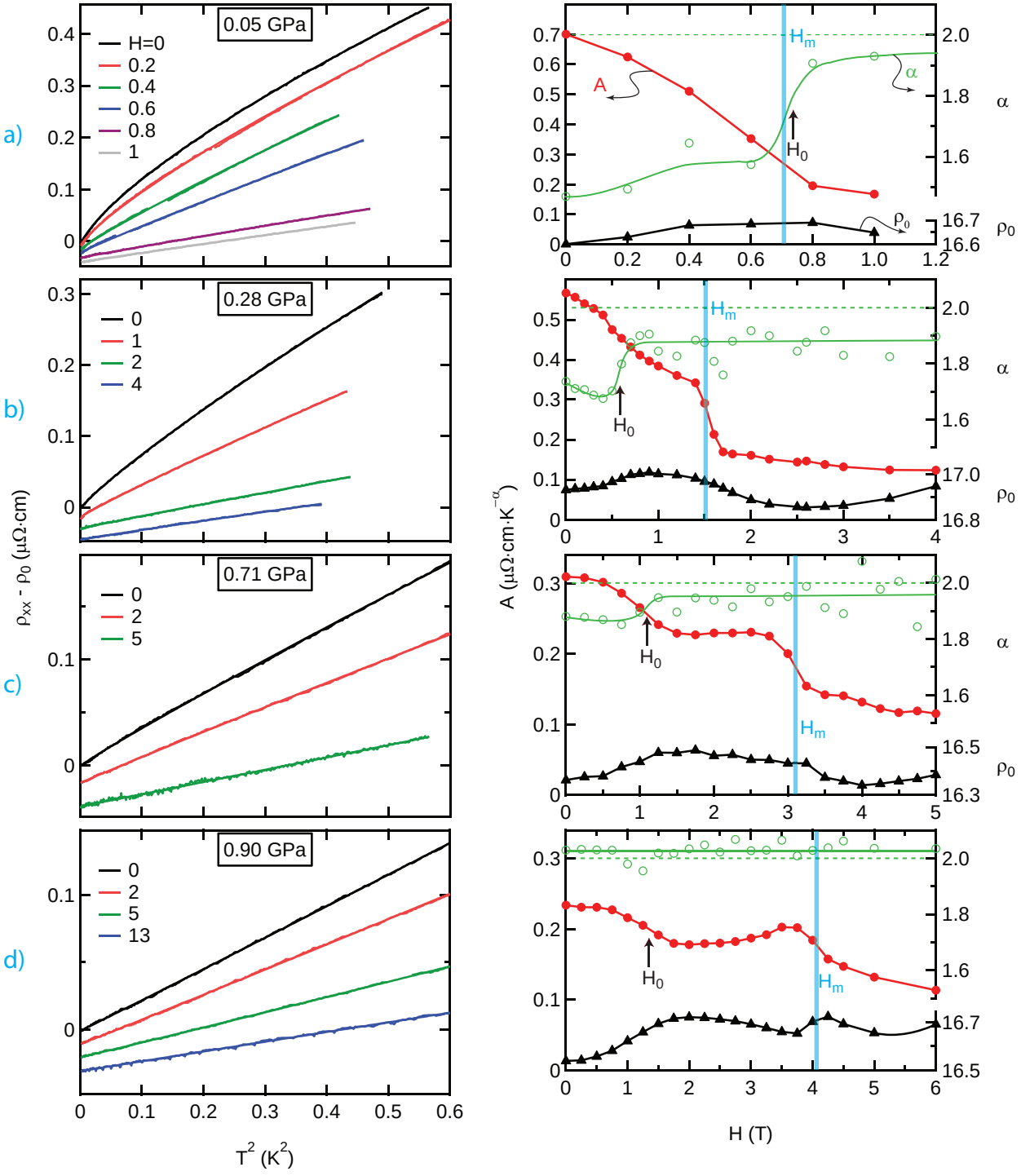

Figure 5.13: Left hand side: T^2 dependence of the transverse resistivity ($H \parallel c$ and $J \parallel a$) at various field values and various pressures: $P = 0, 0.28, 0.71, 0.90$ GPa. Each curve is superimposed with a power law fit (Eq. 5.2), and they are shifted together vertically for clarity. Right hand side: field variation of the exponent α (○), the coefficient A (●) and the residual term ρ_0 (▲) (in μΩ.cm) obtained by fitting $\rho_{xx}(T)$ with Eq. 5.2. Lines are guides for the eye.

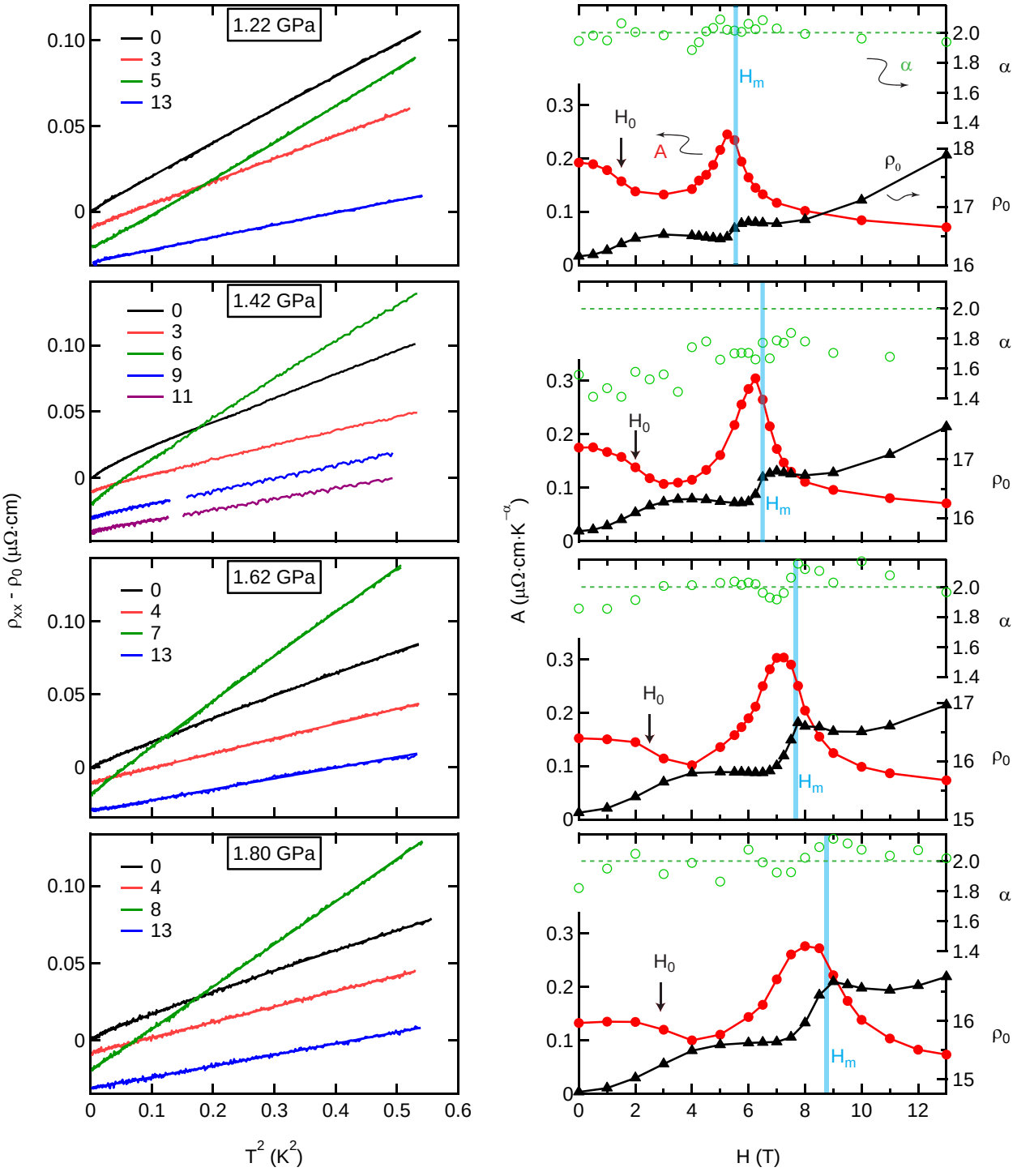

Figure 5.14: Continuation of Fig. 5.13 for the pressures $P = 1.22, 1.42, 1.62, 1.80\,\mathrm{GPa}$. At $P = 1.42\,\mathrm{GPa}$, the fit is successful only up to $0.4\,\mathrm{K}$.

(see next), the $\rho_{xx}(T)$ curves strongly depend on the approach (increasing or decreasing field). Hence, the little variations from the T^2 law observed around H_m are due to the crossing of the metamagnetic transition on cooling, and shall not be considered as a NFL effect. The NFL regions are indicated in the field–pressure phase diagram Figure 5.20.

Summary on the A coefficient

Figure 5.15-a summarizes the A coefficient [3] versus field at all pressures, obtained from temperature sweeps (increasing field step by step). In the inset we plot the value of A at $H = 0$ versus pressure, showing a fast initial decrease up to 0.9 GPa where A is only 1/3 of the intial value, followed by a slow decrease up to the highest pressure. In addition, in Figure 5.15-b we show A determined from field sweep measurements (which will be shown next) at various temperatures between 0.05 K and 0.6 K (typically 5 curves). In the region of H_m, there are strong differences between up and down field sweeps, especially above 1.22 GPa when the maximum of A starts to grow. On top of the broad A enhancement, there is a sharp *positive* peak in *decreasing* sweeps (at $H_m^{\rm dec}$) while there is a sharp *negative* peak in *increasing* sweep (at $H_m^{\rm inc}$). It is worthwhile to note that the maximum of A from T scans is broader and occurs before $H_m^{\rm inc,dec}$.

As a summary, the A coefficient is enhanced in two distinct field and pressure regions:

- At low-pressure–low-field, A is enhanced due to the proximity of FM instability. It is related to the enhancement of C/T [100] by the Kadowaki-Woods relation $A \sim \gamma^2$, in the presence of strong spin fluctuations. A decreases abruptly on entering the FM phase, and also decreases with increasing pressure. This is consistent with the picture of strong spin fluctuations associated with the FM instability.

- A is also enhanced at high-pressure–high-field, with a maximum in the broad pressure–field region around 1.4-1.8 GPa – 6-9 T. This enhancement is associated to the QCEP. This is very similar to the resistivity data reported in Ref. [76].

The values of H_m and H_0 are plotted in the field–pressure phase diragram of UCoAl Figure 5.20. The change of regime between these two distinct field and pressure regions occurs at $\sim$ 1.1 GPa. This is probably connected to the end of the Hall effect jump at $P_M \approx 1.3$ GPa (see Fig. 5.8). The maximum in A coefficient around ≈ 1.6 GPa, is maybe connected to the end of the sharp transition in Hall effect, at $P_\Delta \approx 1.7$ GPa (see Fig. 5.10). We thus retrieve the characteristic pressures P_M and P_Δ established by Hall effect measurements (Section 5.2).

[3] The A cofficients obtained from power law fits with different α exponent have different units, so in principle they should not be plotted on the same scale. But when the exponent is close to 2, the value of A is only weakly affected when forcing the fit with $\alpha = 2$. For this reason, in the summary of A vs H for all pressures (Fig. 5.15), we show the values obtained by fitting $\rho_{xx}(T)$ with a T^2 law.

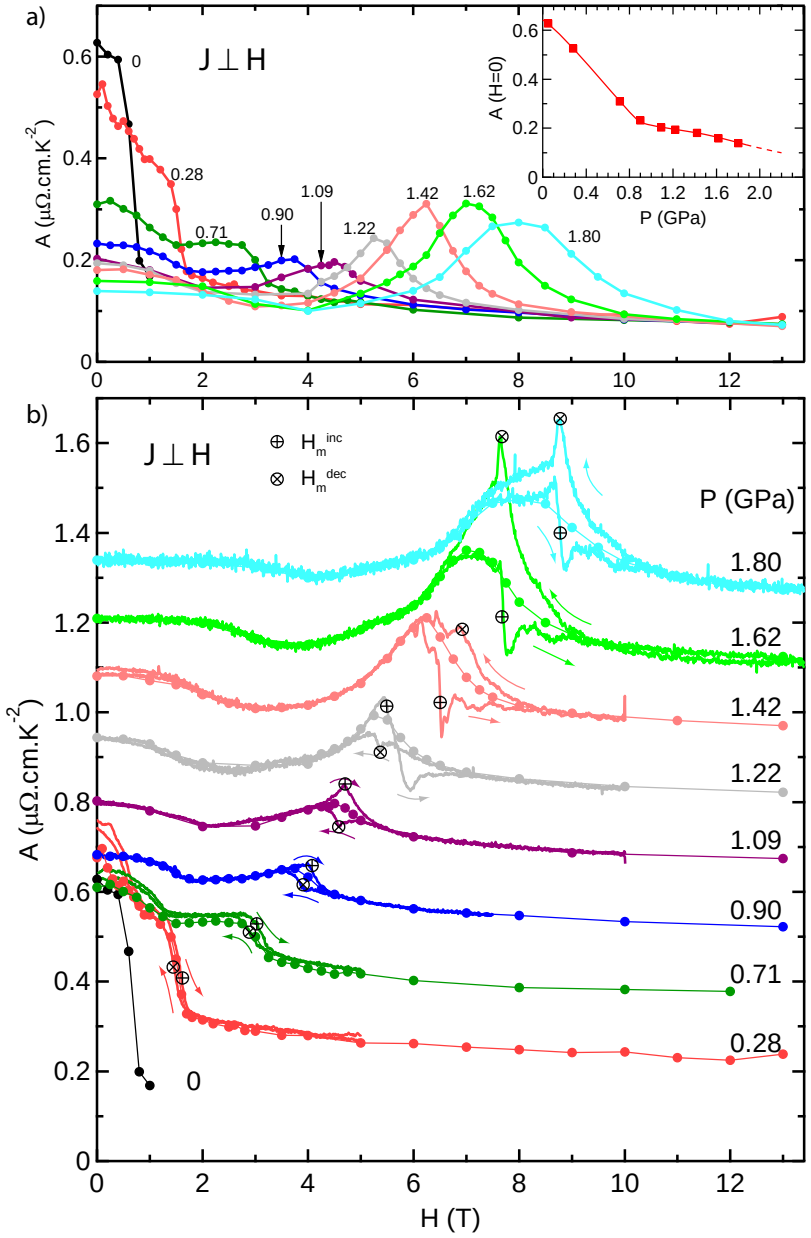

Figure 5.15: a) A coefficient vs field, at various pressures, obtained from T^2 law fit of ρ_{xx} in the range [0.05-0.6 K], from temperature scans (dots). b) these values of A are shifted vertically, and plotted along with A determined from up and down field scans (continuous lines). The fits were obtained over the same temperature range, involving ~ 300 points in the T scans, and only ~ 5 points in the H scans. Labels indicate the pressure in GPa. Arrows indicate the field sweep direction, and markers indicate $H_m^{\rm inc,dec}$. Inset of panel (a) shows the value of A at $H = 0$ versus pressure. The line is a guide for the eye.

5.3.2 Field dependence — pressure $P \approx 0$

Figure 5.16 shows the magnetoresistivity of UCoAl in the transverse (ρ_{xx}) and longitudinal (ρ_{zz}) configurations, at $P = 0$. These measurements were performed in a PPMS down to 5 K, without a pressure cell. At 5 K, when going from the PM to FM state, $\rho_{xx}(H)$ undergoes a step-like decrease and $\rho_{zz}(H)$ a step-like increase. As temperature increases, both ρ_{xx} and ρ_{zz} show a peak at the transition. The peak is maximum at 11 K, marking the end of the first order transition: the critical endpoint (CEP) is located at $T_0 = 12\,\mathrm{K}, H_m^\star = 1\,\mathrm{T}$, in agreement with other measurements (thermoelectricity [78], NMR [22, 77], etc.).

The increased resistivity around the CEP is ascribed to the scattering on spin fluctuations [77].

In Figure 5.17, the field dependence of resistivity was measured down to 50 mK in a dilution fridge, with the samples inside the piston-cylinder pressure cell. The pressure cell had been closed with as little force as possible, just enough to seal the pressure chamber with the Daphne oil in it. At low temperature, the pressure was found to be 0.05 GPa. In the longitudinal sample, H_m is already shifted to 1 T by the small pressure. Below 1 K the jump in ρ_{xx} collapses, leaving only a small kink at 50 mK. On the contrary, ρ_{zz} still shows a sharp jump at the lowest temperature. There is a hysteretic behaviour in both configurations. In the longitudinal, the hysteresis loop opens up notably in $\rho_{zz}(H)$ on cooling below 4.2 K. In the transverse, the hysteresis consists of a shift of the hump. This is a rather unusual shape at 50 mK, due to the collapse of the jump in $\rho_{xx}(H)$

To summarize, at (almost) zero pressure, there are 3 important differences between ρ_{xx} and ρ_{zz}:

- i) opposite variation at the metamagnetic transition
- ii) when $T \to 0$ the jump in $\rho_{xx}(H)$ vanishes, while it stays constant in $\rho_{zz}(H)$
- iii) the A coefficient is much larger in ρ_{xx}

These differences occur at low temperature $T << T_0$. At higher temperature, both configurations show a peak in the vicinity of the CEP ($T_0 \sim 11$ K) and a broad maximum in the crossover regime ($T > T_0$).

5.3.3 Pressure study — Intermediate Temperatures — Critical EndPoint

Figure 5.18-a shows field-scans $\rho_{zz}(H)$ and $\rho_{xx}(H)$, every 1 K from 50 mK up to 14 K, for 3 different pressures.

In the longitudinal configuration, the pressure evolution does not change the description given at $P = 0$. There is always a positive step at the metamagnetic transition. On

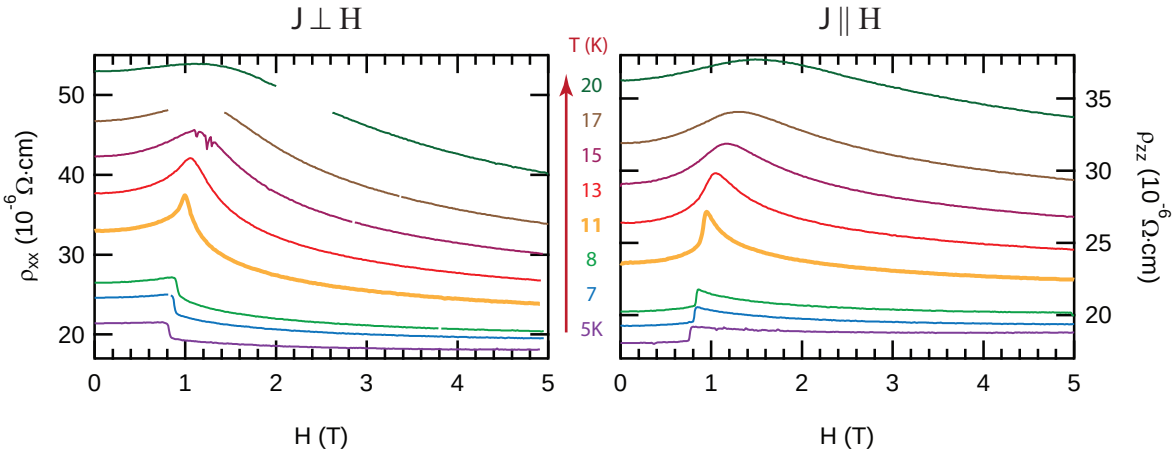

Figure 5.16: Magnetoresistance of UCoAl at zero pressure for $H \parallel c$ in the transverse ($J \parallel a$, left panel) and longitudinal ($J \parallel c$, right panel) configurations. The temperature $T_0 = 11\,\mathrm{K}$ corresponds to the sharpest peak (bold line).

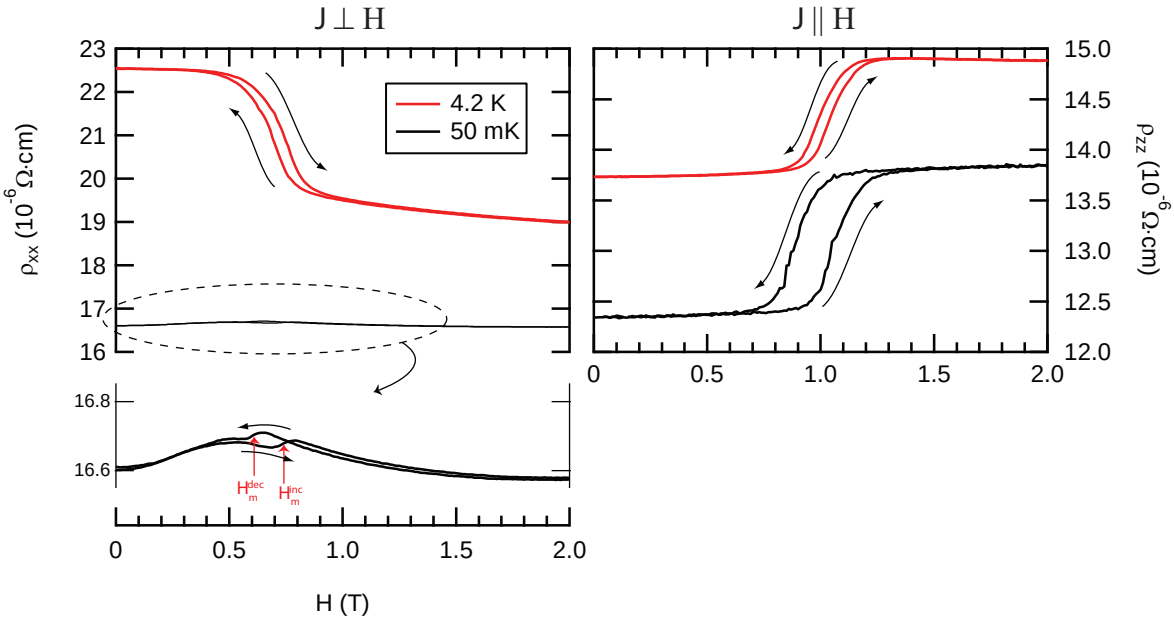

Figure 5.17: Magnetoresistance of UCoAl at $T = 4.2\,\mathrm{K}$ and 50 mK ($P = 0.05\,\mathrm{GPa}$), in the transverse ($\vec{J} \perp \vec{H}$, left panel) and longitudinal ($\vec{J} \parallel \vec{H}$, right panel) configurations, showing up and down sweeps. The curves at 50 mK for the transverse configuration are also shown on an expanded scale.

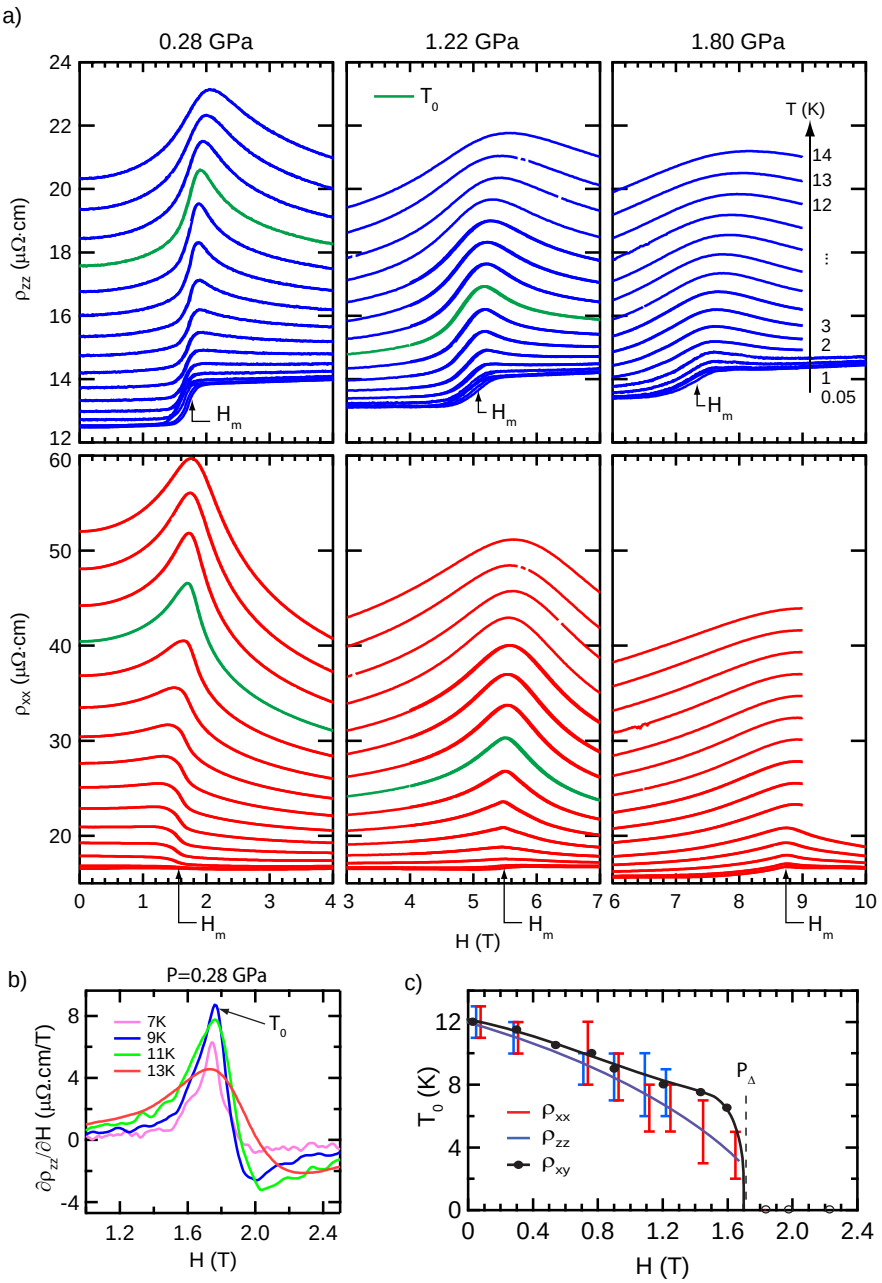

Figure 5.18: a) Longitudinal (ρ_{zz}) and transverse magnetoresistivity (ρ_{xx}) versus field at various temperatures (50 mK,1 K,... every 1 K up to 14 K) for 3 different pressures. Green curves indicate the temperature T_0 of the CEP, which is determined as the sharpest peak (sharpest change in $\partial\rho/\partial H$, panel b). Panel c shows the pressure evolution of T_0 from both resistivity configurations, and from Hall effect.

the contrary, the negative step in the transverse resistivity changes into a positive step at high pressure. The temperature T_0 of the critical endpoint is indicated by the green curve in each plot. T_0 corresponds to the sharpest peak, determined by the sharpest variation of $\partial\rho/\partial H$, as shown in Figure 5.18-b. At low pressure, the sharpest peak is rather well defined, so the temperature T_0 of the critical endpoint is well determined. As pressure increases, T_0 decreases, and the peak in resistivity is less pronounced. In $\rho_{zz}(H)$, because of the broadening of the transition, we cannot distinguish the CEP above 1.22 GPa. In $\rho_{xx}(H)$, we can track the CEP down to $T_0 \approx 3.5 \pm 1.5$ K at 1.62 GPa, but to decide whether there is a sharpest peak is rather subjective, since it is impossible to define T_0 from $\partial\rho/\partial H$. The pressure evolution of T_0 is shown in Figure Fig 5.18-c.

Finally, the increase of H_m with pressure is slightly lower in the longitudinal configuration: at 1.80 GPa, $H_m^{xx} = 8.8$ T while $H_m^{zz} = 7.4$ T. This is probably due to a little pressure inhomogeneity in the sample chamber.

5.3.4 Pressure study — Low temperature

Next we want to discuss the H dependence of ρ_{xx} and ρ_{xx} at low temperature. Previously we observed several anomalies in the H dependence of ρ_0 and the A coefficient. Here we will concentrate on the field range around H_m and discuss the observed hysteresis. The field sweep rate was typically 0.03 T/min at the lowest temperature, and we checked that the data were perfectly reproducible for twice faster and twice slower sweep rate, so we ensured that the observed hysteresis effect were not an artifact due to the instrumental time response.

Field scans at lowest temperature (50 mK)

The pressure evolution of resistivity versus field, at the lowest temperature (50 mK), is presented in Figure 5.19 for both configurations.

The longitudinal configuration (Fig. 5.19-a) is the simplest case to start with: there is a clear step-like increase at H_m, and the shape of the transition is conserved at all pressures. In the PM state, ρ_{zz} increases with pressure, but it is not affected by pressure in the FM state. In the PM state, $\rho_{zz}(H)$ is basically flat from $H = 0$ to $H_0 \sim \frac{H_m}{2}$, and shows a broad kink between $H_0 \sim \frac{H_m}{2}$ and H_m. Above H_m, $\rho_{zz}(H)$ has a constant slope of 0.072 μΩ.cm/T, which is pressure-independent. The hysteresis loop at H_m reduces with pressure, but it is still visible at 1.93 GPa (see Fig. 5.23). At 1.80 GPa, a bump starts to build up above the transition, and gets more pronounced at 1.93 GPa. From these data it is difficult to locate the critical pressure where the metamagnetism vanishes.

The transverse magnetoresistivity has many particularities (Fig. 5.19-b,c). For all pressures, $\rho_{xx}(H)$ initially increases up to $H_0 \sim \frac{H_m}{2}$ from where it forms a broad plateau until the transition occurs (H_0 is related to a feature in A coefficient). In the high field limit, it increases again in a parabolic H^2 dependence. At the transition, the shape of

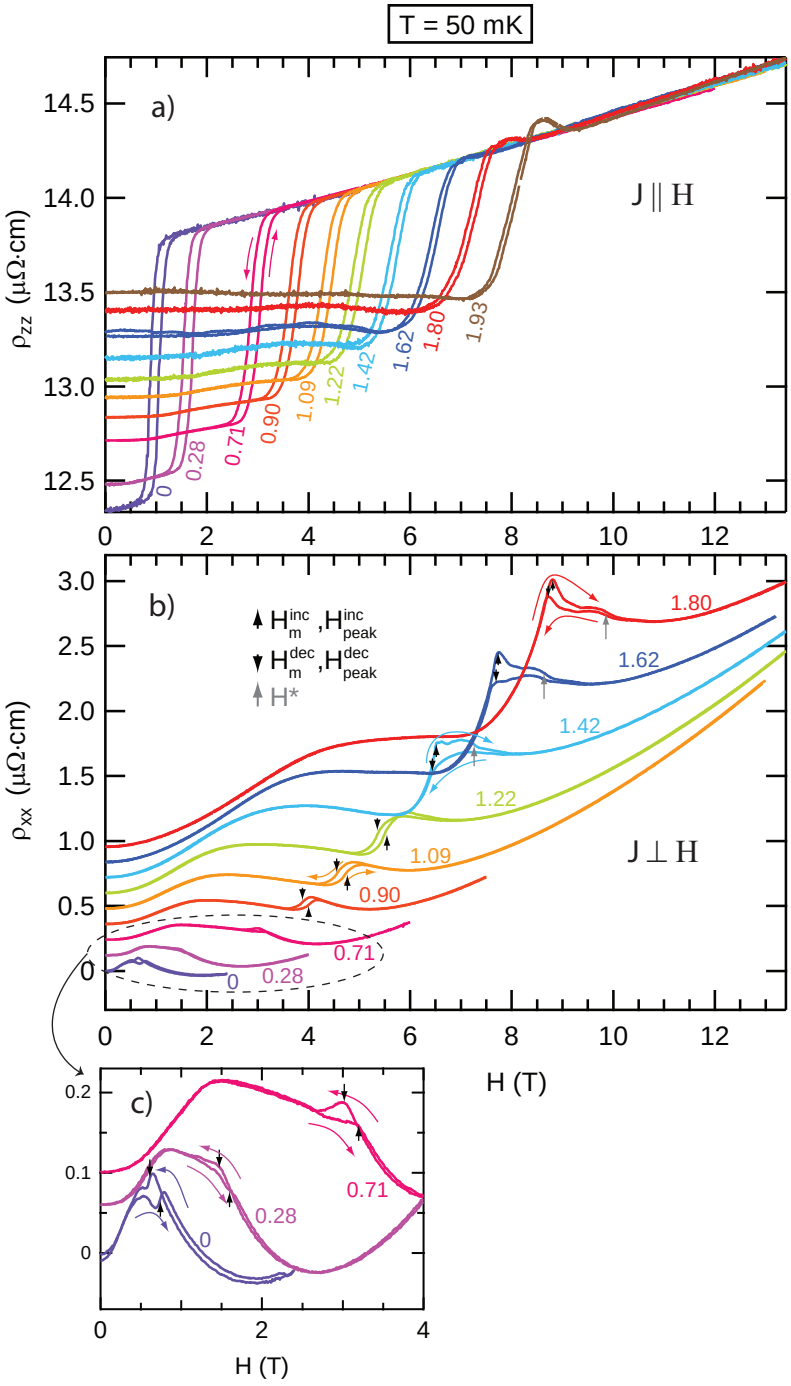

Figure 5.19: Magnetoresistivity at 50 mK for various pressures, a) in the longitudinal and b) transverse configurations. In [b], the curves are shifted vertically for clarity. Panel [c] shows the low-pressure transverse resistivity on an expanded scale. Labels indicate the pressure values in GPa. Colour arrows indicate the field sweep direction (up or down). Black arrows indicate the metamagnetic field $H_m^{\mathrm{inc,dec}}$ (denoted $H_{\mathrm{peak}}^{\mathrm{inc,dec}}$ above 1.22 GPa) for increasing and decreasing field sweeps. Grey arrows indicate the anomaly $H^\star$.

$\rho_{xx}(H)$ is strongly modified by pressure, and notable differences arise between up-sweep ($\rho_{xx}^{\mathrm{inc}}(H)$) and down-sweep ($\rho_{xx}^{\mathrm{dec}}(H)$). We can describe the transverse magnetoresistivity at different pressures (Fig. 5.19-b,c) as follows:

$P = 0$: $\rho_{xx}^{\mathrm{inc}}(H)$ and $\rho_{xx}^{\mathrm{dec}}(H)$ show an anomaly with opposite sign

$P = 0.28\,\mathrm{GPa}$: the plateau appears between $[\frac{H_m}{2}, H_m]$, and the hysteresis consists in a little shoulder on $\rho_{xx}^{\mathrm{dec}}(H)$

$P = 0.71\,\mathrm{GPa}$: $\rho_{xx}^{\mathrm{dec}}(H)$ starts to show a little peak at the transition

$P = 0.90$,$1.09\,\mathrm{GPa}$: ρ_{xx} now has a positive step on entering the FM phase. Up and down sweeps are similar with a hysteresis ΔH

$P = 1.22\,\mathrm{GPa}$: in addition to the hysteresis ΔH, there is now a positive hump in $\rho_{xx}^{\mathrm{inc}}(H)$

$P = 1.42\,\mathrm{GPa}$: up and down sweeps are now very different in the transition region. A two-bump structure builds up at H_m (which is now referred to as H_{peak}) and at $H^\star$, in $\rho_{xx}^{\mathrm{inc}}(H)$ only, while $\rho_{xx}^{\mathrm{dec}}(H)$ is smooth. Thus we cannot infer the hysteresis ΔH at the lowest temperature [4].

$P = 1.62$,$1.80\,\mathrm{GPa}$: the first bump grows up into a peak at H_{peak}, while the second bump at $H^\star$ remains a shoulder-like anomaly and drifts away from the first peak. $\rho_{xx}^{\mathrm{dec}}(H)$ starts to present the same features as $\rho_{xx}^{\mathrm{inc}}(H)$, in such a way that the difference between up and down sweeps fades out.

The pressure evolution of H_m, H_{peak}, and $H^\star$, draws the H–T phase diagram of UCoAl in the limit $T \to 0$ (Fig. 5.20). H_m (and H_{peak}) increases almost linearly with pressure. The increase of H_m is slower in the longitudinal sample, probably because of a little pressure inhomogeneity. The phase diagram under pressure obtained with transverse resistivity is in good agreement with the two reported experiments [76, 79]. To our knowledge, there is no report on longitudinal resistivity in the literature.

The broad anomaly at $H_0 \sim H_m/2$ occurs at all pressures, mostly in the transverse resistivity (there is also a corresponding anomaly in ρ_{zz}, which is much weaker, and disappears at 1.93 GPa). It may result from a competition between the scattering near H_m and the orbital effect due to the cyclotron motion of the quasiparticles, although we cannot rule out that this kink may also be the signature of a Lifshitz transition within the PM state [5].

At high field ($H >> H_m$), a $\rho_{xx} \sim H^2$ is observed, with no sign of saturation up to the highest field (13.4 T). This parabolic field dependence is the typical scattering

[4] but we can infer ΔH at higher temperature, see next.

[5] M. Brando (private discussions)

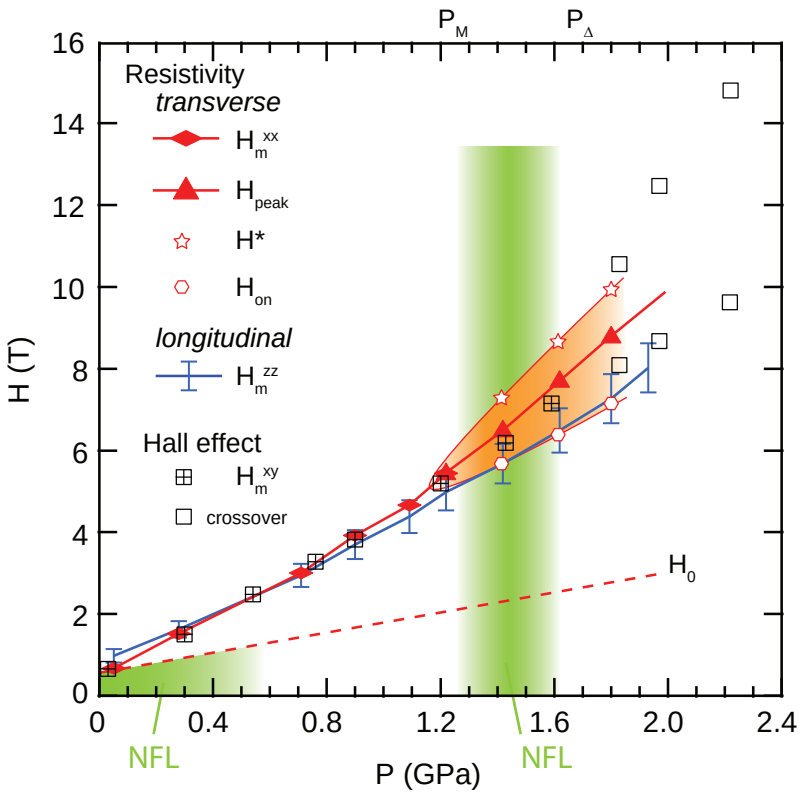

Figure 5.20: Field–pressure phase diagram of UCoAl (for $T \to 0\,\mathrm{K}$) from transverse (red) and longitudinal (blue) resistivity, and Hall effect (black). We indicate the non-Fermi liquid (NFL) regions (green), and the unknown phase (orange) between H_{on} and $H^{\star}$ where up-down difference is observed in transverse resistivity. We also indicate the characteristic pressures P_M and P_{Δ}.

contribution due to the cyclotron motion of the quasiparticles in a compensated metal, with closed Fermi surface. It would saturate if it were not a compensated metal. In the other configuration, there is a constant positive magnetoresistance $\rho_{zz} \sim H$, which necessarily occurs for non-spherical Fermi surface [6].

The plateau of resistivity that appears above 1.22 GPa between $H_{\rm peak}$ and $H^\star$ have already been reported by F. Honda and D. Aoki [76, 79]. This plateau of residual resistivity is observed only in the transverse configuration, whereas the enhancement of A coefficient occurs in both configurations (not shown here). This indicates that the temperature-dependent scattering is rather isotropic, while the residual scattering is highly anisotropic. This is in good agreement with the mechanism of residual resistivity enhancement predicted at a ferromagnetic quantum phase transition [101].

Hysteresis ΔH

At every pressure, we performed up and down field scans at various temperatures, typically every 0.2 K from 0.05 to 2 K, and every 1 K above, in order to get a fine mapping of the phase diagram in the low temperature region. A selection of scans are presented for the longitudinal sample (Fig. 5.21) and the transverse sample (Fig. 5.22), in which we can see the reducing of the hysteresis when temperature increases. In addition to the hysteresis ΔH (which is observed in both samples), there is a difference in absolute value between up and down field sweeps, only in the transverse configuration. This unconventional feature will be referred to as *up-down difference*, noted $\Delta\rho_{xx}$. First, we focus on the «conventional» hysteresis.

The evolution of the hysteresis ΔH with temperature and pressure is shown in Fig. 5.23) for the two configurations. It is plotted along with the temperature T_0 of the maximum resistivity enhancement around the CEP, determined earlier (see Fig 5.18).

In the longitudinal sample, the hysteresis width is clearly defined. But in the case of the transverse sample, the shape of the hysteresis changes with pressure, in such a way that up and down sweeps are not always super-imposable. We indicate in the insets of Fig. 5.23-a & b how the hysteresis width was determined.

ΔH decreases with increasing temperature and reaches the instrumental limit, which is the hysteresis of the superconducting magnet (≈ 0.02 T). At low pressure (0.28 GPa), the reducing of ΔH with T looks like an exponential decay, so the temperature $T_{\rm hyst}$ where it collapses is not well defined ($T_{\rm hyst}(P=0) \approx 7$ K). Up to 1.22 GPa, $\Delta H(T)$ is almost pressure-independent, at least up to 4 K (no hysteresis data available at higher temperature for these pressures). Further increasing pressure ($P > 1.22$ GPa), $\Delta H(T=0)$ reduces and the temperature decay is faster ($T_{\rm hyst}$ decreases). The pressure evolution of $\Delta H(T=0)$ and $T_{\rm hyst}$ are summarized in Figure 5.23-c. By extrapolation, it seems that the hysteresis will collapse at $2-2.2$ GPa, similarly to T_0. This is probably indicating

[6] H. Harima (private discussions)

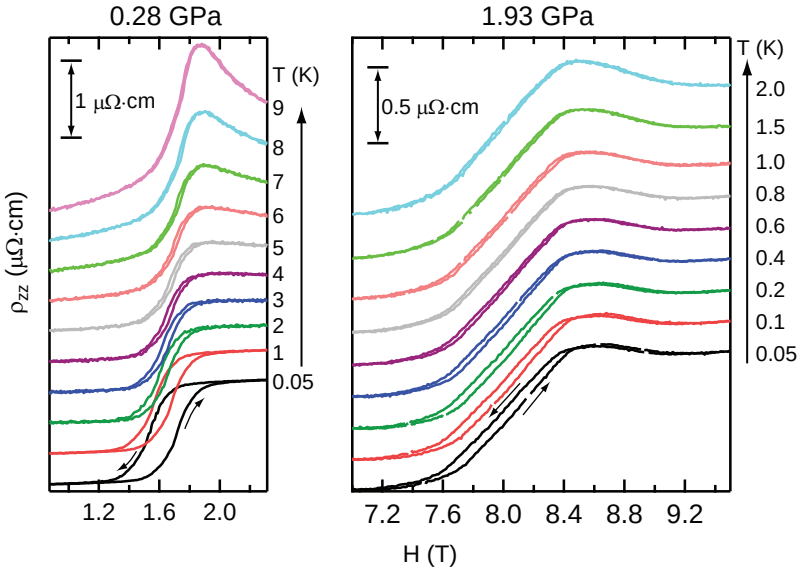

Figure 5.21: Longitudinal magnetoresistivity ρ_{zz} vs H — details of the hysteresis for $P = 0.28$ and 1.93 GPa. Labels indicate the temperature.

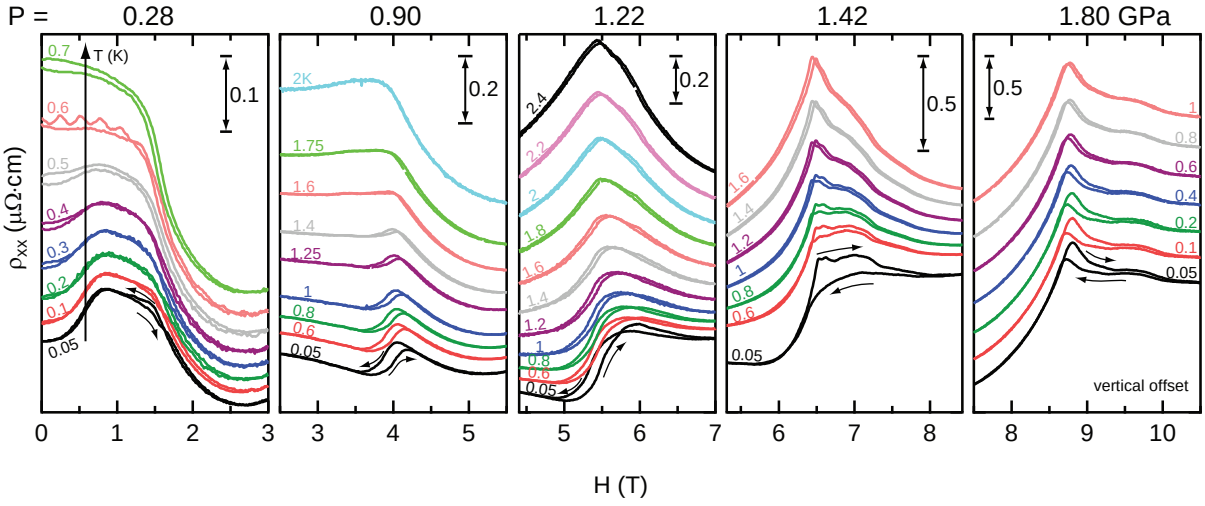

Figure 5.22: Transverse magnetoresistivity ρ_{xx} vs H — details of the hysteresis for various pressures (top labels). Colour labels indicate the temperature.

the termination of the QCEP region.

We can try to relate these results to the characteristic pressures of the Hall effect $P_M \approx 1.3\,\mathrm{GPa}$ and $P_\Delta \approx 1.7\,\mathrm{GPa}$. The hysteresis starts to reduce at $P \approx 1.3\,\mathrm{GPa} \approx P_M$, and will collapse at $P \approx 2\,\mathrm{GPa}$ which is close to P_Δ.

Yet the hysteresis ΔH seems to vanish at $T_{\mathrm{hyst}} < T_0$.

Unconventional up-down difference $\Delta\rho_{xx}$

We already mentioned that there is an unconventional difference in ρ_{xx} between up and down sweeps 50 mK (sub kelvin range), around H_m, for pressures above 1.22 GPa (Figs. 5.19), and in Figure 5.22 we saw that this up-down difference $\Delta\rho_{xx}$ decreases with increasing temperature. In order to study this feature, we must compensate the conventional hysteresis that we have studied in the previous paragraph. We thus define the up-down difference of the transverse resistivity as:

$$\Delta\rho_{xx}(H) = \rho_{xx}^{\mathrm{inc}}(H + \frac{\Delta H}{2}) - \rho_{xx}^{\mathrm{dec}}(H - \frac{\Delta H}{2}) \tag{5.3}$$

where ΔH is the hysteresis that has been determined before (see Fig. 5.23-b). [7]

$\Delta\rho_{xx}(H)$ is plotted in Figure 5.24 at various pressures ($P = 1.22, 1.42, 1.62, 1.80\,\mathrm{GPa}$) and various temperatures.

$\Delta\rho_{xx}(H)$ has a triangular shape, with a sharp maximum at H_{peak}. In order to describe $\Delta\rho_{xx}$, we must introduce new characters: it is delimited between fields H_{on} and $H^\star$ (defined earlier), and below the temperature T_V.

$\Delta\rho_{xx}$ appears very small at 1.22 GPa below $T_V = 0.6\,\mathrm{K}$. It is largest at 1.42 GPa, with the highest temperature limit $T_V = 1.8\,\mathrm{K}$. At higher pressure, $\Delta\rho_{xx}$ decreases and broadens gradually, and the temperature limit decreases: $T_V = 1.4\,\mathrm{K}$ at 1.62 GPa, and 1 K at 1.80 GPa.

The peak of $\Delta\rho_{xx}(H)$ occurs at H_{peak}. At 1.42 GPa, there is a shouldering after the peak, and a tail after $H^\star$. At higher pressure, the anomaly around $H^\star$ is present in both $\rho_{xx}^{\mathrm{inc}}(H)$ and $\rho_{xx}^{\mathrm{dec}}(H)$, in such a way that it cancels out in the substraction. Consequently, $\Delta\rho_{xx}(H)$ is left with a symmetrical peak shape, in contrast with the highly asymmetrical shape of the parent curves $\rho_{xx}(H)$.

Finally, the values of H_{on}, $H^\star$, and H_{peak} are plotted in the H–P phase diagram of UCoAl (Fig. 5.20). They delimit the region where up-down difference occurs in the transverse magneoresistivity. We remark that this region exactly corresponds to the enhancement of the A coefficient.

[7] at 1.42 GPa, we could not determine ΔH below 1.2 K because $\rho_{xx}^{\mathrm{dec}}(H)$ is smooth, so we extrapolated ΔH at low T using an exponential law.

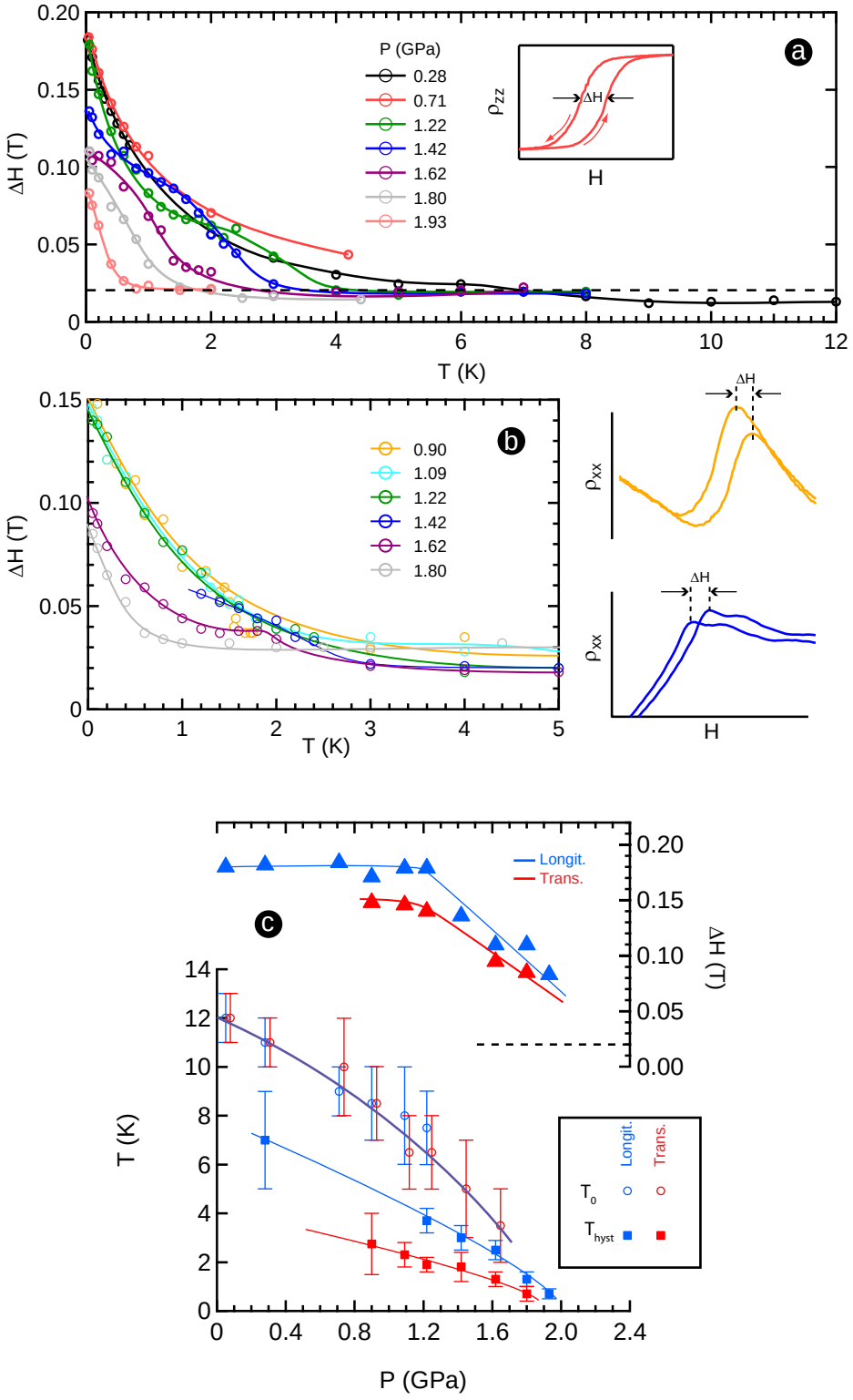

Figure 5.23: a) Longitudinal and, b) transverse hysteresis width ΔH vs temperature, at various pressures. The dashed line indicates approximatively the residual hysteresis of the superconducting magnet (200 Oe). Insets show examples of hysteresis loops. c) Pressure dependence of ΔH at 50 mK (right scale) and of $T_{\rm hyst}$ and T_0 (left scale). $T_{\rm hyst}$ is the temperature at which the hysteresis collapses, and T_0 is the sharpest peak in $\rho(H)$ (see Fig. 5.18) for longitudinal (blue) and transverse (red) samples. Lines are guides for the eye.

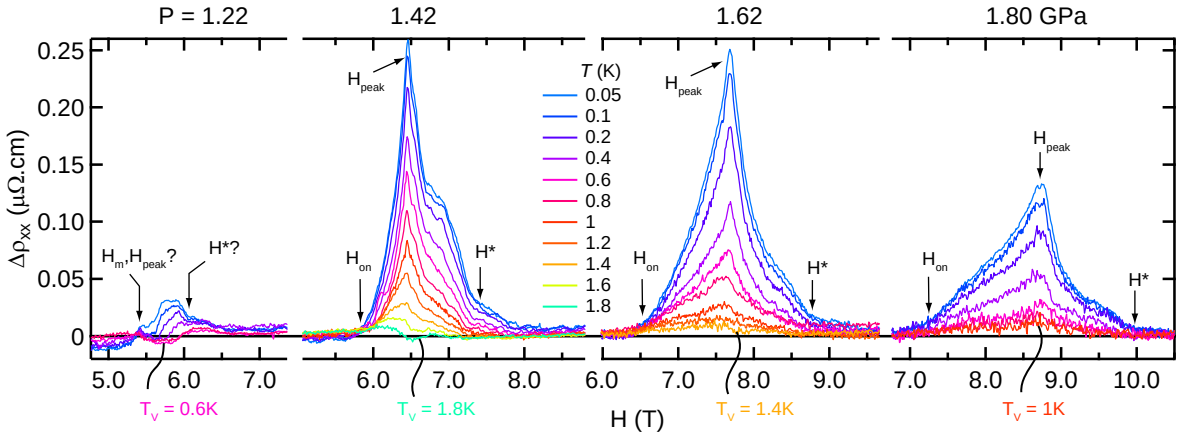

Figure 5.24: Up-down difference $\Delta\rho_{xx}(H) = \rho_{xx}^{\rm inc}(H + \frac{\Delta H}{2}) - \rho_{xx}^{\rm dec}(H - \frac{\Delta H}{2})$, at various temperatures (colour scale), at $P = 1.22, 1.42, 1.62, 1.80$ GPa. We indicate the fields $H_{\rm on}$, $H_{\rm peak}$, $H^\star$ and temperature T_V (see in text). Horizontal axis is broken.

5.3.5 Discussion

Where is the QCEP?

The transverse resistivity has many variations in temperature, field and pressure, which are different from the longitudinal resistivity. Hence it is not clear where the QCEP is located. The difficulty to localize the QCEP was also noted in the Hall effect measurements (two characteristic pressures $P_M = 1.3$ GPa and $P_\Delta = 1.7$ GPa) (see Section 5.2). In our resistivity measurements, we also identified these characteristic pressures P_M and P_Δ:

We observe strong changes in ρ_{xx} around $\sim 1.1 - 1.4$ GPa: the A coefficient reaches a low value at zero field and rises at H_m, the jump in the transverse magnetoresistance $\rho_0^{xx}(H)$ changes sign and starts to exhibit a peak followed by a plateau, the hysteresis ΔH starts to reduce, and an unconventional up-down difference opens up. This corresponds to the characteristic pressure P_M where the jump in Hall effect changes sign. In difference, the longitudinal sample shows no spectacular change at P_M: just the reducing of the hysteresis ΔH.

For both configurations, we could follow T_0 under pressure, though with a large uncertainty. It seems to reach 0 K somewhere between 1.6-2.2 GPa (Fig. 5.18). The hysteresis between up and down field sweeps was observed in both configurations up to the highest pressure of the experiment (1.93 GPa for $\rho_{zz}(H)$). It seems that $T_{\rm hyst}$ and ΔH are going to collapse around 2 GPa, in both longitudinal and transverse configurations (Fig. 5.23-c). This characteristic pressure of 2 GPa is probably the equivalent of $P_\Delta = 1.7$ GPa where the Hall effect anomaly collapses. The little discrepancy may be due to sample dependence or pressure inhomogeneity.

To summarize, there is a large ambiguity on the location of the QCEP, between 1.2–2.2 GPa and between 6–10 T. This is not an uncertainty due to instrumental limitation. In fact, the QCEP seems to be hidden by the formation of a new phase. To study further the QCEP, thermodynamic probes such as NMR are desired.

Possible scenarios for a new phase around the QCEP

In this paragraph we wish to review some reported examples which could be related to the properties of UCoAl around the QCEP. Quite generally, it was shown that unusual properties arise if a metamagnetic transition is accompanied by a change in the Fermi surface topology (Lifshitz transition), as it is believed to occur at the QCEP in $ZrZn_2$, where unconventional universality is expected [102].
First, we discuss a possible analogy with the quantum critical metamagnet $Sr_3Ru_2O_7$, in which an exotic phase is observed, called *nematic* phase [103–105]. In analogy with the nematic state of liquid crystals, which has orientational but no positional order, it has been proposed that the electrons could form nematic liquids in the presence of strong correlations [106]. Such an electron nematic state is characterized by a lower rotational symmetry than the lattice symmetry. It was indeed observed in $Sr_3Ru_2O_7$ which has double-layered perovskite structure . In the case of UCoAl, the inversion symmetry is not present in the crystal structure, so the situation is more complicated.
The plateau between H_m and $H^\star$ may be related to the case of $CeRu_2Si_2$ (Rh-doped) where a plateau of A coefficient was observed, between the fields H_c and H_m. In that case the AF order disappears at H_c and the pseudo-metamagnetic transition occurs at H_m [107]. In-between, the system is in a PM state with strong AF fluctuations.This regime occurs only in the doped system, and it was suggested that in the pure compound the two anomalies are actually merged together, with both FM and AF critical fluctuations [108]. This picture may be considered for UCoAl if AF correlations were to be detected at $H = 0$. The susceptibility for $H \parallel c$-axis at zero pressure shows the characteristic broad peak at $T_\chi^{\max} \approx 20\,\mathrm{K}$. This is typical heavy fermion behaviour with AF correlations. Further studies with microscopic probes are required.
One could possibly think that H_m and $H^\star$ are two metamagnetic transitions, with a low-moment FM_1 phase in-between, like the FM_1 phase in UGe_2. The A coefficient also forms a plateau in this region of the phase diagram in UGe_2. Such a two-step metamagnetic transition will occur if there are two peaks in the DOS due to van Hove singularity [109, 110]. However, the magnetostriction under pressure, which is related to the magnetization ($\Delta V/V \propto M^2$ at first approximation), showed no anomaly at $H^\star$.

A frustration effect?

We finally propose a last scenario, considering this difference $\Delta\rho_{xx}$ between up and down sweep magnetoresistivity. It is a very peculiar phenomenon, observed only in the transverse sample, at low temperature, in the region of the T–P–H phase diagram where the QCEP is expected. We have no explanation for this phenomenon. Yet we may speculate that the vertical hysteresis resembles the memory effect of a spin glass state, which typically occurs in magnetically frustrated systems. It should be noted that the crystal structure of UCoAl forms a quasi-Kagome lattice of U atoms, thus magnetic frustration can potentially exist. When the CEP terminates at $T = 0$, a new phase due to the frustration — which is hidden by the first-order transition at H_m at low pressure — may start to appear. However, this raises the question of how frustration can be realized in an itinerant magnetic system.

5.3.6 Conclusion on the resistivity measurements on UCoAl

We carried out an extensive series of resistivity measurements on UCoAl, under magnetic field, high pressure, and low temperature, with a particularly sensitive instrumentation (cold transformers).

We studied the non-Fermi liquid behaviour along the transverse direction. We found two separate NFL regions: at low-pressure–low-field, due to the presence of spin fluctuations in the vicinity of the FM instability ; and another NFL region at 1.42 GPa. The A coefficient was finely mapped in the field–pressure phase diagram, and it is highly enhanced in the two critical regions: at low-pressure–low-field and around 1.42 GPa, in relation with the NFL behaviour.

The hysteresis between up and down field scans was determined precisely, indicating the collapse of the first-order metamagnetic transition at $P_\Delta \sim 2$ GPa. We observed striking differences between the longitudinal and transverse configurations. The variation of ρ_{xx} at H_m progressively changes sign at $P_M \approx 1.2$ GPa, where a plateau appears in the transverse residual resistivity, as already reported by F. Honda [79] and D. Aoki [76]. In addition, an intriguing difference in the transverse resistivity between up and down field sweeps was observed above P_M, suggesting an exotic phase emerging in the region of the QCEP. Its location in the phase diagram has been defined precisely, but the nature of this exotic phase is unknown.

5.4 Magnetization

5.4.1 Ambient pressure (relaxation effects)

Magnetization measurements are routinely performed as a sample characterization technique, using commercial SQUID extraction magnetometers (*MPMS, Quantum Design*) available at INAC. In principle, the sharpness of the metamagnetic transition is an aspect of the quality of a sample of UCoAl. Among the numerous samples which we have characterized, one of them showed an extraordinary sharp transition, with the magnetization undergoing a discontinuous jump whatever the field sweep rate. In this section we present magnetic measurements performed at our laboratory with an MPMS down to 2 K, as well as some complementary measurements down to 100 mK, performed with Carley Paulsen (Institut Néel, CNRS – Grenoble) on the same sample, with a home-made instrument (a dilution fridge mounted on an extraction SQUID magnetometer).

The sample was cone-shaped, cleaved out near the tail of the ingot. Single crystal and orientation was checked by X-ray Laue photograph. In the MPMS, the sample was glued with GE varnish onto a plastic foil inserted inside a plastic straw. For the experiment in dilution fridge, the sample was glued with GE varnish onto a copper plate, and thermal contact was provided by copper foil wrapped around the sample and Apiezon N-grease. The field was applied along the c-axis.

Magnetization versus field

Figure 5.25 shows M-H measurements at various temperatures from 0.1 K to 13 K. Points are taken every 5 Oe in the transition region, with a delay of $1'30''$ between two measurements. Below 10 K, we can see discontinuities at the transition, and a clear hysteresis between up and down sweeps. From these data we obtain the T-H phase diagram of UCoAl at zero pressure (Fig. 5.26). The hysteresis expands rapidly on cooling below ~ 2 K. The temperature of the critical endpoint is found at $T_0 = 10$ K.

Metamagnetic transition: relaxation effects

Actually, in the vicinity of H_m before the transition, the system is unstable, and it eventually transits spontaneously after some time. This transient regime could be observed in both directions : from PM to FM (relaxation «up») and from FM to PM (relaxation «down»). From now on, we distinguish the critical field for up-sweep (H_m^{inc}) and for down-sweep (H_m^{dec}). Figure 5.27 shows the details of the hysteresis at 2 K and indicates the unstable regions where the relaxation phenomena are observed.

In order to measure relaxation processes, the field was rapidly increased from 0 to $H \lesssim H_m^{\mathrm{inc}}$ in the case of up-sweeps, or rapidly decreased from ~ 2 T to $H \gtrsim H_m^{\mathrm{dec}}$ in the case of down-sweeps. The measurements were started after cooling the shunt in order to have the magnet in persistent mode ($\sim$ 15 s delay), or as soon as the field

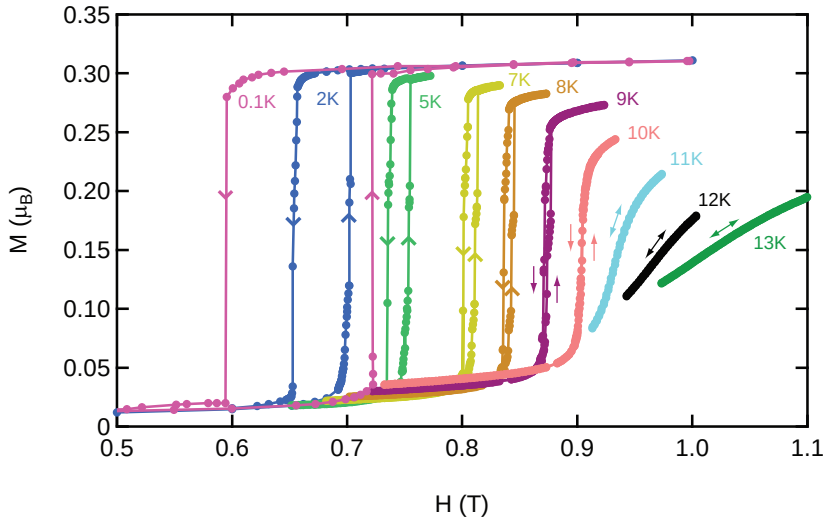

Figure 5.25: Magnetization as a function of applied field, with up and down sweeps. Colour labels indicate the temperature.

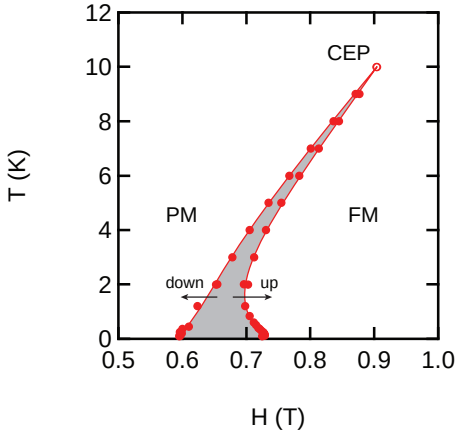

Figure 5.26: Temperature–field phase diagram of UCoAl, obtained from up and down M-H measurements of Fig. 5.25.

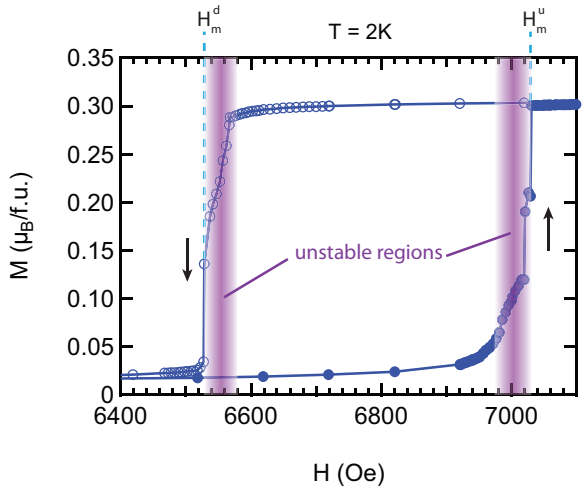

Figure 5.27: Details of the hysteresis in M vs H at 2 K. Coloured zones indicate the regions in which time effects could be observed. In this case, data points were measured every 1'30".

H was established (for short-time relaxation measurements). In any case the field was steady during the whole measurements. The results are independent of the magnet state (driven/persistent mode) and of the measuring rate (typical extraction time is 4 s, and the delay between points can be shrinked to arbitrary low value).

Figure 5.28 shows relaxation curves (up and down) at 2 K for different steady fields H. Time is plotted on a log scale. Relaxation curves $M(t)$ could be measured in a field range of about 50 Oe before $H_m^{\rm inc}$ and $H_m^{\rm dec}$, where the time scale of the relaxation ranges from a few seconds to a few hours.

The relaxation curves are not typical exponential decays. The magnetization relaxes step by step. We observe two rapid jumps of $\approx 0.08\,\mu_{\rm B}$ each, where the slope $\mathrm{d}M/\mathrm{d}t$ diverges. The last jump leads to the stable FM state with $M = 0.3\,\mu_{\rm B}$. Starting from different initial values, all $M(t)$ curves have the same steps at the same values of M, and they all finish in the same stable final state. Similar relaxation curves are observed up to 5 K, but over a gradually reduced field window.

During the experiment performed at CNRS with the dilution fridge, we measured relaxation curves at 100 mK, 500 mK, 1.2 K and 2 K. The data are similar to those obtained at INAC, but not identical. At 100 mK, the relaxation appears to be too slow to measure over reasonable time scales and we do not show the data here. The relaxation at 500 mK are shown in Figure 5.29. It is interesting to note that the points of inflection in the relaxation occur at a given value of magnetization which is temperature- and field-independent. We note that there are some strange problems with reproducibility. We observed step-like features in the relaxation at given values of magnetization in all applied fields. However, these features disappeared after the extractor was replaced (see

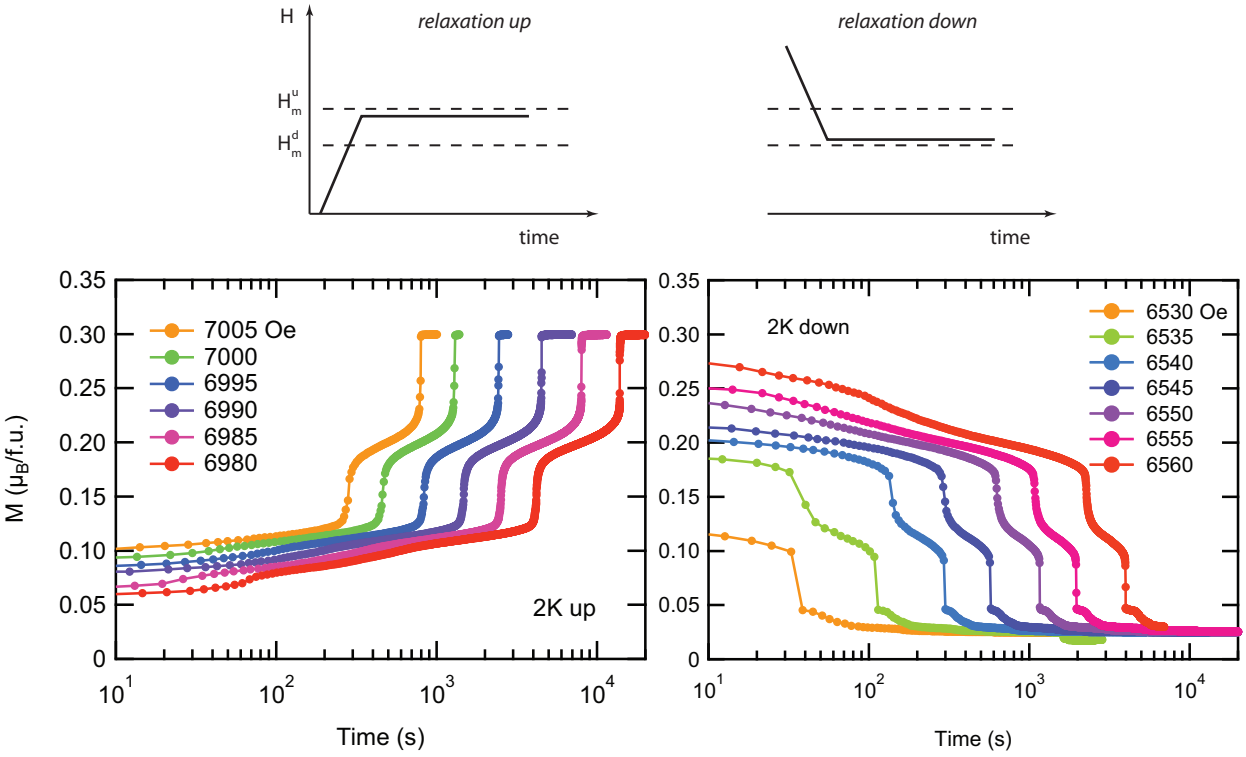

Figure 5.28: Magnetization as a function of time (log scale) at the various steady fields at 2 K. The field was rapidly increased (decreased) from 0 (2 T) to the steady value, for relaxation «up» and «down», respectively.

Fig. 5.29-b) and were not observed during the time that we took the 500 mK data shown in Fig. 5.29-a, despite many different measuring protocols being attempted so that to get the multiple step features back again. Eventually, after a few days of M vs T, the features returned again when measuring at 1.2 K etc. This indicates that the shape of the relaxation curves is highly sensitive to the sample environment, possibly through mechanical stress induced by the glue and sample holder.

Effect of field and pressure on the relaxation time

$M_H(t)$ curves taken at a given temperature and different fields are superimposable in a logarithmic time scale, which means that they only differ by a time scaling. Hence there are two aspects to consider:

- the shape of a relaxation curve, with plateaux and jumps
- the effect of field and temperature on the characteristic time of the relaxation curves

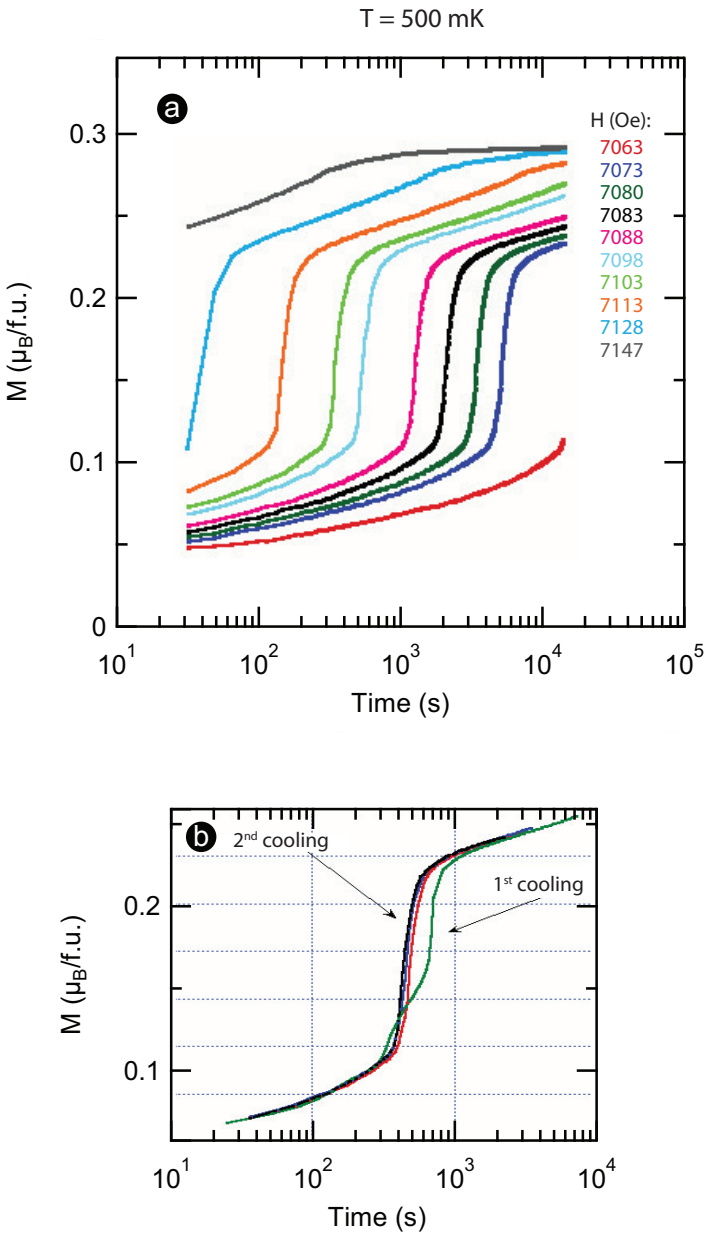

Figure 5.29: a) Magnetization as a function of time (relaxation up) at various steady fields at 500 mK. The sample was warmed to 1 K before regulating at 500 mK. b) Before and after the extractor has been replaced.

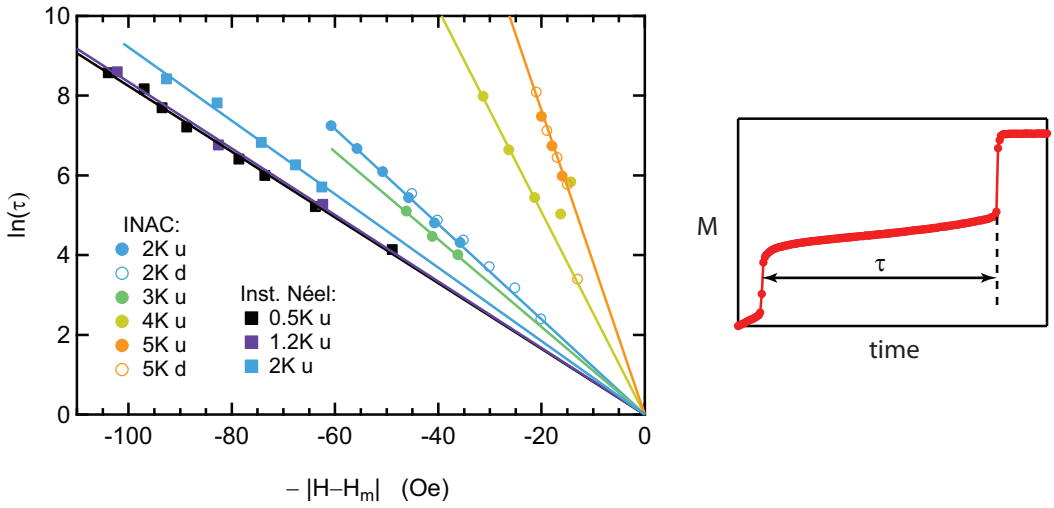

Figure 5.30: $\ln\tau$ vs $-|H-H_m|$ at various indicated temperature and field-sweep directions. Lines show the fit uing eqs. 5.4a and 5.4b.

For the latter, we propose a simple phenomenological description.

Since the relaxation curves measured in the dilution fridge cannot be fit to an exponential function, to infer a relaxation time we estimated the time it takes the magnetization to reach $(1-1/e)M_{\max}$. For the curves measured in the ^{4}He fridge (MPMS), we defined the characteristic time τ as the duration of the plateau between the two characteristic steps. In order to find a relation between τ and H, in Figure 5.30 we plot $\ln\tau$ against $(H-H_m^{\text{inc}})$ for up-relaxation, and $(H_m^{\text{dec}}-H)$ for down-relaxation, so that we have $-|H-H_m|$ as a common horizontal scale for up and down relaxation curves at various temperatures $(2,3,4,5\,\text{K})$. This plot yields the empirical relations:

$$\tau = \exp\left(-\frac{H-H_m^{\text{inc}}}{h}\right) \quad \text{for relaxation up} \tag{5.4a}$$

$$\tau = \exp\left(-\frac{H_m^{\text{dec}}-H}{h}\right) \quad \text{for relaxation down} \tag{5.4b}$$

where τ is expressed in seconds. The constant h is the same for up and down relaxation, but decreases with increasing temperature. It therefore defines $H_m^{\text{inc,dec}}$ as the field at which the characteristic relaxation time $\tau = 1\,\text{second}$ is too short to observe relaxation effects experimentally.

From equations 5.4a and 5.4b, we can derive the scaling relation between two time constants τ taken at different fields H and $H' = H - \Delta H$:

$$\tau(H-\Delta H) = \mathrm{e}^{\Delta H/h}\tau(H) \tag{5.5}$$

where $\Delta H > 0$ ($\Delta H < 0$) for relaxation *up* (resp. *down*). The constant h has the dimension of a field, and it is the characteristic width of the unstable region, such that: $\tau(H_m^{\rm inc} - 0h) = 1\,{\rm s}$; $\tau(H_m^{\rm inc} - 4h) \approx 1\,{\rm min}$; $\tau(H_m^{\rm inc} - 8h) \approx 1\,{\rm hour}$ [8]. In a simple picture, the field window within which relaxation curves are measureable in a reasonable time is $\Delta H^{\rm obs} = 4h$. This field window reduces with temperature: from $\Delta H^{\rm obs} \sim 50\,{\rm Oe}$ at 500 mK to only $\sim 10\,{\rm Oe}$ at 5 K.

We already noted that relaxation curves $M(t)$ at a given temperature only differ by their time scale. The farther from H_m, the slower the relaxation. We can therefore write the relation between two relaxation curves taken at H and $H' = H - \Delta H$:

$$M_{H-\Delta H}(t) = M_H\left(t{\rm e}^{-\Delta H/h}\right) \tag{5.6}$$

and in a log time scale, they are just shifted horizontally:

$$M_{H-\Delta H}(\ln t) = M_H\left(\ln t - \frac{\Delta H}{h}\right) \tag{5.7}$$

The external field actually tunes the speed of the relaxation.

Interpretation of the relaxation effects

These magnetic relaxation effects are very unusual. To our knowledge, such relaxation curves have never been observed in materials more or less related to our topic [9]. So far, we found no explanation for these phenomena. We put forward 3 possible mechanisms that could be relevant in the context of UCoAl:

i) A percolation mechanism. Clusters of FM phase nucleate throughout the sample, and grow up independently. When a critical density is reached, the multitude of independent clusters merge into a single entity. This critical point is a singularity, in the sense that the delocalized spin-polarized electrons suddenly escape from microscopic confinement (cluster-size) to the infinite lattice, producing a sudden Fermi surface reconstruction. This picture could explain the diverging $\partial M/\partial t$ that occurs in the relaxation curves.

ii) Lattice strain relaxation : this invokes the magnetostriction as a source of irreversibility responsible for the simultaneous onset of ferromagnetism within the basal plane and between the planes. There is a strong magnetostriction accompanying the metamagnetic transition in UCoAl. As a consequence, when a part of the sample becomes ferromagnetic, a strain field forms at the boundaries, which stands as a potential barrier separating the two states of the system. In phase space, the system has to overcome this potential in order to go from one state to the other. This is the direct

[8] This is for relaxation-up ; for relaxation-down, one should consider $(H_m^{\rm dec} + 4h)$, $(H_m^{\rm dec} + 8h)$ ...

[9] The steps in the relaxation curves may look like the case of some single molecule magnets [111, 112], but these are completely different systems

manifestation of the first-order nature of the transition, giving rise to a hysteresis. In real space, when the field is close to but below H_m, pockets of FM phase nucleate by thermal activation over the potential barrier Δ with a probability $\tau^{-1} = \exp \frac{\Delta - \mu B}{k_B T}$. This is consistent with the exponential increase of the hysteresis with decreasing temperature observed in magnetization (Fig 5.26) and in resistivity (Fig. 5.23). At low temperature, the relaxation becomes extremely fast (we observe a discontinuous jump at 100 mK), as if the band splitting between spin-up / spin-down was occuring simultaneously in the whole sample.

iii) A spin glass state: The existence of AF interactions — if any — would give rise to frustration on the quasi-Kagome lattice of U atoms, and may thus produce relaxation effects. This possibility was also put forward in Section 5.3.5 to explain the peculiar difference between up and down field sweep in the transverse magnetoresistance.

5.4.2 Magnetization under pressure

We performed magnetization measurements of UCoAl under pressure with a non-magnetic pressure cell (Cu-Ti alloy) which fits in a commercial SQUID magnetometer (MPMS, *Quantum Design*). This pressure cell is based on the model developped by Kobayashi *et al.* [32] and Tateiwa *et al.* [33], and modifed by Yusei Shimizu in 2009 at Hokkaido University. We used Daphne oil 7373 as a pressure transmitting medium. The sample was a single crystal oriented along the c-axis, and cut into hexagonal shape in order to optimize the sample space. Pressure was determined from the superconducting transition of Pb. The background — mainly due to the NiCrAl gasket — was measured independently and substracted from the data.

In Fig. 5.31-a we present M-H magnetization curves of UCoAl along the c-axis, at $2K$, for various pressures up to 1.8 GPa. Pressure shifts the transition to higher fields, as expected. We can track the transition up to 5.5 T, which is the limit of our magnetometer. The magnetization in the FM state slowly decreases with pressure. But pressure has no effect on the slope $\mathrm{d}M/\mathrm{d}H$, neither in the PM or FM state. The transition anormaly broadens with pressure: from 0.25 T at zero pressure to 0.7 T at 0.7 GPa and 1 T at 1.3 GPa. At 1.8 GPa, the end of the transition is beyond the limit of the magnet. The pressure dependence of H_m (taken as the middle of the transition) is plotted in Fig. 5.31-b along with the values obtained by other measurements. Our magnetization measurements are not in agreement with the other probes : there is a lower pressure dependence, which is comparable to the magnetization data reported by Mushnikov *et al.*. There is definitely a problem with magnetization measurements under pressure. The probable reason is the very high sensitivity of UCoAl to non-hydrostaticity.

We tried to improve the pressure conditions by reducing the size of the sample, by using different gaskets, without notable improvement. Attemps to improve the hydrostaticity by using liquid Argon as a pressure transmitting medium failed, as we did not succeed to obtain any pressure (Ar was probably not successfully trapped in the pressure chamber).

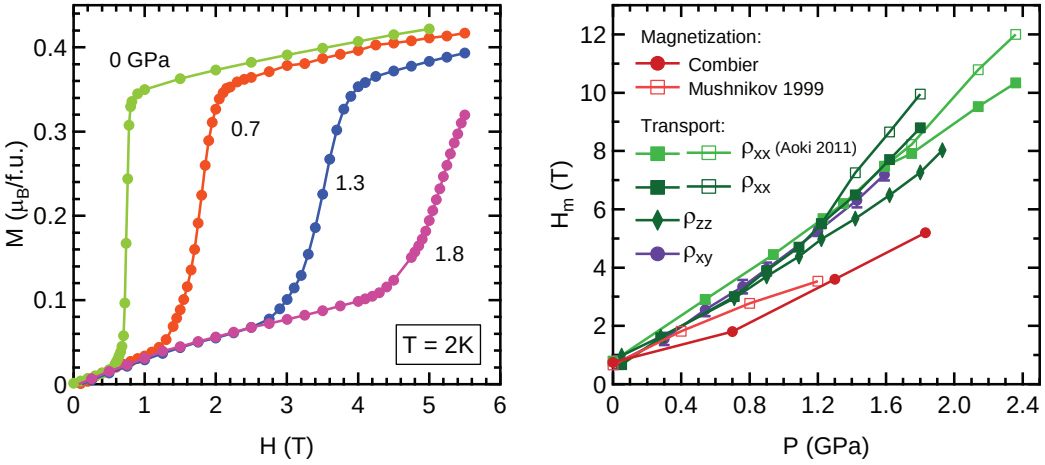

Figure 5.31: a) Magnetization of UCoAl at 2 K at various pressures, measured in a SQUID magnetometer. b) Pressure dependence of H_m measured with various probes. Resistivity data was reported in [76] and magnetization data is taken from [75].

5.5 X-ray Magnetic Circular Dichroism

The degree of delocalization of the $5f$ electrons governs the magnetic properties of Uranium intermetallics. The metamagnetism in UCoAl is usually considered in a itinerant picture (band metamagnetism). The strong spin-orbit coupling in the $5f$ states induces a sizeable orbital moment which is comparable and antiparallel to the spin moment. The ratio of orbital-to-spin moments provides information on the degree of delocalization of the $5f$ electrons [113]. In many U compounds (URhAl, UIrAl, UPtAl, etc.) this ratio is reduced (≈ -2) compared to the free ion values (-3.42 and -2.57 for $5f^2$ and $5f^3$ configurations, respectively). Furthermore, the individual values of μ_L and μ_S of the $5f$ orbitals are key parameters to understand the metamagnetic behaviour of UCoAl. These microscopic properties can be adressed by X-ray magnetic circular dichroism (XMCD) measurements.

We performed an XMCD experiment at the European Synchrotron Radiation Facility (beamline ID12), in collaboration with Alexandra Palacio Morales, Andrei Rogalev and Fabrice Wilhelm. The motivation was to measure the orbital and spin part of the magnetization in order to compare with band structure calculations and polarized neutron diffraction experiments, and to see whether there is a change of the orbital-to-spin moment ratio between the PM and FM state of UCoAl on the U site. In addition, Co- and U-specific magnetization measurements may address the question of whether the Co holds an intrinsic or an induced moment.

In the past, XMCD experiments had been performed at the $M_{4,5}$ absorption edges of Uranium on a polished crystal, at $\sim$ 10 K, between 0.7-7 T. The authors could not

conclude about the question of a change in μ_L/μ_S. We repeated the measurements at the U $M_{4,5}$-edges, with improved experimental conditions: lower temperature $T = 2\,\mathrm{K}$, more extended field range $H = 0.5, 1, 17\,\mathrm{T}$, higher surface quality (cleaved sample), and a high quality sample of UCoAl (sharper metamagnetic transition). We also measured the XMCD signal of UCoAl at the Cobalt K-edge, which, to our knowledge, have never been reported before.
In this section, we introduce the principle of the XMCD technique, and how we can retrieve the orbital and spin moments by applying sum rules. We then present our results and compare with reported XMCD experiments. We also relate our results with neutron and NMR experiments reported in the literature [22, 77, 81].

5.5.1 Principle

X-ray magnetic circular dichroism (XMCD) is a spectroscopic technique that utilizes circularly polarized X-rays from a synchrotron source to obtain information on the microscopic magnetic properties of a material. It is sensitive to the spin and orbital magnetic moments of an absorbing atom. By definition, XMCD is the difference of absorption spectrum (dichroism) between left and right circularly polarized photons. It is essentially an *element-specific* and *orbital-selective* magnetometry tool, which is particularly adapted for the study of $3d$, $4d$, $5d$ transition metals, rare earths and actinides.

X-ray absorption is proportional to the density of *unoccupied* states (DOS above the Fermi level), with different absorption cross-sections (α^+, α^-) according to the helicity of the photons — parallel or antiparallel to the projection of the spin or orbital angular momentum μ_s, μ_l of the electrons (which are decided by the field direction). The XMCD signal is written as:

$$\Delta\alpha = \alpha^+ - \alpha^- \tag{5.8}$$

At a given absorption edge, XMCD is sensitive to the *difference* of the spin ↑/spin↓ DOS above the Fermi level. The uranium $M_{4,5}$ absorption edges correspond to excitations of $3d$ electrons to the $5f$ states [10]:

$$\begin{aligned} \mathrm{U}M_4: &\quad 3d_{3/2} \rightarrow 5f_{5/2} \\ \mathrm{U}M_5: &\quad 3d_{5/2} \rightarrow 5f_{7/2,(5/2)} \end{aligned}$$

Left or right handed photons transfer their angular momentum to the excited photoelectrons, and the destination empty states act as a detector for this angular momentum. Since the initial state is known, and the transfered angular momentum as well, the XMCD

[10] There is a little branching $3d_{5/2} \rightarrow 5f_{5/2}$ at the U M_5 edge, which cannot be neglected.

at the U $M_{4,5}$ is sensitive to the difference between the $5f$ spin $\uparrow$/spin$\downarrow$ DOS above the Fermi level.

5.5.2 Sum rules

From the absorption and XMCD spectra of a pair of spin-orbit split core levels, we can extract microscopic information on the *ground state* of an atom. For this purpose, Thole, Carra et co-workers established a set of sum rules [114, 115]. They relate the integrated intensities of the isotropic absorption spectra (referred to as XANES: *X-ray absorption near-edge spectroscopy*) ($I_{M_{4,5}}$) and XMCD ($\Delta I_{M_{4,5}}$), to:

- the angular part of the spin-orbit splitting of the $5f$ valence shell
- the orbital moment
- the spin moment

These sum rules were derived within an atomic model. When applied to solids, some input parameters are required (the number of valence electrons and the spin-orbit coupling scheme) thus adding some uncertainty to the results.

First sum rule: angular part of the spin-orbit coupling

The first sum rule is used to get the number of spin-orbit split $5f_{5/2}$ and $5f_{7/2}$ empty states. The simple idea is that the ratio of integrated intensities of the XANES ($I_{M_{4,5}}$), called *branching ratio*, reflects the ratio of $5f_{5/2}$ and $5f_{7/2}$ empty states.

Formally, the branching ratio is related to the average value of the spin-orbit interaction in the $5f$ states:

$$\left\langle \vec{l} \cdot \vec{s} \right\rangle = -\frac{15}{4} n_{\mathrm{h}}^{5f} \left(\frac{I_{M_5}}{I_{M_5} + I_{M_4}} - \frac{3}{5} \right) + \frac{3}{2} n_{\mathrm{h}}^{5f} \cdot \Delta \tag{5.9}$$

which, in turn, is related to the occupation number of $5f_{5/2}$ and $5f_{7/2}$ states:

$$\left\langle \vec{l} \cdot \vec{s} \right\rangle = \frac{3}{2} n_{7/2} - 2 n_{5/2} \tag{5.10}$$

$$14 - n_{\mathrm{h}}^{5f} = n_{7/2} + n_{5/2} \tag{5.11}$$

$$\tag{5.12}$$

The second term in eq. 5.9 is a correction which takes into account the overlap of XANES spectra. When $\left\langle \vec{l} \cdot \vec{s} \right\rangle$ is large, this term is vanishing. From the system of equations {5.10,5.11} we can obtain $n_{7/2}$ and $n_{7/2}$ if we know the number of valence electrons.

Second sum rule: orbital moment

From the integrated intensities of the XANES ($I_{M_{4,5}}$) and XMCD ($\Delta I_{M_{4,5}}$) spectra, it is possible to extract the orbital part of the magnetic moment $\mu_L = -\langle L_z \rangle \mu_\mathrm{B}$ using the relation:

$$\langle L_z \rangle = n_\mathrm{h}^{5f} \frac{\Delta I_{M_5} + \Delta I_{M_4}}{I_{M_5} + I_{M_4}} \tag{5.13}$$

Third sum rule: spin moment

The determination of the spin part of the magnetic moment $\mu_S = -2\langle S_z \rangle \mu_\mathrm{B}$ is less straightforward, because we have access to an *effective* spin moment of the $5f$ orbitals:

$$\mu_S^\mathrm{eff} = -2 \left\langle S_z^\mathrm{eff} \right\rangle \mu_\mathrm{B} \tag{5.14}$$

which is obtained from combined analysis of XMCD and XANES spectra:

$$2 \left\langle S_z^\mathrm{eff} \right\rangle = n_\mathrm{h} \frac{\Delta I_{M_5} - \frac{3}{2} \Delta I_{M_4}}{I_{M_5} + I_{M_4}} \tag{5.15}$$

μ_S is hidden by the so-called *dipolar magnetic term*:

$$\mu_S^\mathrm{eff} = \mu_S + \mu_\mathrm{DM} = -2 \langle S_z \rangle \mu_\mathrm{B} - 6 \langle T_z \rangle \mu_\mathrm{B} \tag{5.16}$$

where T_z is the *intra-atomic magnetic dipole operator*, which measures the anisotropy of the spin distribution (due to the anisotropy of charge) in a shell. It depends on the spin-orbit coupling and on the crystal field. The difficulty is that there is no way to experimentally determine $\langle T_z \rangle$ unambiguously. There are, however, some theoretical calculations of $\langle T_z \rangle$ for three spin-orbit *coupling schemes* [116]: LS (Russel-Saunders), JJ, and *intermediate coupling* (IC). Uranium corresponds to the IC scheme.

5.5.3 Experimental details

The sample was a single-crystal with a cleaved surface perpendicular to the c-direction, and it was glued onto a Cu plate mounted on the cold finger. The temperature of the sample was 2 K during the whole experiment.

XMCD measurements have been performed at the U M_4 (3.728 keV) and M_5 (3.552 keV) edges, and at the Co K edge (7.709 keV) (values given in the tables [117]), at 3 different fields (0.5, 1, 17 T). Energy scans were performed with left and right handed polarizations, and for positive and negative field in order to remove the residual contribution, thus eliminating the possible experimental bias coming from linear dichroism. We shall thus

refer to *parallel (antiparallel) scan* when the photons polarization is parallel (antiparallel) to the applied field. XANES and XMCD are therefore obtained from the parallel ($\parallel$) and antiparallel ($\nparallel$) scans averaged over positve and negative field, as follows:

$$\mathrm{XANES}_{\parallel} = \frac{1}{2}\left(\mathrm{scan}_{\parallel}^{\mathrm{pos}} + \mathrm{scan}_{\parallel}^{\mathrm{neg}}\right) \tag{5.17}$$

$$\mathrm{XANES}_{\nparallel} = \frac{1}{2}\left(\mathrm{scan}_{\nparallel}^{\mathrm{pos}} + \mathrm{scan}_{\nparallel}^{\mathrm{neg}}\right) \tag{5.18}$$

$$\mathrm{XANES}_{\mathrm{iso}} = \frac{1}{2}\left(\mathrm{XANES}_{\parallel} + \mathrm{XANES}_{\nparallel}\right) \tag{5.19}$$

$$\mathrm{XMCD} = \frac{1}{2}\left(\mathrm{XANES}_{\parallel} - \mathrm{XANES}_{\nparallel}\right) \tag{5.20}$$

$$\tag{5.21}$$

The measurements were typically repeated 10 times (20 times at 0.5 T) at every edge and every field value.

5.5.4 Results

U $M_{4,5}$-edges

The XANES were corrected for self-absorption and the edge jumps were normalized by the degeneracy of initial states: between $[0, 1]$ for U M_5, and between $[1, 5/3]$ for U-M_4.

Figure 5.32 shows XANES spectra (left- and right-hand polarization, and isotropic) and XMCD spectra at the U $M_{4,5}$ edges. XMCD is shown for $H = 0.5, 1, 17\,\mathrm{T}$, while XANES is shown only at 17 T since the isotropic XANES has negligible field dependence. The data at 0.5 T correspond to the paramagnetic state, and $1\,\mathrm{T}, 17\,\mathrm{T}$ to the FM state. The XANES of different helicities cannot be distinguished at U-M_5, but are clearly visible at the U-M_4 edge.

The XANES at U-$M_{4,5}$ edges are typical absorption spectra, consisting of a resonance peak (called *white line*) on top of a step-like edge jump. In order to integrate the peak intensities (shaded area on the graph), the edge jump was accounted for by an arctan function.

At U-M_4, there is a rather large negative XMCD peak, with symmetrical shape, whereas the XMCD at U-M_5 is comparatively much smaller, and it has an asymmetrical S-shape with a negative part and a smaller positive part. At first look, these spectral shapes agree with the reported XMCD experiments at U-$M_{4,5}$ [59] and U-$N_{4,5}$ [118] on UCoAl.

However, the low-field XMCD signals are small, and require a closer look. In Figure 5.33 the XMCD spectra are scaled and superimposed to one another.

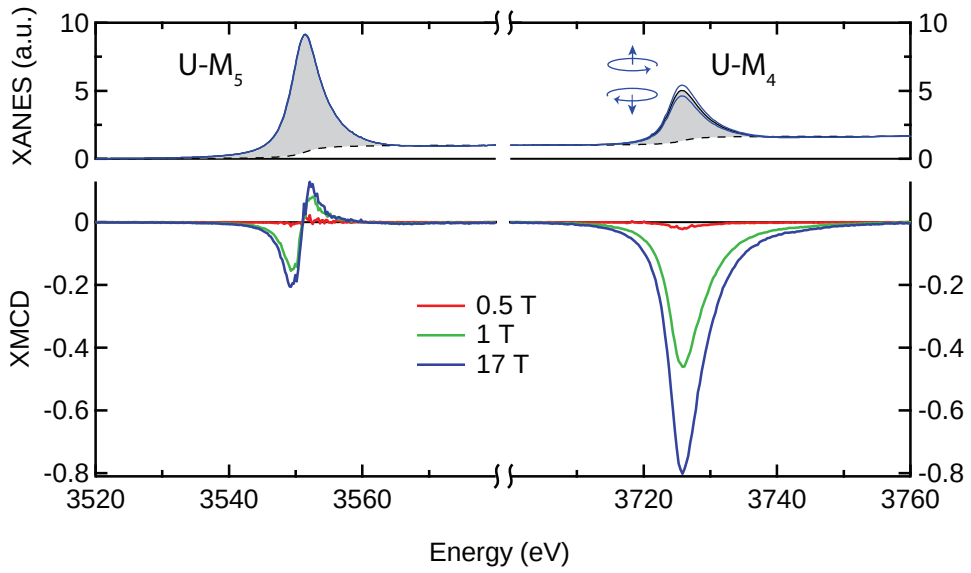

Figure 5.32: XANES and XMCD spectra at the U $M_{4,5}$ edges, at various fields $(0.5, 1, 17\,\mathrm{T})$. The shaded areas represent the integral of the XANES peaks. Absorption spectra are shown at 17 T only, for both polarizations. XMCD and XANES are given in the same arbitrary units.

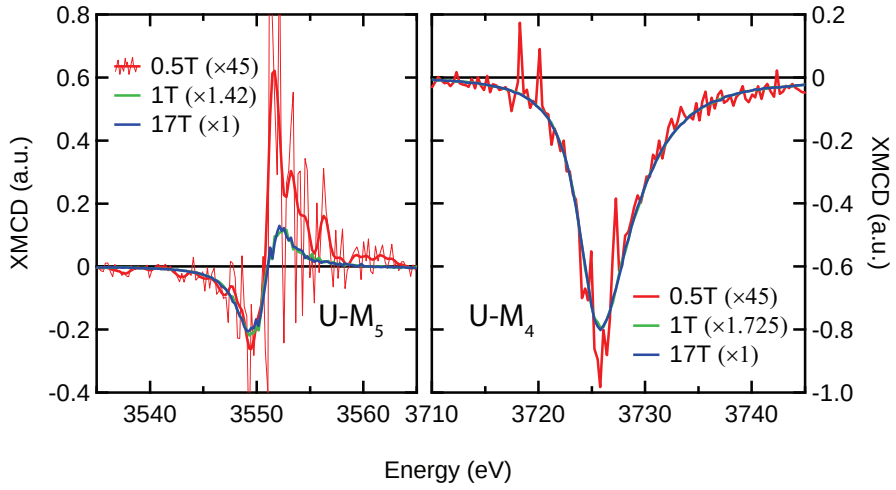

Figure 5.33: XMCD spectra at the U $M_{4,5}$ edges, at various fields $(0.5, 1, 17\,\mathrm{T})$, scaled to match the 17 T spectra. The 1 T and 17 T spectra can be hardly distinguished in the M_4 edge. In addition, we show a smoothed curve of the U-M_5 spectrum at 0.5 T for better reading.

- U-M_4: Perfect matching is achieved at all fields with $\Delta\alpha_{0.5\,\mathrm{T}}/\Delta\alpha_{17\,\mathrm{T}} = 45$ and $\Delta\alpha_{1\,\mathrm{T}}/\Delta\alpha_{17\,\mathrm{T}} = 1.725$.
- U-M_5: the XMCD spectra at 1 T and 17 T can be superimposed with a ratio $\Delta\alpha_{1\,\mathrm{T}}/\Delta\alpha_{17\,\mathrm{T}} = 1.42$ which is different than at U-M_4. But the 0.5 T spectrum cannot be satisfactorily superimposed to the others, despite the tolerance allowed by the relatively large standard deviation of the data points. Eventually, the negative part can be superimposed to the other spectra with a ratio $\Delta\alpha_{0.5\,\mathrm{T}}/\Delta\alpha_{17\,\mathrm{T}} = 45$ as at U-M_4, but then the positive part is ~ 2 times larger.

Van der Laan *et al.* have predicted that the shape of the XMCD spectra at the U N_5 and M_5 edges is sensitive to the number of valence electrons in the U atom [119]. However, because of the weak signal, the spectral shape of the U-M_5 XMCD at 0.5 T should be considered with precautions, especially since different spectral shapes were observed in the reported experiments:

- At the same U M_5-edge, the XMCD signal was found to have no positive part at low field (0.7 T) [59].
- In the soft X-rays, all XMCD spectra at U N_5-edge could be superimposable [118] (no change of spectral shape).

As a conclusion, we can hardly confirm or infirm a possible valence change at the metamagnetic transition in UCoAl, owing to the important variability of the XMCD spectral shape at low field among the various experiments.

From the second and third sum rules (eqs. 5.13 and 5.15), we have $\Delta I_{M_4} \propto \langle L_z \rangle - 2\left\langle S_z^{\mathrm{eff}} \right\rangle$ and $\Delta I_{M_5} \propto \langle L_z \rangle + 4\left\langle S_z^{\mathrm{eff}} \right\rangle/3$. At U-$M_4$, the large negative symmetrical XMCD means that μ_L and μ_S^{eff} contributions add up. At U-M_5, the small S-shape XMCD indicates that their contributions almost cancel out.

From these simple observations, it already appears that μ_L and μ_S^{eff} are antiparallel, with $\mu_L/\mu_S^{\mathrm{eff}} \sim -2$. Precise determination of these values will be discussed in Section 5.5.5.

In Figure 5.34 we plot the field dependence of the maxima of XMCD signal at U $M_{4,5}$-edges, and we compare with the data of Ref. [59]. The amplitudes of the U-$M_{4,5}$ XANES peaks (corrected for self-absorption and normalized to edge jump) are similar, but in our experiment the XMCD signal is quite larger : ~ 1.5 times larger at U-M_4, and 2-3 times larger at U M_5-edge.

Co K-edge

The Cobalt K-edge corresponds to the transitions $1s \rightarrow 4p$. Since there is no spin-orbit splitting of the starting levels, XMCD only measures the orbital moment of the $4p$ electrons.

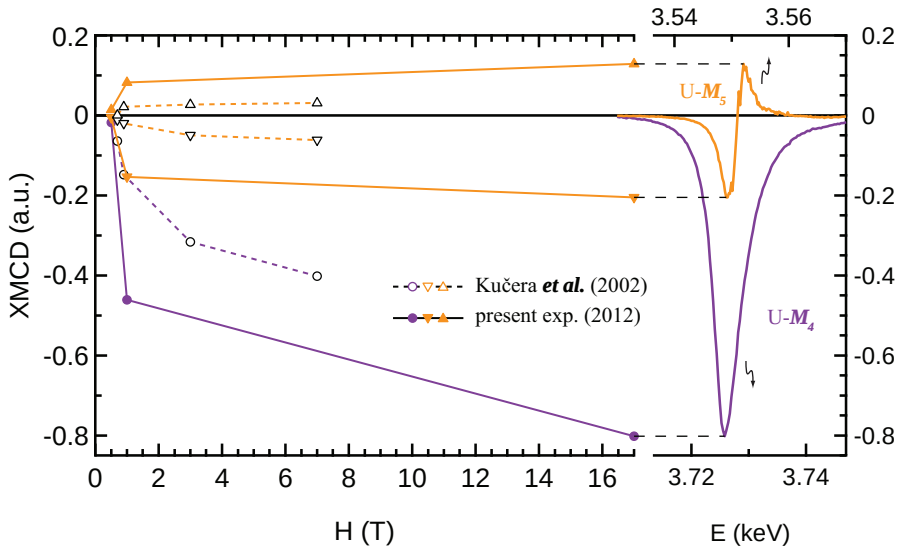

Figure 5.34: Field evolution of the XMCD extrema at the U $M_{4,5}$ edges, and comparison with values of ref. [59]. XMCD spectra at 17 T are shown on the right hand side as a reference.

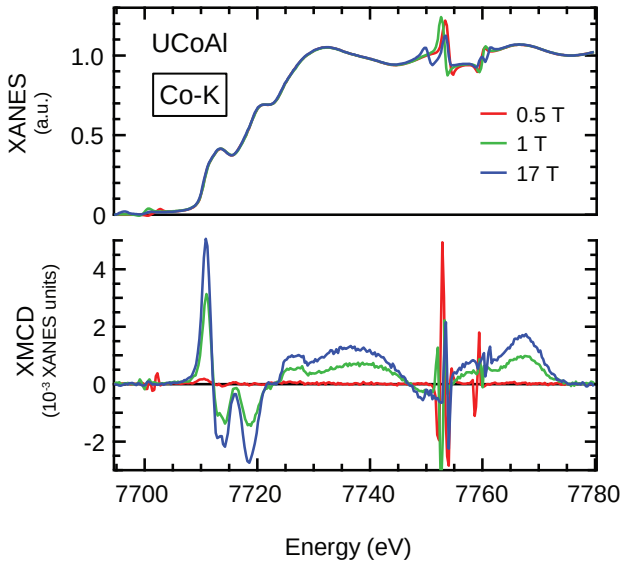

Figure 5.35: XANES and XMCD spectra at the Co K-edge, at $H = 0.5, 1, 17$ T.

XANES and XMCD at the Co K-edge are presented in Fig. 5.35. Measurements were performed at 0.5, 1, and 17 T. Only isotropic XANES are shown since left and right polarizations would not be distinguished on the graph. The XMCD signal is indeed very small (XMCD/XANES $\sim 10^{-3}$ at 17 T). Since $4p$ states are in the conduction electrons continuum, there is no white line peak on top of the Co K XANES edge jump, and it is very difficult to apply sum rules. The structures above ~ 7730 eV are resonances ascribed to the local environment of the Co atoms, but the study of this so-called *EXAFS* (Extended X-ray Absorption Fine Structure) outreaches the scope of our experiment. Around 7752 eV and 7760 eV, there are non-reproducible features that are due to diffraction peaks.

In the XMCD spectra, the sharp positive and negative peaks around 7710-7715 eV are dominant, and do not exist in Co metal. They are known to originate from a large spin-orbit coupling with U orbitals [11], so it indicates that the Co moment is mostly induced by the U. These induced peaks can be used to detect a change of the hybridization between U-5f and Co-4d bands, by following the evolution of the peak signal with field.

Element-specific magnetization

Co-specific magnetization curve M-H was obtained by measuring XMCD at a fixed photon energy $h\nu = 7710.9$ eV, corresponding to the maximum of the positive peak which originates from Co($4p$)-U($5f$) hybridization. The field was increased step by step along a loop pathway $H = 0 \rightarrow +17\,\mathrm{T} \rightarrow -17\,\mathrm{T} \rightarrow 0$, and the signal was recorded for the two different beam polarizations at every field value. The dichroism was separated from the residual contribution by averaging over positive and negative fields. Similarly, U-specific M-H curve was obtained at fixed energy $h\nu = 3725.8$ eV corresponding to the maximum of XMCD signal at U M_4-edge.
Results are presented in Figure 5.36, in which the Co- and U- specific magnetizations are compared with the bulk magnetization of UCoAl measured with a SQUID magnetometer. [12] The residual contributions are also plotted, showing no field dependence.
Both U and Co magnetizations show a sharp step-like increase at H_m. The U curve almost perfectly scales with the bulk magnetization, following the same negative curvature above H_m, while the Co magnetization has no curvature. The difference is small, thus the proportion of U moment induced on the Co is quite constant. A possible interpretation for the absence of curvature in the Co magnetization is that the Pauli paramagnetism is

[11] A. Rogalev and F. Wilhelm (private discussions)

[12] Some precision about the bulk magnetization data in Fig. 5.36: Since we do not have magnetization data at high field for this sample, the data shown in the main graph was measured at 90 mK on a different sample. Nevertheless, we checked that both samples have exactly the same magnetization profile above H_m, and we can see in Fig. 5.25 that there is no difference in the magnetization between 0.1 K and 2 K in the FM state. Differences only appear at the metamagnetic transition, where the critical field and hysteresis width are sample- and temperature- dependent. This is why the bulk magnetization in the inset of Fig. 5.36 was measured at 2 K, on the same sample as the XMCD data.

non-negligible compared to the U-induced polarization, thus adding a significant linear contribution. That the Pauli paramagnetism is visible would imply a very small Co moment, which is indeed consistent with NMR and neutron diffraction results [22,77,81]. In the reported soft-XMCD experiment [118], the authors compared the field dependence of the XMCD signal at the U N_5 and Co L_2 edges. They found a different magnetization profile on U and Co, but their result might be biased by the overlap of Co L_2 with U N_4 edge.
In the inset of Fig. 5.36, we see the details of the metamagnetic transition with up and down sweeps, compared with bulk magnetization at 2 K. Nominal temperature of the XMCD experiment was 2 K. The transition is as sharp as the bulk magnetization in up-sweep curves (< 150 Oe), but broader in down-sweeps (~ 300 Oe). The shape of the transition may be affected by the sample environment: for the XMCD experiment, the sample was strongly maintained by GE varnish inside a cavity in the Cu plate, and may thus experience stress.

The up-sweep critical field is similar for both XMCD signals and almost matches (~ 100 Oe higher) with the bulk magnetization. On the contrary, down-sweep critical fields are quite different, with a larger hysteresis of the U M_4 XMCD signal and a smaller hysteresis at Co K-edge as compared to the bulk magnetization.

The ~ 2 times smaller hysteresis in Co than in U could be ascribed to a discrepancy between the nominal temperature of the XMCD experiment (2 K) and the temperature of the sample under X-ray irradiation. Indeed, the transition in the Co signal resembles the bulk magnetization at ~ 3 K (see Fig. 5.25). The higher luminosity of the beam at the Co K-edge could explain a higher sample temperature. But in any case the sample heating is very limited and does not impact the results at higher field. Beside a possible experimental bias, these hysteresis curves would otherwise mean that Co demagnetizes first. This would be again another aspect of the peculiar properties of UCoAl observed in magnetic relaxation effects and resistivity measurements.

5.5.5 Analysis

In this section we present the sum rule analysis of the U $M_{4,5}$ spectra.
All sum rules require the number of $5f$ holes as an input, which is unknown. We thus consider the two atomic cases for the U electronic configuration: $5f^3$ (U^{3+}) and $5f^2$ (U^{4+}), and we get $n_{\mathrm{h}}^{5f} = 14 - n_{\mathrm{e}^-}^{5f} = 11$ and 12, respectively.
First sum rule involves the branching ratio $\mathrm{BR} = \frac{I_{M_5}}{I_{M_5}+I_{M_4}}$, which is determined experimentally, and is field-independent:

$$\mathrm{BR} = 0.698$$

Solving eqs. {5.10,5.11} for the two electronic configurations leads:

with values of the correction Δ taken from the literature [120]. The $5f^2$ configuration leads to non-physical values of $n_{7/2}$ and $n_{5/2}$. Nevertheless, our results confirm that

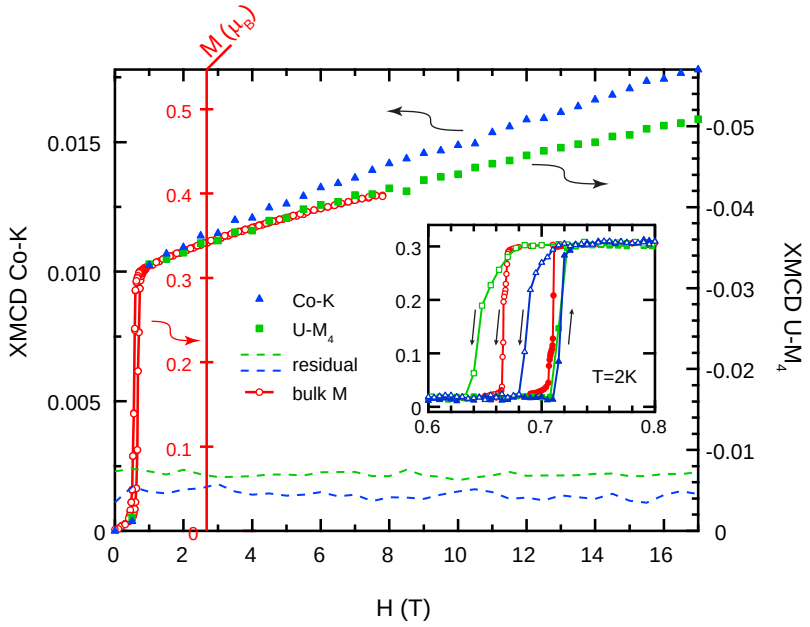

Figure 5.36: Magnetization of Cobalt at K-edge (left axis) and of Uranium at M_4-edge (right axis) ; residual contributions ; and bulk magnetization of UCoAl (free axis). Inset shows the details of the hysteresis between up and down sweeps at the metamagnetic transition, with bulk magnetization of the same sample at 2 K.

	$5f^2$	$5f^3$	
$n_{7/2}$	-0.22	0.49	($\Delta = 0.010$)
$n_{5/2}$	2.22	2.51	($\Delta = 0.014$)

the $5f$ electrons are mostly in the $J = 5/2$ configuration (antiparallel orbital and spin moments).
Second and third sum rules (Eqs. 5.13 and 5.15) yield the orbital moment μ_L and the effective spin moment μ_S^{eff}, which we determine for the two electronic configurations $5f^2$ and $5f^3$.
The spin moment μ_S can be determined from the effective spin moment μ_S^{eff} using theoretical values of the dipolar magnetic term μ_{DM}, as shown in eq. 5.16. Table 5.1 lists the theoretical values of μ_{DM}/μ_S in the intermediate coupling scheme, with $5f^2$ and $5f^3$ configurations:

Table 5.1: Theoretical values of μ_{DM}/μ_S in the intermediate coupling scheme (IC)

	$5f^2$	$5f^3$
μ_{DM}/μ_S	3.48	1.85

Alternatively, the spin moment μ_S can be determined independently of μ_S^{eff}, by considering that the magnetic moment is entirely carried by the U $5f$ orbitals:

$$\mu_{\text{bulk}} = \mu_L + \mu_S \tag{5.22}$$

Results are summarized in Table 5.2, at $H = 0.5, 1, 17\,\text{T}$, for the 2 electronic configurations $5f^2$ and $5f^3$.

In the first part of the table we show μ_L, μ_S^{eff}, and μ_L/μ_S^{eff} obtained from sum rules. The ratio μ_L/μ_S^{eff} changes from -0.55 in the PM state to ≈-0.75 in the FM state, and it is independent of the number of $5f$ electrons since it only results from the XMCD spectra and does not involve any external parameter.
In the second part, we used the bulk magnetization μ_{bulk} as an input to derive μ_S, μ_L/μ_S, and μ_{DM}/μ_S. In the PM state, bulk measurements performed on the same sample with two different magnetometers yielded $\mu_{\text{bulk}}(0.5\,\text{T}) = 0.12\,\mu_\text{B}$ and $0.16\,\mu_\text{B}$. This deviation is comparable to $|\mu_S|$ and thus undermines the ratios μ_L/μ_S and μ_{DM}/μ_S at 0.5 T. In the FM state, the error in the bulk magnetization is negligible. There is only the uncertainty on the number of valence electrons, which propagates to the ratio μ_L/μ_S, but the differences between $5f^2$ and $5f^3$ remain quite small: the ratio μ_L/μ_S is found between -2.40 – -2.15 at 1 T and between -2.15 – -1.95 at 17 T. These values are notably reduced compared to the free ion values of -3.42 ($5f^2$) and -2.57 ($5f^3$). The values of μ_{DM}/μ_S inferred from our results are close to 2, which corresponds to the theoretical value (1.85) for the $5f^3$ configuration in the intermediate coupling scheme.
In the last part of the table, we determined μ_S, μ_L/μ_S, and the total U moment

Table 5.2: Magnetic moments on U atom in UCoAl (expressed in μ_B) from XMCD data at U $M_{4,5}$-edges. μ_S is obtained with two techniques: with $\mu_{\rm bulk}$ measured by SQUID magnetometry, and with the theoretical values of $\mu_{\rm DM}/\mu_S$ for the intermediate coupling scheme.

		from sum rules			from bulk				from $\frac{\mu_{\rm DM}}{\mu_S}$		
H(T)	n^{5f}	μ_L	$\mu_S^{\rm eff}$	$\frac{\mu_L}{\mu_S^{\rm eff}}$	$\mu_{\rm bulk}$	μ_S	$\frac{\mu_L}{\mu_S}$	$\frac{\mu_{\rm DM}}{\mu_S}$	μ_S	$\frac{\mu_L}{\mu_S}$	$\mu_U^{\rm total}$
0.5	2	0.018	-0.033	-0.55	0.014(2)*	-0.004(2)	?	?	-0.007	-2.4	0.011
	3	0.017	-0.031			-0.003(2)	?	?	-0.011	-1.6	0.006
1	2	0.59	-0.78	-0.76	0.315	-0.27	-2.2	1.8	-0.17	-3.4	0.41
	3	0.54	-0.71			-0.22	-2.4	2.2	-0.25	-2.2	0.29
17	2	1.01	-1.36	-0.74	0.488**	-0.52	-1.9	1.6	-0.30	-3.3	0.70
	3	0.92	-1.24			-0.43	-2.1	1.9	-0.44	-2.1	0.49

$\star$) $\pm$0.002 for two different magnetometers
$\star\star$) extrapolated from 8 T

$\mu_U^{\rm total} = \mu_L + \mu_S$ from the theoretical values of $\mu_{\rm DM}/\mu_S$ (see Table 5.1). From the values of $\mu_U^{\rm total}$ it is clear that the $5f^2$ configuration can be dismissed, while $5f^3$ yields realistic values, close to the bulk magnetization. In this configuration, the ratio μ_L/μ_S changes from -1.6 to $\approx$-2.1 between the PM and FM states.
In reality, the number of $5f$ electrons is probably intermediate, but there are theoretical values of the dipolar magnetic term for integer valence numbers only.

5.5.6 Conclusions

We measured the absorption and XMCD of UCoAl, at the $M_{4,5}$ edges of Uranium and at the K-edge of Cobalt, at 2 K, in magnetic fields up to 17 T. This synchrotron experiment was carried out under presumably improved experimental conditions, compared to the first XMCD experiment on UCoAl reported in 2002 [59] (lower temperature, high quality sample with sharp transition, cleaved surface).
We compared our results with that of Kučera *et al.* and Takeda *et al.* [118]. We could reproduce the XMCD spectra in the FM state, but we obtained a slightly different U M_5 XMCD spectral shape in the PM state, probably because of low signal-to-noise ratio.
The XMCD spectrum at the Co K edge exhibits two main peaks which are , not present in the Co metal, and which are ascribed to a polarization induced by the U orbitals via spin-orbit coupling. The Co moment is therefore mostly induced by the U orbitals (absence of intrinsic Co moment). By comparing the U- and Co-specific magnetizations versus field, we found that their proportion is basically constant, hence the hybridization between U $5f$ and Co $4p$ orbitals is not significantly changed between the PM and FM

phase. A small additional linear contribution in the Co magnetization is ascribed to a sizeable Pauli paramagnetic effect. This suggests that the Co moment is very small, which is consistent with NMR and polarized neutron diffraction results [22, 77, 81].
Looking at the hysteresis at the metamagnetic transition, we observed different critical fields for U and Co on decreasing field sweep, which could suggest that the Co site demagnetizes before the U site. This peculiar result should be considered with precaution as long as it is not confirmed by another microscopic probe such as NMR.
Individual values of the orbital and spin moments of Uranium were obtained by applying sum rules. They are in good agreement with other XMCD [59] and polarized neutron diffraction results [81]. Our results confirm that the magnetism in UCoAl is dominated by the orbital component, which is larger and antiparallel to the spin moment. The ratio of orbital-to-spin moment μ_L/μ_S is close to -2 — which is reduced from the free ion value — in good agreement with *ab initio* calculations [60].

Moreover, we observed a change of μ_L/μ_S from -1.6 to -2.1 accross the metamagnetic transition. This change occurs while the ratio of induced Co to U moment is conserved, hence the U-5f–Co-4d hybridization is basically unchanged. We recall that the orbital-to-spin moment ratio is normally considered as a measure of the 5f–ligand hybridization [113]. Therefore in this case this is not completely true. It means that μ_L/μ_S is affected by the splitting into spin-up–spin-down bands at the metamagnetic transition, possibly via a change in the spin-orbit coupling of the 5f electrons, or maybe the quenching of the orbital moment by the crystal field is partially released when the large magnetostriction occurs.

General conclusion

The aim of this thesis was to study new materials in order to explore the physics of ferromagnetic quantum criticality. This follows the discovery of the ferromagnetic superconductors in uranium-based intermetallic compounds, and the need to find ideal systems to study the mechanisms which allow the coexistence of ferromagnetism and superconductivity.

In this thesis we have investigated three uranium-based ternary intermetallic compounds: URhSi, URhAl, and UCoAl. These are strongly correlated electron systems, with moderate heavy fermion behaviour ($\gamma \sim 100\,\mathrm{mJ.mol^{-1}.K^{-2}}$). URhSi and URhAl are itinerant ferromagnets, while UCoAl is a paramagnet being close to a ferromagnetic instability. The quantum critical behaviour in these compounds have been studied under high pressure and magnetic field. Single crystals of these materials have been grown and characterized by resistivity, magnetic, and specific heat measurements.

In Chapter 3 we discussed URhSi. High quality single crystals are difficult to obtain. We have succeeded to grow single crystals of URhSi, however the quality is very low (RRR 4). With thermal expansion measurements we observed that the Curie temperature $T_C = 10.5\,\mathrm{K}$ reduces upon application of a magnetic field perpendicular to the easy magnetization axis. By extrapolating T_C to 0 K, a quantum phase transition is expected at $\approx 40\,\mathrm{T}$, in relation with a resistivity anomaly. Given the strong similarities with the ferromagnetic superconductor URhGe, URhSi is expected to attract a lot of attention, now that its phase diagram is being unveiled. However, the main limitation for now is the low crystal quality.

The pure FM ground state in URhAl has been confirmed by neutron diffraction. The critical behaviour of the PM-FM transition at 27 K has been studied with Arrott–Noakes analysis of the magnetization. Although URhAl is certainly a 3D Ising system, the critical behaviour does not correspond to any universal class of criticality, probably because at these temperatures close to the Kondo coherence the system is in the frontier region between the Curie-Weiss picture of localized moments and the itinerant picture of band magnetism. URhAl has been studied under high pressure, focusing on the Curie temperature with AC calorimetry measurements. T_C decreases with pressure and reaches 0 K at $\approx 5.3\,\mathrm{GPa}$. We thus established the pressure phase diagram of URhAl for the first time, thereby opening the way to further studies. Preliminary results of resistivity

recently obtained by our team are indicating that the A coefficient becomes very large in the quantum critical region ($\sim 5\,\mathrm{GPa}$), where non-Fermi liquid behaviour is observed.

The chapter on UCoAl is the main part of this thesis.

The microscopic properties of the magnetization have been investigated with X-ray magnetic circular dichroism (XMCD), by probing the U $5f$ and Co $4p$ density of states. The U moment is dominated by the orbital part, which is antiparallel to the spin part. The orbital-to-spin moment ratio changes from -1.6 in the PM phase to -2.1 in the FM phase. We confirmed that the magnetism of UCoAl is almost entirely carried by the U $5f$ orbitals, and that the small Co moment is not intrinsic, but is induced by hybridization with $5f$ orbitals. The ratio of Co and U magnetization is conserved on either side of the metamagnetic transition, thus the hybridization seems unchanged.

The metamagnetic transition has been studied by bulk magnetization measurements. Very unusual relaxation phenomena have been observed, showing a succession of steps. The field tunes the speed of the relaxation but does not affect the steps. We proposed several possible explanations for these phenomena.

The transport properties have been studied under pressure by Hall effect and resistivity measurements. We have drawn the wing-shape temperature–field–pressure phase diagram of UCoAl, and we explored the region of the quantum critical endpoint. The Hall coefficient does not change significantly between the PM and FM phase. In the meantime, thermoelectric power measurements performed in our laboratory showed that S/T changes drastically. Since Hall effect and thermoelectricity are sensitive to light and heavy bands, respectively, we thus believe that they are probing different bands, so the question of a Fermi surface change is not so clear. The positive jump in Hall effect at the metamagnetic transition disappears at the pressure $P_M \approx 1.3\,\mathrm{GPa}$, while a positive jump appears in the transverse resistivity at the same pressure. The anisotropy of the resistivity under high pressure has been investigated in detail. In the longitudinal resistivity, nothing happens at P_M. The metamagnetic transition then terminates at a pressure $P_\Delta \sim 2\,\mathrm{T}$. In the region between P_M and P_Δ, a plateau appears in the transverse resistivity, with a large difference between increasing and decreasing field sweep. This up-down difference is a very peculiar phenomenon, which should be further investigated in the future. This is suggesting that a new exotic phase appears in the region of the quantum critical endpoint.

Eventually, UCoAl is not a simple system, probably because of frustration on the quasi-Kagome lattice formed by the uranium atoms. Instead, UCoAl is a promising candidate for several unexpected physical phenomena, which may lead physicists to discover new aspects of solid state and quantum matter.

Bibliography

[1] S. Doniach. The Kondo lattice and weak antiferromagnetism. *Physica B+C*, 91(0):231 – 234, 1977. Cited on page 21.

[2] Hilbert v. Löhneysen, Achim Rosch, Matthias Vojta, and Peter Wölfle. Fermi-liquid instabilities at magnetic quantum phase transitions. *Rev. Mod. Phys.*, 79:1015–1075, Aug 2007. Cited on page 22.

[3] O. Trovarelli, C. Geibel, S. Mederle, C. Langhammer, F. M. Grosche, P. Gegenwart, M. Lang, G. Sparn, and F. Steglich. $YbRh_2Si_2$: Pronounced Non-Fermi-Liquid Effects above a Low-Lying Magnetic Phase Transition. *Phys. Rev. Lett.*, 85:626–629, Jul 2000. Cited on page 22.

[4] S. Friedemann, S. Wirth, S. Kirchner, Q. Si, S. Hartmann, C. Krellner, C. Geibel, T. Westerkamp, M. Brando, and F. Steglich. Break Up of Heavy Fermions at an Antiferromagnetic Instability. *Journal of the Physical Society of Japan*, 80SA(Supplement A):SA002, 2011. Cited on page 22.

[5] H. v. Löhneysen, T. Pietrus, G. Portisch, H. G. Schlager, A. Schröder, M. Sieck, and T. Trappmann. Non-Fermi-liquid behavior in a heavy-fermion alloy at a magnetic instability. *Phys. Rev. Lett.*, 72:3262–3265, May 1994. Cited on page 22.

[6] A. Schröder, G. Aeppli, R. Coldea, M. Adams, O. Stockert, H.v. Löhneysen, E. Bucher, R. Ramazashvili, and P. Coleman. Onset of antiferromagnetism in heavy-fermion metals. *Nature*, 407(6802):351–355, September 2000. Cited on page 22.

[7] C. Pfleiderer, G. J. McMullan, S. R. Julian, and G. G. Lonzarich. Magnetic quantum phase transition in MnSi under hydrostatic pressure. *Phys. Rev. B*, 55:8330–8338, Apr 1997. Cited on page 22.

[8] Andrew Huxley, Ilya Sheikin, Eric Ressouche, Nolwenn Kernavanois, Daniel Braithwaite, Roberto Calemczuk, and Jacques Flouquet. UGe_2 : A ferromagnetic spin-triplet superconductor. *Phys. Rev. B*, 63:144519, Mar 2001. Cited on page 22.

[9] M Uhlarz, C Pfleiderer, and SM Hayden. Quantum phase transitions in the itinerant ferromagnet $ZrZn_2$. *Phys. Rev. Lett.*, 93(25):256404, Dec 17 2004. Cited on pages 22, 77, 78, and 93.

[10] T. Goto, Y. Shindo, H. Takahashi, and S. Ogawa. Magnetic properties of the itinerant metamagnetic system $Co(S_{1-x}Se_x)_2$ under high magnetic fields and high pressure. *Phys. Rev. B*, 56:14019–14028, Dec 1997. Cited on pages 22 and 79.

[11] Y. J. Uemura, T. Goko, I. M. Gat-Malureanu, J. P. Carlo, P. L. Russo, A. T. Savici, A. Aczel, G. J. MacDougall, J. A. Rodriguez, G. M. Luke, S. R. Dunsiger, A. McCollam, J. Arai, Ch. Pfleiderer, P. Boni, K. Yoshimura, E. Baggio-Saitovitch, M. B. Fontes, J. Larrea, Y. V. Sushko, and J. Sereni. Phase separation and suppression of critical dynamics at quantum phase transitions of MnSi and $(Sr_{(1-x)}Ca_x)RuO_3$. *Nat Phys*, 3(1):29–35, January 2007. Cited on page 22.

[12] Sen Yang, Xiaobing Ren, and Xiaoping Song. Evidence for first-order nature of the ferromagnetic transition in Ni, Fe, Co, and $CoFe_2O_4$. *Phys. Rev. B*, 78:174427, Nov 2008. Cited on page 22.

[13] A. I. Larkin and S. A. Pikin. Phase transitions of the first order but nearly of the second. *Soviet Physics JETP-USSR*, 29(5):891–896, 1969. Cited on page 23.

[14] Vladimir P. Mineev. On the phase diagram of UGe_2. *Comptes Rendus Physique*, 12(5-6):567–572, Jun-Aug 2011. Cited on page 23.

[15] D. Belitz, T. R. Kirkpatrick, and Thomas Vojta. First Order Transitions and Multicritical Points in Weak Itinerant Ferromagnets. *Phys. Rev. Lett.*, 82:4707–4710, Jun 1999. Cited on page 23.

[16] Robert B. Griffiths. Proposal for Notation at Tricritical Points. *Phys. Rev. B*, 7:545–551, Jan 1973. Cited on page 24.

[17] V. Taufour, D. Aoki, G. Knebel, and J. Flouquet. Tricritical Point and Wing Structure in the Itinerant FerromagnetUGe(2). *Phys. Rev. Lett.*, 105(21):217201, November 2010. Cited on pages 24, 77, and 78.

[18] H. Kotegawa, V. Taufour, D. Aoki, G. Knebel, and J. Flouquet. Evolution toward Quantum Critical End Point in UGe(2). *J. Phys. Soc. Jpn.*, 80(8):083703, August 2011. Cited on pages 24, 77, and 78.

[19] V. Taufour. *Croissance de cristaux de composés à base d'Uranium et étude de UGe_2*. PhD thesis, Université de Grenoble, 2011. Cited on page 24.

[20] H. H. Hill. *Plutonium and Other Actinides*. 1970. Cited on page 26.

[21] A.E. Dwight. In B.C. Giessen, editor, *Developments in the Structural Chemistry of Alloy Phases*, page 182. Plenum, New York, 1969. Cited on page 27.

[22] H. Nohara, H. Kotegawa, H. Tou, T. D. Matsuda, E. Yamamoto, Y. Haga, Z. Fisk, Y. Ōnuki, D. Aoki, and J. Flouquet. Strong Longitudinal Magnetic Fluctuations Near Critical End Point in UCoAl: A (59)Co-NMR Study. *J. Phys. Soc. Jpn.*, 80(9):093707, September 2011. Cited on pages 27, 79, 80, 83, 101, 125, 133, and 137.

[23] V. Sechovský and L. Havela. Chapter 1 Magnetism of ternary intermetallic compounds of Uranium. volume 11 of *Handbook of Magnetic Materials*, pages 1 – 289. Elsevier, 1998. Cited on pages 26, 28, and 30.

[24] Inga Fischer. *Metallic Magnets without Inversion Symmetry and Antiferromagnetic Quantum Critical Points*. PhD thesis, Institute for Theoretical Physics - University of Cologne, 2006. Cited on page 28.

[25] Dai Aoki, Andrew Huxley, Eric Ressouche, Daniel Braithwaite, Jacques Flouquet, Jean-Pascal Brison, Elsa Lhotel, and Carley Paulsen. Coexistence of superconductivity and ferromagnetism in URhGe. *Nature*, 413(6856):613–616, October 2001. Cited on pages 29 and 31.

[26] N. T. Huy, A. Gasparini, D. E. de Nijs, Y. Huang, J. C. P. Klaasse, T. Gortenmulder, A. de Visser, A. Hamann, T. Görlach, and H. v. Löhneysen. Superconductivity on the Border of Weak Itinerant Ferromagnetism in UCoGe. *Phys. Rev. Lett.*, 99:067006, Aug 2007. Cited on pages 29 and 31.

[27] F. Lévy, I. Sheikin, B. Grenier, and A. D. Huxley. Magnetic Field-Induced Superconductivity in the Ferromagnet URhGe. *Science*, 309(5739):1343–1346, 2005. Cited on pages 29, 31, and 50.

[28] D. Aoki, T. D. Matsuda, V. Taufour, E. Hassinger, G. Knebel, and J. Flouquet. Extremely Large and Anisotropic Upper Critical Field and the Ferromagnetic Instability in UCoGe. *Journal of the Physical Society of Japan*, 78(11):113709, November 2009. Cited on pages 29 and 50.

[29] Dai Aoki and Jacques Flouquet. Ferromagnetism and Superconductivity in Uranium Compounds. *Journal of the Physical Society of Japan*, 81(1):011003, 2012. Cited on pages 29, 32, and 45.

[30] S. S. Saxena, P. Agarwal, K. Ahilan, F. M. Grosche, R. K. W. Haselwimmer, M. J. Steiner, E. Pugh, I. R. Walker, S. R. Julian, P. Monthoux, G. G. Lonzarich, A. Huxley, I. Sheikin, D. Braithwaite, and J. Flouquet. Superconductivity on the border of itinerant-electron ferromagnetism in UGe_2. *Nature*, 406(6796):587–592, August 2000. Cited on page 31.

[31] Uranium Radiation Properties, www.wise-uranium.org, 2012. Cited on page 36.

[32] T. C. Kobayashi, H. Hidaka, H. Kotegawa, K. Fujiwara, and M. I. Eremets. Nonmagnetic indenter-type high-pressure cell for magnetic measurements. *Review of Scientific Instruments*, 78(2):–, 2007. Cited on pages 37 and 123.

[33] Naoyuki Tateiwa, Yoshinori Haga, Zachary Fisk, and Yoshichika Ōnuki. Miniature ceramic-anvil high-pressure cell for magnetic measurements in a commercial superconducting quantum interference device magnetometer. *Review of Scientific Instruments*, 82(5):–, 2011. Cited on pages 37 and 123.

[34] B. Salce, J. Thomasson, A. Demuer, J. J. Blanchard, J. M. Martinod, L. Devoille, and A. Guillaume. Versatile device for low temperature in situ generation of forces up to 25 kN: Application to hydrostatic pressure experiments. *Review of Scientific Instruments*, 71(6):2461–2466, 2000. Cited on page 41.

[35] Paul F. Sullivan and G. Seidel. Steady-State, ac-Temperature Calorimetry. *Phys. Rev.*, 173:679–685, Sep 1968. Cited on page 41.

[36] J Derr, G Knebel, G Lapertot, B Salce, M-A Méasson, and J Flouquet. Valence and magnetic ordering in intermediate valence compounds: TmSe versus SmB_6. *Journal of Physics: Condensed Matter*, 18(6):2089, 2006. Cited on page 42.

[37] K. Prokeš, Th. Wand, A.V. Andreev, M. Meissner, F. Honda, and V. Sechovský. Magnetic specific heat and magnetoresistance of URhSi. *Journal of Alloys and Compounds*, 460(1-2):47 – 53, 2008. Cited on pages 45, 47, and 48.

[38] R. Troć and V.H. Tran. Magnetic properties of UT(Si,Ge) series. *Journal of Magnetism and Magnetic Materials*, 73(3):389 – 397, 1988. Cited on page 45.

[39] F.R. de Boer, E. Brück, J. C. P. Klaasse, H. Nakotte, K. H. J. Buschow, L. Havela, V. Sechovský, P. Nozar, E. Sugiura, M. Ono, M. Date, and A. Yamagishi. Development of the ground state within the UTSi system. *Journal of Applied Physics*, 69(8):4702–4704, 1991. Cited on page 45.

[40] V. H. Tran and R. Troć. Large magnetoresistance of the ferromagnetic intermetallics URhSi and URhGe. *Phys. Rev. B*, 57:11592–11597, May 1998. Cited on page 45.

[41] K. Prokeš, E. Brück, K. H. J. Buschow, F. R. de Boer, V. Sechovský, P. Svoboda, X. Hu, H. Maletta, and T. J. Gortenmulder. Magnetism in URhSi. *Journal of Applied Physics*, 79(8):5221–5223, 1996. Cited on page 45.

[42] K. Prokeš, A.V. Andreev, F. Honda, and V. Sechovský. Magnetic structure of URhSi single crystal. *Journal of Magnetism and Magnetic Materials*, 261(1,2):131–138, 2003. Cited on page 46.

[43] K. Prokeš and A. Gukasov. Magnetization densities in URhSi studied by polarized neutron diffraction. *Phys. Rev. B*, 79:024406, Jan 2009. Cited on page 46.

[44] B Lloret. PhD thesis, University of Bordeaux, 1988. Cited on page 47.

[45] Kazuo Ueda and Tôru Moriya. Contribution of Spin Fluctuations to the Electrical and Thermal Resistivities of Weakly and Nearly Ferromagnetic Metals. *Journal of the Physical Society of Japan*, 39(3):605–615, 1975. Cited on pages 48 and 80.

[46] K. Ikeda, S.K. Dhar, M. Yoshizawa, and K.A. Gschneidner Jr. Quenching of spin fluctuations by high magnetic fields. *Journal of Magnetism and Magnetic Materials*, 100(1-3):292 – 321, 1991. Cited on page 49.

[47] Niels Hessel Andersen and Henrik Smith. Electron-magnon interaction and the electrical resistivity of Tb. *Phys. Rev. B*, 19:384–387, Jan 1979. Cited on page 49.

[48] Tatsuma D. Matsuda. Magnetic Anisotropy and Field Induced Effective Mass Enhancement in URhSi. *Journal of the Physical Society of Japan*, to be published. Cited on page 49.

[49] V. P. Mineev. Magnetic field dependence of pairing interaction in ferromagnetic superconductors with triplet pairing. *Phys. Rev. B*, 83:064515, Feb 2011. Cited on page 51.

[50] W. Knafo, T. D. Matsuda, D. Aoki, F. Hardy, G. W. Scheerer, G. Ballon, M. Nardone, A. Zitouni, C. Meingast, and J. Flouquet. High-field moment polarization in the ferromagnetic superconductor UCoGe. *Phys. Rev. B*, 86(18), NOV 12 2012. Cited on pages 51 and 55.

[51] P. A. Veenhuizen, F. R. De Boer, A. A. Menovsky, V Sechovský, and L Havela. Magnetic properties of URuAl and URhAl single-crystals. *Journal de Physique*, 49(C-8, 1):485–486, DEC 1988. Cited on page 57.

[52] L. Havela, M. Diviš, V. Sechovský, A.V. Andreev, F. Honda, G. Oomi, Y. Méresse, and S. Heathman. U ternaries with ZrNiAl structure − lattice properties. *J. Alloys Compd.*, 322(1-2):7–13, June 2001. Cited on pages 57, 74, and 90.

[53] T.D. Cuong, Z. Arnold, J. Kamarád, A.V. Andreev, L. Havela, and V. Sechovský. Composition and volume dependence of magnetism in $URu_{(1-x)}Rh_xAl$ and $URuAl_{(1-y)}Sn_y$. *Journal of Magnetism and Magnetic Materials*, 157-158(0):694 – 695, 1996. European Magnetic Materials and Applications Conference. Cited on pages 57 and 60.

[54] J. A. Paixão, G. H. Lander, A. Delapalme, H. Nakotte, F. R. de Boer, and E. Brück. Evidence for Anisotropic Hybridization in Uranium Compounds. *EPL (Europhysics Letters)*, 24(7):607, 1993. Cited on page 57.

[55] W Grange, M Finazzi, J.-P Kappler, A Delobbe, G Krill, Ph Sainctavit, J.-P Sanchez, A Rogalev, and J Goulon. 5f-hybridization in URhAl studied by X-ray magnetic circular dichroism. *Journal of Alloys and Compounds*, 275-277(0):583 – 586, 1998. Cited on pages 57 and 58.

[56] T Gasche, M S S Brooks, and B Johansson. Ground-state properties of ternary uranium compounds: I. Hybridization effects. *Journal of Physics: Condensed Matter*, 7(49):9499, 1995. Cited on page 58.

[57] P.M. Oppeneer, A.Ya. Perlov, V.N. Antonov, A.N. Yaresko, T. Kraft, and M.S.S. Brooks. Optical and magneto-optical spectroscopy of uranium and plutonium compounds: recent theoretical progress . *Journal of Alloys and Compounds*, 271-273(0):831 – 836, 1998. Cited on page 58.

[58] J. Kuneš, P. Novák, M. Diviš, and P. M. Oppeneer. Magnetic, magneto-optical, and structural properties of URhAl from first-principles calculations. *Phys. Rev. B*, 63:205111, May 2001. Cited on page 58.

[59] M. Kučera, J. Kuneš, A. Kolomiets, M. Diviš, A. V. Andreev, V. Sechovský, J.-P. Kappler, and A. Rogalev. X-ray magnetic circular dichroism studies of $5f$ magnetism in UCoAl and UPtAl. *Phys. Rev. B*, 66:144405, Oct 2002. Cited on pages 58, 79, 128, 130, 131, 136, and 137.

[60] V. N. Antonov, B. N. Harmon, O. V. Andryushchenko, L. V. Bekenev, and A. N. Yaresko. Electronic structure and X-ray magnetic circular dichroism in uranium compounds. II. UTAl (T = Co, Rh, and Pt) intermetallics. *Phys. Rev. B*, 68:214425, Dec 2003. Cited on pages 58, 79, and 137.

[61] M. Kučera, P. Beránková, M. Matyáš, I. Tichý, and A.A. Menovsky. Magneto-optical investigations of URhAl intermetallic compound. *Journal of Alloys and Compounds*, 271-273(0):467 – 470, 1998. Cited on page 58.

[62] P. Javorský, L. Havela, F. Wastin, P. Boulet, and J. Rebizant. Magnetic properties of diluted band ferromagnet URhAl. *Phys. Rev. B*, 69:054412, Feb 2004. Cited on pages 58 and 74.

[63] A Hiess, L Havela, K Prokes, RS Eccleston, and GH Lander. Magnetic response function in URhAl. *PHYSICA B*, 230:89–91, FEB 1997. SCES 96, ZURICH, SWITZERLAND, AUG 19-22, 1996. Cited on page 58.

[64] K. P. Belov and A. N. Goryaga. *Fiz. Met. Metalloved.*, 2:3, 1956. Cited on page 64.

[65] A. Arrott. *Physical Review*, 108:1394, 1957. Cited on page 64.

[66] Anthony Arrott and John E. Noakes. Approximate Equation of State For Nickel Near its Critical Temperature. *Phys. Rev. Lett.*, 19:786–789, Oct 1967. Cited on page 64.

[67] S.N. Kaul. Static critical phenomena in ferromagnets with quenched disorder. *Journal of Magnetism and Magnetic Materials*, 53(1-2):5 – 53, 1985. Cited on page 65.

[68] T. Hattori, Y. Ihara, K. Ishida, Y. Nakai, E. Osaki, K. Deguchi, N. K. Sato, and I. Satoh. ^{59}Co-NMR/Nuclear-Quadrupole-Resonance (NQR) Studies on Ferromagnetic Superconductor UCoGe. *Journal of the Physical Society of Japan*, 80SA(Supplement A):SA007, 2011. Cited on page 74.

[69] Dietrich Belitz, T. R. Kirkpatrick, and J Rollbuhler. Tricritical behavior in itinerant quantum ferromagnets. *Phys. Rev. Lett.*, 94(24):247205, Jun 24 2005. Cited on page 77.

[70] W. Wu, A. McCollam, S. A. Grigera, R. S. Perry, A. P. Mackenzie, and S. R. Julian. Quantum critical metamagnetism of $Sr_3Ru_2O_7$ under hydrostatic pressure. *Phys. Rev. B*, 83:045106, Jan 2011. Cited on page 78.

[71] Mario Zacharias and Markus Garst. Quantum criticality in itinerant metamagnets. *Phys. Rev. B*, 87:075119, Feb 2013. Cited on page 78.

[72] M. Bercx and F. F. Assaad. Metamagnetism and Lifshitz transitions in models for heavy fermions. *Phys. Rev. B*, 86:075108, Aug 2012. Cited on page 78.

[73] R. Daou, C. Bergemann, and S. R. Julian. Continuous Evolution of the Fermi Surface of $CeRu_2Si_2$ across the Metamagnetic Transition. *Phys. Rev. Lett.*, 96:026401, Jan 2006. Cited on pages 78 and 93.

[74] A. V. Andreev, R. Z. Levitin, Y. F. Popov, and R. Y. Yumaguzhin. Metamagnetism of UAlCo. *Sov. Phys. Solid State*, 27:1145–1146, 1985. Cited on pages 78, 80, and 83.

[75] N. V. Mushnikov, T. Goto, K. Kamishima, H. Yamada, A. V. Andreev, Y. Shiokawa, and A. Iwao. Magnetic properties of the 5f itinerant electron metamagnet UCoAl under high pressure. *Phys. Rev. B*, 59(10):6877–6885, March 1999. Cited on pages 78, 80, 89, 90, and 124.

[76] D. Aoki, T. Combier, V. Taufour, T. D. Matsuda, G. Knebel, H. Kotegawa, and J. Flouquet. Ferromagnetic Quantum Critical Endpoint in UCoAl. *J. Phys. Soc. Jpn.*, 80(9):094711, September 2011. Cited on pages 78, 79, 81, 83, 88, 89, 90, 99, 106, 108, 114, and 124.

[77] K. Karube, T. Hattori, S. Kitagawa, K. Ishida, N. Kimura, and T. Komatsubara. Universality and critical behavior at the critical endpoint in the itinerant-electron metamagnet UCoAl. *Phys. Rev. B*, 86(2):024428, JUL 23 2012. Cited on pages 78, 80, 83, 101, 125, 133, and 137.

[78] A. Palacio-Morales, A. Pourret, G. Knebel, T. Combier, D. Aoki, H. Harima, and J. Flouquet. Metamagnetic Transition in UCoAl Probed by Thermoelectric Measurements. *Phys. Rev. Lett.*, 110:116404, Mar 2013. Cited on pages 78, 80, 83, 92, 93, and 101.

[79] Fuminori Honda, G. Oomi, A. V. Andreev, V. Sechovský, and Y. Shiokawa. Electrical resistance and magnetoresistance of UCoAl under high pressure. *Journal of Nuclear Science and Technology*, Supplement 3:126–128, 2002. Cited on pages 78, 80, 106, 108, and 114.

[80] L. Havela, A.V. Andreev, V. Sechovský, I.K. Kozlovskaya, K. Prokeš, P. Javorský, M.I. Bartashevich, T. Goto, and K. Kamishima. $5f$-band metamagnetism in UCoAl. *Physica B: Condensed Matter*, 230-232(0):98 – 101, 1997. Proceedings of the International Conference on Strongly Correlated Electron Systems. Cited on page 79.

[81] M. Wulff, J.M. Fournier, A. Delapalme, B. Gillon, A. Sechovský, L. Havela, and A.V. Andreev. Study of orbital and spin magnetism in UCoAl by polarized neutron diffraction. *Physica B: Condensed Matter*, 163(1-3):331 – 334, 1990. Cited on pages 79, 125, 133, and 137.

[82] P. Javorský, V. Sechovský, J. Schweizer, F. Bourdarot, E. Lelièvre-Berna, A. V. Andreev, and Y. Shiokawa. Magnetization densities in UCoAl studied by polarized neutron diffraction. *Phys. Rev. B*, 63:064423, Jan 2001. Cited on page 79.

[83] A.V. Andreev, N.V. Mushnikov, T. Goto, V. Sechovský, Y. Homma, and Y. Shiokawa. Interplay between doping and pressure effects in magnetism of $UCo_{(1-x)}T_xAl$ (T=Fe,Ni) single crystals. *Physica B: Condensed Matter*, 329-333, Part 2(0):499 – 501, 2003. Proceedings of the 23rd International Conference on Low Temperature Physics. Cited on page 79.

[84] Y. Ishii, M. Kosaka, Y. Uwatoko, A.V. Andreev, and V. Sechovský. Ferromagnetism induced in UCoAl under uniaxial pressure. *Physica B: Condensed Matter*, 334(1-2):160 – 166, 2003. Cited on page 80.

[85] A V Andreev, M I Bartashevich, T Goto, K Kamishima, L Havela, and V Sechovský. Effects of external pressure on the 5f-band metamagnetism in UCoAl. *Phys. Rev. B*, 55(9):5847–5850, 1997. Cited on page 80.

[86] L. Havela, A. Kolomiets, F. Honda, A.V. Andreev, V. Sechovský, L.E. DeLong, Y. Shiokawa, T. Kagayama, and G. Oomi. Stability of the non-Fermi liquid state in UCoAl. *Physica B: Condensed Matter*, 281,282(0):379 – 380, 2000. Cited on pages 80 and 96.

[87] A. J. Bograd, J. S. Alwood, D. J. Mixon, J. S. Kim, and G. R. Stewart. Non-Fermi liquid behavior in UCoAl. 2002. Cited on page 80.

[88] Ladislav Havela, Fuminori Honda, Jean-Christophe Griveau, Alexander V. Andreev, Alexandre Kolomiets, and Vladimir Sechovský. Non-Fermi liquid behaviour in UCoAl: Pressure variations . *Journal of Alloys and Compounds*, 408,412(0):1316 – 1319, 2006. Proceedings of Rare Earths'04 in Nara, Japan. Cited on page 80.

[89] N. Doiron-Leyraud, I. R. Walker, L. Taillefer, M. J. Steiner, S. R. Julian, and G. G. Lonzarich. Fermi-liquid breakdown in the paramagnetic phase of a pure metal. *Nature*, 425(6958):595–599, October 2003. Cited on page 80.

[90] Tristan Combier, Dai Aoki, Georg Knebel, and Jacques Flouquet. Ferromagnetic Quantum Criticality Studied by Hall Effect Measurements in UCoAl. *Journal of the Physical Society of Japan*, 82(10):104705, 2013. Cited on page 80.

[91] T. D. Matsuda, H. Sugawara, Y. Aoki, H. Sato, A. V. Andreev, Y. Shiokawa, V. Sechovský, and L. Havela. Transport properties of the anisotropic itinerant-electron metamagnet UCoAl. *Phys. Rev. B*, 62(21):13852–13855, December 2000. Cited on pages 83 and 84.

[92] Hiroshi Kontani, Morio Miyazawa, and Kosaku Yamada. Theory of Anomalous Hall Effect in a Heavy Fermion System with a Strong Anisotropic Crystal Field. *J. Phys. Soc. Jpn.*, 66(8):2252–2255, 1997. Cited on page 84.

[93] A. Fert and P. M. Levy. Theory of the Hall effect in heavy-fermion compounds. *Phys. Rev. B*, 36:1907–1916, Aug 1987. Cited on page 84.

[94] S. Mašková, A.M. Adamska, L. Havela, N.-T.H. Kim-Ngan, J. Przewoźnik, S. Daniš, K. Kothapalli, A.V. Kolomiets, S. Heathman, H. Nakotte, and H. Bordallo. Lattice anisotropy in uranium ternary compounds: UTX. *J. Alloys Compd.*, 522(0):130–135, May 2012. Cited on page 90.

[95] R. Settai, M. Nakashima, S. Araki, Y. Haga, T. C. Kobayashi, N. Tateiwa, H. Yamagami, and Y. Ōnuki. A change of the Fermi surface in UGe_2 across the critical pressure. *J. Phys.: Condens. Matter*, 14(1):L29, 2002. Cited on page 92.

[96] Y Haga, M Nakashima, R Settai, S Ikeda, T Okubo, S Araki, TC Kobayashi, N Tateiwa, and Y. Ōnuki. A change of the Fermi surface across the metamagnetic transition under pressure in UGe_2. *J. Phys.: Condens. Matter*, 14(5):L125–L135, FEB 11 2002. Cited on page 92.

[97] S Kambe, J Flouquet, P Haen, and P Lejay. Characteristic of metamagnetic transition in $CeRu_2Si_2$ revealed with Hall mobility. *J. Low Temp. Phys.*, 102(5-6):477–486, MAR 1996. Cited on page 93.

[98] H. Aoki, S. Uji, A. K. Albessard, and Y. Ōnuki. Transition of f electron nature from itinerant to localized: Metamagnetic transition in $CeRu_2Si_2$ studied via the de Haas-van Alphen effect. *Phys. Rev. Lett.*, 71:2110–2113, Sep 1993. Cited on page 93.

[99] N. Kimura, M. Endo, T. Isshiki, S. Minagawa, A. Ochiai, H. Aoki, T. Terashima, S. Uji, T. Matsumoto, and G. G. Lonzarich. de Haas-van Alphen Effect in $ZrZn_2$ under Pressure: Crossover between Two Magnetic States. *Phys. Rev. Lett.*, 92:197002, May 2004. Cited on page 93.

[100] Tatsuma D. Matsuda, Yuji Aoki, Hitoshi Sugawara, Hideyuki Sato, Alexander V. Andreev, and Vladimir Sechovský. Specific-Heat Anomaly around Metamagnetic Transition in UCoAl. *Journal of the Physical Society of Japan*, 68(12):3922–3926, 1999. Cited on page 99.

[101] Kazumasa Miyake and Osamu Narikiyo. Enhanced Impurity Scattering due to Quantum Critical Fluctuations: Perturbational Approach. *Journal of the Physical Society of Japan*, 71(3):867–871, 2002. Cited on page 108.

[102] Youhei Yamaji, Takahiro Misawa, and Masatoshi Imada. Quantum Metamagnetic Transitions Induced by Changes in Fermi-Surface Topology: Applications to a Weak Itinerant-Electron Ferromagnet $ZrZn_2$. *Journal of the Physical Society of Japan*, 76(6):063702, 2007. Cited on page 113.

[103] S. A. Grigera, P. Gegenwart, R. A. Borzi, F. Weickert, A. J. Schofield, R. S. Perry, T. Tayama, T. Sakakibara, Y. Maeno, A. G. Green, and A. P. Mackenzie. Disorder-Sensitive Phase Formation Linked to Metamagnetic Quantum Criticality. *Science*, 306(5699):1154–1157, 2004. Cited on page 113.

[104] R. A. Borzi, S. A. Grigera, J. Farrell, R. S. Perry, S. J. S. Lister, S. L. Lee, D. A. Tennant, Y. Maeno, and A. P. Mackenzie. Formation of a Nematic Fluid at High Fields in $Sr_3Ru_2O_7$. *Science*, 315(5809):214–217, 2007. Cited on page 113.

[105] A. W. Rost, S. A. Grigera, J. A. N. Bruin, R. S. Perry, D. Tian, S. Raghu, Steven Allan Kivelson, and A. P. Mackenzie. Thermodynamics of phase formation in the quantum critical metal $Sr_3Ru_2O_7$. *Proceedings of the National Academy of Sciences*, 108(40):16549–16553, 2011. Cited on page 113.

[106] S. A. Kivelson, E. Fradkin, and V. J. Emery. Electronic liquid-crystal phases of a doped Mott insulator. *Nature*, 393(6685):550–553, June 1998. Cited on page 113.

[107] Chihiro Sekine, Toshiro Sakakibara, Hiroshi Amitsuka, Yoshihito Miyako, and Tsuneaki Goto. Magnetic Properties and Phase Diagram of $Ce(Ru_{1-x}Rh_x)_2Si_2$ $(0 \leq x < 0.5)$. *Journal of the Physical Society of Japan*, 61(12):4536–4546, 1992. Cited on page 113.

[108] Masugu Sato, Yoshihiro Koike, Susumu Katano, Naoto Metoki, Hiroaki Kadowaki, and Shuzo Kawarazaki. Field-induced Ferromagnetic Correlation in the Metamagnetic Crossover in $CeRu_2Si_2$ as Studied by Neutron Scattering. *Journal of the Physical Society of Japan*, 73(12):3418–3421, 2004. Cited on page 113.

[109] K. G. Sandeman, G. G. Lonzarich, and A. J. Schofield. Ferromagnetic Superconductivity Driven by Changing Fermi Surface Topology. *Phys. Rev. Lett.*, 90:167005, Apr 2003. Cited on page 113.

[110] B. Binz and M. Sigrist. Metamagnetism of itinerant electrons in multi-layer ruthenates. *EPL (Europhysics Letters)*, 65(6):816, 2004. Cited on page 113.

[111] Dante Gatteschi and Roberta Sessoli. Quantum Tunneling of Magnetization and Related Phenomena in Molecular Materials. *Angewandte Chemie International Edition*, 42(3):268–297, 2003. Cited on page 121.

[112] Victor Mougel, Lucile Chatelain, Jacques Pécaut, Roberto Caciuffo, Éric Colineau, Jean-Christophe Griveau, and Marinella Mazzanti. Uranium and manganese assembled in a wheel-shaped nanoscale single-molecule magnet with high spin-reversal barrier. *Nat Chem*, 4(12):1011–1017, December 2012. Cited on page 121.

[113] G. H. Lander, P. J. Brown, C. Stassis, P. Gopalan, J. Spalek, and G. Honig. Magnetic and structural study of $La_{1.8}Sr_{0.2}NiO_4$. *Phys. Rev. B*, 43:448–456, Jan 1991. Cited on pages 124 and 137.

[114] B. T. Thole, P. Carra, F. Sette, and G. van der Laan. X-ray circular dichroism as a probe of orbital magnetization. *Phys. Rev. Lett.*, 68:1943–1946, Mar 1992. Cited on page 126.

[115] Paolo Carra, B. T. Thole, Massimo Altarelli, and Xindong Wang. X-ray circular dichroism and local magnetic fields. *Phys. Rev. Lett.*, 70:694–697, Feb 1993. Cited on page 126.

[116] J. Stöhr and H. König. Determination of Spin- and Orbital-Moment Anisotropies in Transition Metals by Angle-Dependent X-Ray Magnetic Circular Dichroism. *Phys. Rev. Lett.*, 75:3748–3751, Nov 1995. Cited on page 127.

[117] A.C. Thompson and D. Vaughan. X-Ray Data Booklet. Lawrence Berkeley National Laboratory, University of California, Berkeley, California, 2001. Cited on page 127.

[118] Yukiharu Takeda, Yuji Saitoh, Tetsuo Okane, Hiroshi Yamagami, Tatsuma D. Matsuda, Etsuji Yamamoto, Yoshinori Haga, Yoshichika Ōnuki, and Zachary Fisk. Separation of magnetic properties at uranium and cobalt sites in UCoAl using soft X-ray magnetic circular dichroism. *Physical Review B*, 88(7), Aug 5 2013. Cited on pages 128, 130, 133, and 136.

[119] Gerrit van der Laan and B. T. Thole. X-ray-absorption sum rules in jj-coupled operators and ground-state moments of actinide ions. *Phys. Rev. B*, 53:14458–14469, Jun 1996. Cited on page 130.

[120] F. Wilhelm and A Rogalev. X-ray Magnetic Circular Dichroism studies of Magnetism in Actinides. In 4^{th} *SCM, Frankfurt, 28 March 2010*, 2010. Cited on page 133.